CATO-2 Deliverable WP 3.3 - D28a

Mineralogical and microstructural characteristics of the Werkendam field related to long-term CO_2 induced reactions: analytical/mineralogical data on reservoir evolution.

Prepared by: Mariëlle Koenen
Laura Wasch
Svenja Waldmann
Susanne Nelskamp

Reviewed by: Harmen Mijnlieff

Approved by: J.Brouwer
(CATO-2 Director)

1 Executive Summary (restricted)

An assessment of the long-term fate of CO_2 in a reservoir is required for CO_2 storage according to EU regulations. Assuming that CO_2 will be successfully contained after injection, the long-term effects depend on the gas-water-rock interactions within the storage reservoir. These interactions can be investigated using experiments and geochemical modelling. The first are per definition short-term, while the latter use simplified representations of complex geological systems. Another way to investigate the long-term effects is provided by natural CO_2 fields, the so called natural analogues. The natural CO_2 field of Werkendam in the Netherlands is representative for numerous potential Dutch storage locations, both on- and offshore. These potential storage sites, including the P18-4 reservoir of the ROAD project, are mostly (future) depleted hydrocarbon reservoirs, located in Triassic sandstone formations in the Dutch subsurface. The Werkendam gas field contains over 70% of CO_2. The CO_2 has probably been present in the reservoir for millions of year. Investigations into this 'natural lab' provided insights on the gas-water-rock interactions on geological time scales, insights which were used to calibrate a geochemical model on the long-term fate of CO_2.

Core samples from the Werkendam field were studied and compared to samples from a CO_2-free stratigraphic equivalent. This *reference* formation is a nearby natural gas (CH_4) field in the same sandstone formation, the Barendrecht-Ziedewij field. Also, samples from the Werkendam aquifer were investigated, but comparison with Barendrecht-Ziedewij is more relevant due to similar water saturation conditions and the presence of hydrocarbons. X-ray diffraction and Scanning Electron Microscopy methods were applied to unravel the mineral reactions which occurred during the history of the sediments and determine their successive and relative occurrence in time.

The analyses show that the early mineral reactions were similar in both gas fields and the aquifer. Some differences can be attributed to variations in primary mineralogy, deviations in burial history of the fields and brine composition. Concerning the later stages, the Werkendam samples show mineral reactions which are not observed in the samples from the natural gas field and the aquifer. These reactions, which we attributed to the presence of CO_2, include the partial dissolution of K-feldspar grains ($KAlSi_3O_8$) and anhydrite cement ($CaSO_4$), and the formation of small amounts of Mg-rich siderite ($MgFe(CO_3)_2$), barite ($BaSO_4$) and quartz (SiO_2). These reactions can be summarized as follows:

K-feldspar + anhydrite + Mg^{2+} + Fe^{2+} + CO_2 →
Mg-rich siderite + quartz + barite + Ca^{2+} + K^+ + Al^+

The iron is probably supplied by reduction of hematite after charging of the reservoir with oil, prior to CO_2 influx. The released iron could react with the dissolved carbon after CO_2 influx to form siderite. Petrographic analyses did not allow precise quantification of the amount of CO_2 trapped in siderite since the formation of siderite is very local and only limited core material was available. A rough estimation based on an average siderite content of 0.6-3.2 wt% indicated that 20-58% of the CO_2 is sequestered in these carbonates. The remaining CO_2 is currently still present in the supercritical phase. The lack of a potassium and aluminium sink from K-feldspar dissolution and a calcium sink from anhydrite dissolution, as well as a lack of source of magnesium for Mg-rich siderite precipitation, suggests that mass transport took place to and from the sandstones. A possible explanation would be the interaction between

the sandstone rocks and the shaley intervals within. Future work should investigate these shaley intervals and potential mass transfer. Dolomite crystals with ankerite rims present in the rocks are unaffected by the CO_2. Probably, the presence of oil prior to CO_2 influx resulted in oil rims around the crystals which protected the ankerite from dissolution.

On the basis of the Werkendam and Barendrecht-Ziedewij cases, a geochemical (batch) reaction model was developed. In the model, a high CO_2 partial pressure was applied to the mineralogy of Barendrecht-Ziedewij, in order to assess if the model is able to simulate the CO_2-induced reactions that occurred in the Werkendam field. For this purpose, assumptions needed to be made with regard to the initial mineralogy, as well as potential secondary minerals which might precipitate. These assumptions influence the model results and they are not easy to fine-tune. We were able to select a set of assumptions for the model to match the observed reactions. This gives confidence in the ability of geochemical models to assess long-term mineral reactions for site specific cases. However, further understanding of how to deal with assumptions is crucial. To assess interaction between the sandstone reservoir rock and the shaley intervals, a reactive transport model needs to be developed. Detailed input on the mineralogy of these intervals is required.

Distribution List

(this section shows the initial distribution list)

External	Copies	Internal	Copies

Document Change Record

(this section shows the historical versions, with a short description of the updates)

Version	Nr of pages	Short description of change	Pages

Table of Content

2 Applicable/Reference documents and Abbreviations

2.1 Applicable Documents

(Applicable Documents, including their version, are documents that are the “legal” basis to the work performed)

	Title	Doc nr	Version
AD-01d	Toezegging CATO-2b	FES10036GXDU	2010.08.05
AD-01f	Besluit wijziging project CATO2b	FES1003AQ1FU	2010.09.21
AD-02a	Consortium Agreement	CATO-2-CA	2009.09.07
AD-02b	CATO-2 Consortium Agreement	CATO-2-CA	2010.09.09
AD-03h	Program Plan 2014	CATO2-WP0.A-D03	2013.12.29

2.2 Reference Documents

(Reference Documents are referred to in the document)

	Title	Doc nr	Version/issue	Date

2.3 Abbreviations

(this refers to abbreviations used in this document)

3 Introduction

3.1 Issue addressed

One of the largest worldwide climate issues is the enhanced greenhouse effect due to human emission of vast amounts of CO_2. According to the European Commission and the Dutch government one of the most promising approaches to reduce CO_2 emission into the atmosphere on the mid-term scale is to store CO_2 in geological formations. Depleted natural gas fields represent the most favorable sites for storage. When CO_2 is injected into the subsurface it will partially dissolve in the pore water and subsequently react with the host rock. During the last two decades many studies focussed on the short- and long-term geochemical effects of injected CO_2 on the reservoir rocks. The understanding of short-term effects is important for injectivity, while long-term effects are of main issue for geological containment and for (semi-)permanent trapping in the form of carbonates. Experimental studies investigating geochemical reactions only cover a limited time scale (months to years) and are highly dependent on experimental conditions (Gaus et al., 2008). Geochemical modelling studies, on the other hand, are able to predict the reactions on a much longer time scale (> tens of years) and can be used to assess the effects of varying downhole conditions relatively easily. However, these models are simplifications of complex geological systems and they use thermodynamic databases which are based on extrapolation of experimental studies and on mineral proxies. Therefore, they are prone to significant uncertainties (Dethlefsen et al., 2011). Also, they exclude organic geochemistry. Another way to study long-term mineral reactions induced by the presence of CO_2 is to investigate natural gas fields with significantly high CO_2 concentrations, the so-called natural analogues for CO_2 storage. Worldwide, several natural analogues have studied (e.g. Watson et al., 2004, Worden 2006, Wilkinson et al., 2009, Pudlo et al., 2011 and Liu et al., 2011). These studies show that long-term mineral reactions are site specific, implying that general conclusions on the geochemical effects of CO_2 are not possible. In this study, we investigated a Dutch natural CO_2 analogue for storage in a depleted gas field which is, to a certain extent, representative of many potential Dutch storage sites.

3.2 Werkendam natural analogue

The first Werkendam well (WED-01) was drilled in 1958 and penetrated an oil field in shallow formations. A second exploration well (WED-02) was drilled in 1965 into deep Triassic sandstone formations (NAM exploration well proposal, 1989). The target reservoir was dry. This water-bearing reservoir or aquifer will be referred to as WED2 in this report. Slightly North of well WED-02, the third well (WED-03) was drilled in 1991 and gas was discovered in these Triassic formations. This gas field is also referred to as the Werkendam Deep field and from now on will be referred to as WED3. The gas consists of ~75% CO_2 and ~21% CH_4, with minor other components. It is accumulated in the sandstones of the Röt and Solling Formations (Upper Bunter), which were deposited during Middle Triassic. Many potential CO_2 storage reservoirs in the Netherlands are located in these formations. Hence, WED3 is an important Dutch natural analogue for CO_2 storage. The Barendrecht-Ziedewij gas-field, based on well BRTZ-01, is located ~25 km westward from Werkendam and will be referred to as BRTZ. This field is a CH_4-bearing (~94% CH_4) stratigraphic equivalent of WED3 with very low concentrations of CO_2.

WED3 and BRTZ have basic characteristics in common: (1) Upper Bunter sandstones as reservoir rock, (2) closely located to each other so that a similar primary mineralogy can be assumed if lithofacies are the same (see Chapter 6 for lithofacies), (3) similar reservoir depths. The main difference is that WED3 is a natural analogue and BRTZ is an almost depleted gas field and theoretically a possible candidate for CO_2 storage. The WED2 aquifer in the Upper Bunter is a water-bearing stratigraphic equivalent which is located somewhat deeper than WED3. An overview of the fields used in this study is shown in Table 1 and the locations are shown in the map in Figure 1.

Table 1. Overview and characteristics of the three reservoirs used in this study

Name	Short name	Reservoir type	CO_2 concentration	Use in this study
Werkendam Deep	WED3	CO_2 natural analogue	74.5%	Natural analogue for CO_2 storage
Barendrecht-Ziedewij	BRTZ	Natural gas field	0.8%	CH_4-bearing stratigraphic equivalent
Werkendam aquifer	WED2	Aquifer	-	water-bearing stratigraphic equivalent

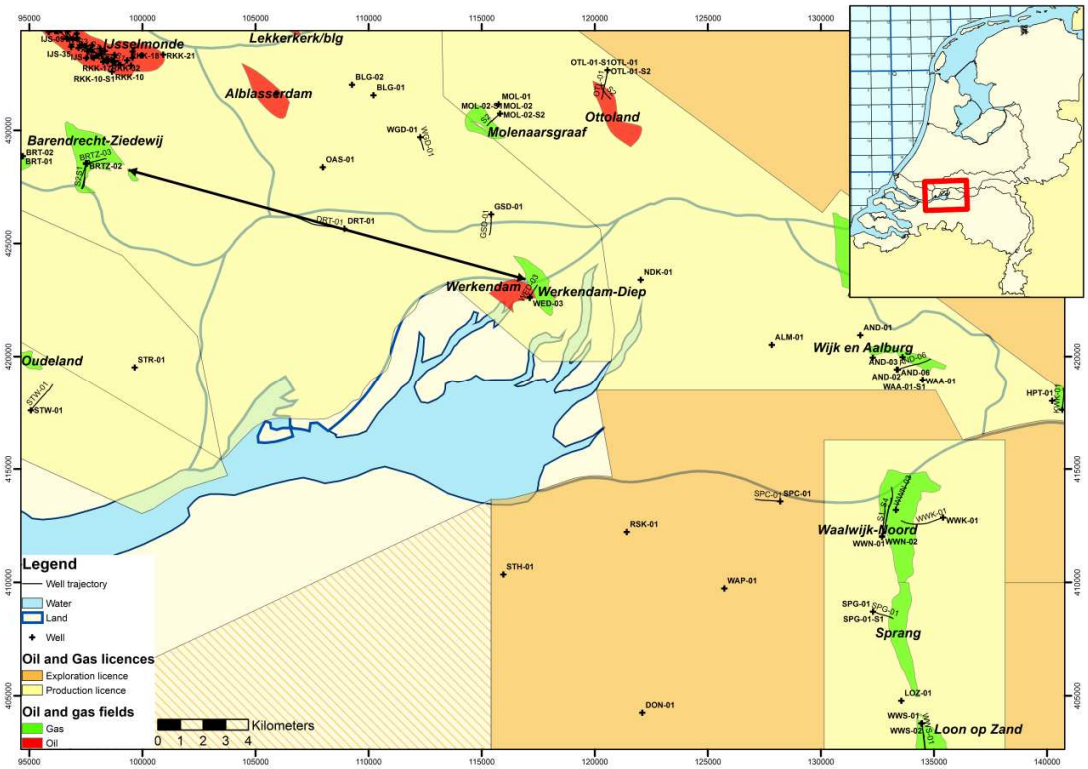

Figure 1. Location of the Werkendam and Barendrecht-Ziedewij gas fields. The Werkendam aquifer is Southwest of, and adjacent to the Werkendam gas field.

3.3 Aim of the study

The main aim of this study is to compare rock samples of the natural analogue for CO_2 storage in depleted gas fields with the aquifer and the CO_2 storage candidate, in order to determine the long-term chemical and mineralogical influence of CO_2 on such reservoir rocks. In this study we investigated and compared rock samples of WED3 with samples of the WED2 aquifer and the BRTZ gas field. The goal was to unravel the diagenetic evolution of each field, define the paragenetic sequence of the sandstones and subsequently compare the different fields and define the mineral reactions in WED3 which occurred due to the presence of CO_2. The main focus is on the comparison of WED3 and BRTZ, since the difference in water saturation between WED2 and WED3 might complicate the comparison. For WED3 and BRTZ basin modelling was performed using wellbore data, and the resulting depth and temperature evolution were used to support the development of the paragenetic sequence.
Additionally, the potential to simulate petrographic observations on CO_2-induced mineral reactions by means of PHREEQC geochemical modelling was investigated.

Supporting laboratory experiments on the geochemical effects of CO_2 on reservoir and caprock are performed within $CATO_2$ and reported in D12 of WP3.3 (Koenen et al., 2014).

4 Methodology

For each of the fields parts of the Triassic Röt Fringe Sandstone Member was cored. This Member is located at 2727-2786 m, 2646-2685 m and 2963-3019 m true vertical depth (TVD) in wells WED-03, BRTZ-01 and WED-02 respectively and constitutes a part of the reservoir intervals for the WED3 and BRTZ gas fields. We selected several sandstone samples from the complete interval of each core, thereby choosing samples with different textures to take into account the heterogeneity of the reservoirs. Whole rock X-ray diffraction (XRD) analyses were performed by PanTerra Geoconsultants B.V. in the Netherlands and SGS Horizon in Canada to determine the (crystalline) mineral content of the samples.
Thin sections of 30 µm thick were prepared by PanTerra Geoconsultants B.V. The thin sections were impregnated with a blue epoxy to indicate the porosity within the samples. The sections were analysed using the following techniques:

- QEMSCAN analyses: QEMSCAN imaging and mineral quantification was performed by SGS Horizon in Canada to address the spatial distribution of minerals and pore space in a 2-dimensional rock section.
- Optical Microscopy: For optical microscopy a Leitz Wetzlar microscope at TNO Utrecht was used. The samples were studied for mineral identification and texture analysis using plane polarized and crossed polarized light.
- Scanning Electron Microscopy (SEM): Back Scattered Electron (BSE) imaging was performed for petrographic analysis using the TESCAN MIRALMH FEG-SEM (TNO Utrecht). This SEM is equipped with and Energy Dispersive X-ray (EDX) spectroscope for semi-quantitative chemical analysis. For CL-imaging we used the Philips XL30S FEG-SEM equipped with a Centaurus CL-detector (K.E. Developments Ltd, Cambridge, UK) at Utrecht University. This CL-detector has a wavelength detection range of 300-650 nm with a peak at 420 nm and is thus most sensitive to blue to violet light. A relatively unknown technique called Charge Contrast Imaging (CCI) was performed using an environmental SEM at the British Geological Survey in Nottingham, UK. With this technique zoning in carbonates and sulfates can be investigated based on minor chemical differences and crystal properties, reflected in differences in surface charge.
  We used BSE-imaging, in combination with EDX chemical analyses, CL-imaging and CC-imaging to determine the paragenetic sequence.

Whole rock carbon and oxygen isotope analysis were performed on selected samples from WED3 and BRTZ by the British Geological Survey (BGS) to assess the origin of different carbonate fractions. The sample selection was based on the siderite and dolomite content as determined from XRD analyses. A set of samples was selected with the highest range in siderite/dolomite ratio so that bulk rock isotope analyses in combination with the siderite and dolomite content could be used to assess the siderite and dolomite isotope values separately. For the selected samples, additional XRD analyses were performed by Qmineral in Leuven, Belgium. The exact same batch of material was subsequently used for the isotope analysis. This was necessary to make sure that the exact carbonate contents were used in the assessment of the isotope values.

Basin modelling was applied to develop a burial history and temperature evolution of WED3 and BRTZ. Potential differences in temperature evolution need to be taken into account when the diagenetic histories of the two fields are compared. To perform 1D modelling of the

burial and temperature history per field, the software PetroMod v11 of the company Schlumberger was used. Basic data requirements for modelling are the present-day geometry, lithological description of the layers based on true vertical depths, the formation properties (e.g. porosity), absolute ages for stratigraphic layers, times of non-deposition and erosion, boundary conditions such as paleo-surface temperature, heat flow and water depth. The model is calibrated using the current temperature, maturity of organic matter and compaction data (Nelskamp and Verweij, 2012). The rock sequence in well BRTZ-01 is cut by two normal faults, cutting out a significant sedimentary sequence. Faults cannot easily be included in the model. To prevent the simulation of severe, false erosion periods we used well BRTZ-03 to determine the burial history of the BRTZ field. It is interpreted that the faults in well WED3 did not result in missing strata.

Geochemical batch modelling was performed using PHREEQC v3 (Parkhurst and Appelo, 2013) in order to simulate the observed CO_2-brine-mineral reactions in WED3. The approach of the modelling was to investigate which model conditions need to be applied to simulate the paragenetic sequence observed in the samples. The BRTZ mineralogy was equilibrated with CO_2 at a high partial pressure to see whether the same mineral reactions would be predicted as observed in WED3.

5 Burial history and the origin of CO_2, CH_4 and oil

5.1 Introduction

There are many hydrocarbon reservoirs present in the subsurface of the Netherlands, including in the West Netherlands Basin (WNB) in the southern part of the Netherlands (Figure 2). During gas and oil exploration and appraisal campaigns the wells BRTZ-01 and WED-03 discovered gas accumulations and WED-02 an aquifer in the sandstones of the Röt and Sölling Members (Upper Buntsandstein) and (part of) the Main Buntsandstein (Volpriehausen and Detfurth Members and Hardegsen Formations). The three reservoirs are all located in the southern part of the WNB. The distance between Barendrecht-Ziedewij and Werkendam is ~25 km (Figure 2). The sediments of the Röt Fringe Sandstone Member, which were deposited during Middle Triassic (~245 Ma), are present in each of the fields. WED3 is located in a block that is normal faulted to the surrounding blocks (Figure 3). The reservoir is sealed by the Muschelkalk / Keuper Members (top). The side seal is provided by the claystones of the Lower Jurassic Aalburg Formation in a fault juxtaposition configuration. Beneath the gas an undeveloped oil rim is present (Figure 3).

5.2 Geological setting of the West Netherlands Basin

The geological architecture and history of the WNB is described in detail in literature (e.g. de Jager 1996, 2003 and 2007). Some key events relevant for this study are reported below.
The WNB is a small inverted basin (De Jager, 2003) located in the southern North Sea area, bounded to the north by the Central Netherlands Basin and the Broad Fourteens Basin and to the south by the London-Brabant Massif (Van Balen et al. 2000) (Figure 2). During the Late Carboniferous (Silesian) organic material was deposited that evolved to the main source rock for CH_4-gas in the Triassic sandstones (De Jager, 1996). At the end of the Carboniferous sedimentation stopped due to uplift. Between Late Permian and Middle Jurassic sedimentation continued and mainly clastic sediments were deposited (De Jager, 1996), including the sediments of the Middle Triassic Röt Fringe Sandstone Member, which represents part of the reservoir rock for the BRTZ and WED3 gas and the aquifer for WED2. The WNB lack the Permian Zechstein salt deposits. Here, the Triassic sediments, which were deposited in eolian, fluvial, lacustrine pralic and shallow marine environments, overly Carboniferous sediments (Geluk, 2005). The lack of Zechstein salt deposits may be an important factor for easy gas migration from the Carboniferous source towards the reservoirs.
The WNB experienced a late Kimmerian rifting event (Late Jurassic – Early Cretaceous) forming the main tectonic elements in the subsurface which are currently present. During this event, the basin was filled with ~2500 m sediments (De Jager, 2007). Tilted half blocks were formed during Late Jurassic rifting; structures that are able to trap gas (De Jager, 1996). The Late Kimmerian rifting event also initiated volcanism in the basin (Sissingh, 2004). During Early Cretaceous the extensional tectonic activity came to an end (De Jager, 1996) and from Late Cretaceous to Early Tertiary the WNB was influenced by the Alpine inversion. Three inversion pulses can be distinguished (Late Cretaceous, Paleocene and Eocene/Oligocene): During the first two inversion pulses pre-existing faults were reversely reactivated. The latest pulse did not cause reactivation of the faults, but only uplift (De Jager, 2007). The amount of uplift within the WNB differs per subarea (Nelskamp and Verweij, 2012). BRTZ, WED2 and WED3 are located in different half blocks (formed during late Jurassic and modified during

Cretaceous/Tertiary inversion). They have a good top seal and sealing lithologies across fault planes (De Jager, 1996), since the gas is still present in the reservoirs.

Figure 4 shows the correlation between the three wells. A thick, clay-rich interval can be observed in the lower part of the Röt Fringe Sandstone Member in each of the wells. For WED this clay rich interval is from approximately 2838 to 2848 m along hole (corresponding to 2747 to 2757 m true vertical depth).

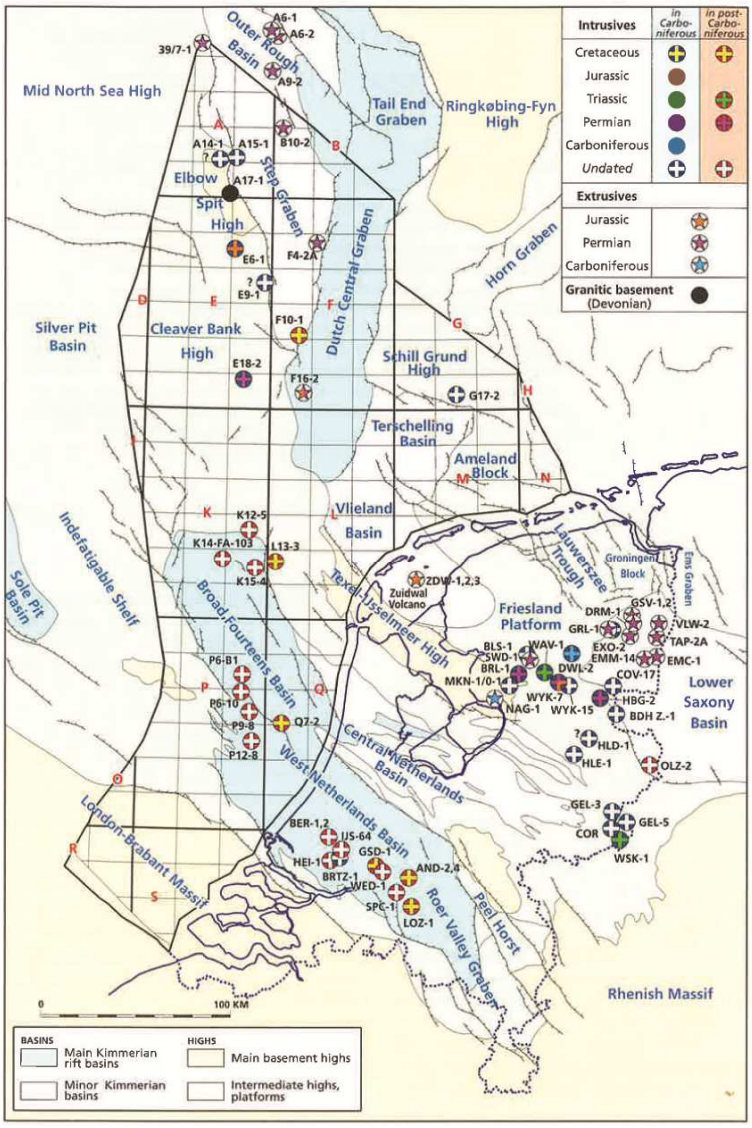

Figure 2. Structural map of the Netherlands. From Van Bergen & Sissing (2007). The WNB is a Kimmerian rift basin attached to the Broad Fourteens Basin and bounded to the south by the London-Brabant Massif and to the north by the Central Netherlands Basin. Wells with volcanic intrusions are indicated. An intrusion is found during drilling of WED-01 and BRTZ-01.

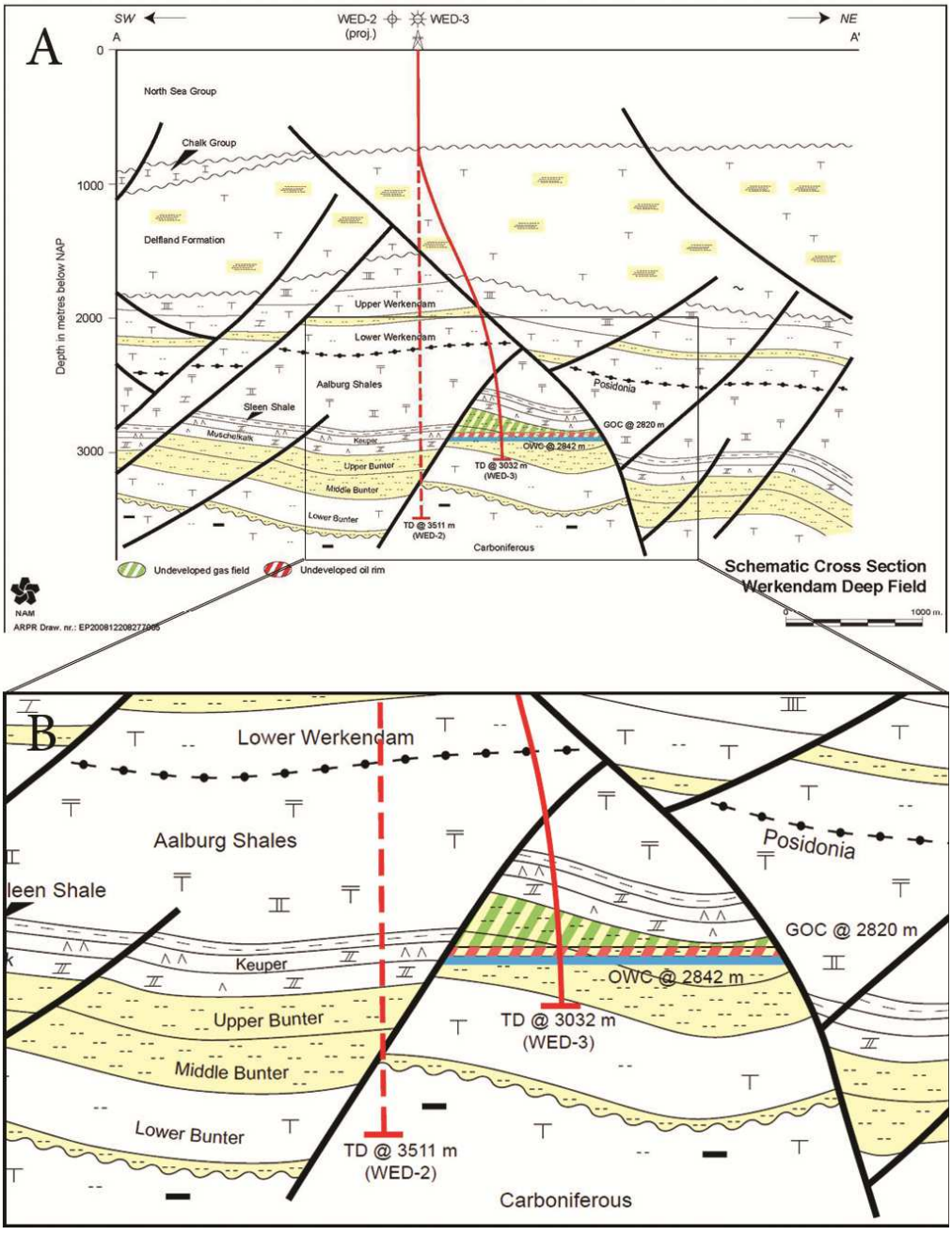

Figure 3. Schematic cross-section of the subsurface of the WED area with wells WED-02 and WED-03 (A) and a close up of the gas reservoir (B) (Source: NAM). The Upper Bunter Formation contains the Röt Members. The gas field and aquifer are separated by a normal fault.

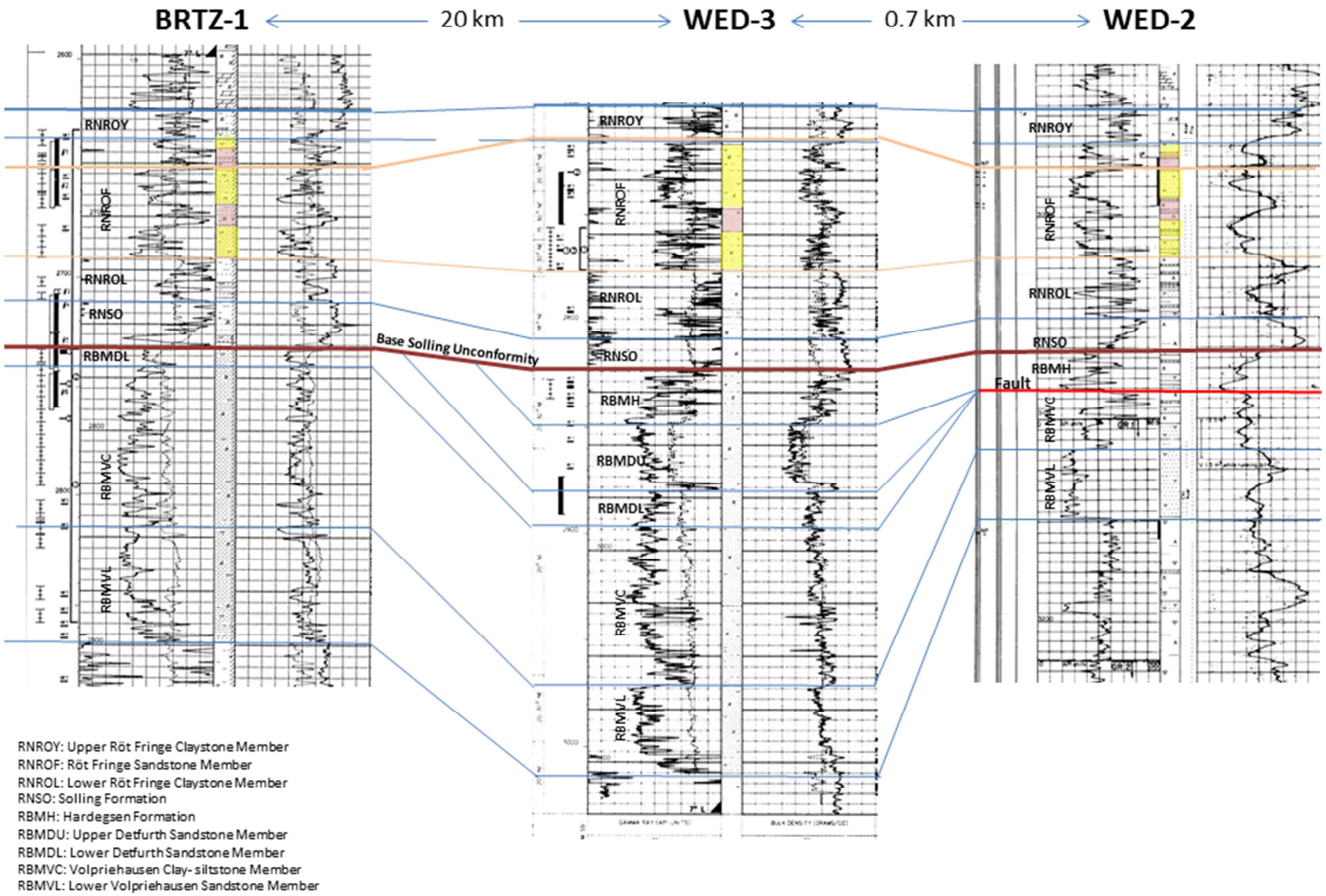

Figure 4. Well correlation for BRTZ-01, WED-03 and WED-02. RNROF represents the Röt Fringe Sandstone Member. A clay-rich interval can be observed in the lower part of the Member in each well.

5.3 Burial history

The basin modelling of WED3 and BRTZ is based on the stratigraphic columns as presented in Appendix A. The resulting burial histories are shown in Figure 5 and in more detail in Appendix A. WED3 experienced major subsidence during Jurassic and Lower Cretaceous. This subsidence can be linked to the Jurassic-Cretaceous rifting event. The amount of subsidence decreased in the Upper Cretaceous, and can be correlated to the end of the rifting. The maximum burial depth of the Röt Fringe Sandstone Member (RNROF in Figure 34) was reached during the Upper Cretaceous and yields >3000 m. At the end of the Cretaceous major inversion of the WED3 field occurred, resulting in a large unconformity. The entire Cretaceous and Paleocene sediment sequence, probably ~900 m thick sediments, is lacking (figure 3). This uplift of approximately 1000 m can be correlated with the first two Alpine inversion pulses. The last inversion pulse occurred at the Eocene/Oligocene boundary and an uplift in the order of 200 m is estimated.
The burial history of BRTZ shows a gradual and slower subsidence of the field. According to the model a small uplift occurred at the Jurassic-Cretaceous boundary. This uplift coincides with the unconformity found in the Middle Jurassic sediment sequence. However this uplift cannot be related to a regional event. In general the WNB subsided during Late Kimmerian rifting (De Jager, 2007). After the small inversion, subsidence of the basin continued and no significant inversion of the reservoir occurred. Only during the last five million years minor uplift occurred.
During Triassic and Paleogene/Neogene the burial history is more or less comparable between the two fields. During Jurassic and Cretaceous times they differ significantly. The Röt Fringe Sandstone Member in WED3 experienced greater subsidence and subsequently major inversion.

The temperature evolution corresponds to the burial history of the sandstones (Figure 5). The calibration of the present-day temperature is quite reliable. Well BRTZ-03 shows modeled present-day temperatures which are slightly too high (Appendix A). A reduction in present-day heat flow or differences in thermal conductivity or radiogenic heat generation of the sediments could influence the calibration. Vitrinite reflectance measurements were only available for well WED-03. The measurements show a past temperature event, because the vitrinites show a higher reflectivity than is expected based on the present-day temperature (Appendix A). The vitrinite reflectance combined with the unconformity in the Cretaceous suggest a large erosion event in combination with a burial anomaly. Either an erosion event or a higher heat flow could be included to correct for the high vitrinite reflectance measurements. The Röt Fringe Sandstone Member in WED3 and BRTZ experienced a maximum temperature of ~140°C and ~120°C respectively based on uncorrected temperature. For WED3 the maximum temperature is probably somewhat higher, as shown by the vitrinite reflectance.

Basin modeling was not performed for WED2 since the main focus in this study is on the comparison of WED3 and BRTZ. However, the lithostratigraphy of WED2 shows a similar unconformity with most Cretaceous deposits missing in the sequence. This suggests a similar major uplift of the reservoir rock as WED3 during the late Cretaceous.

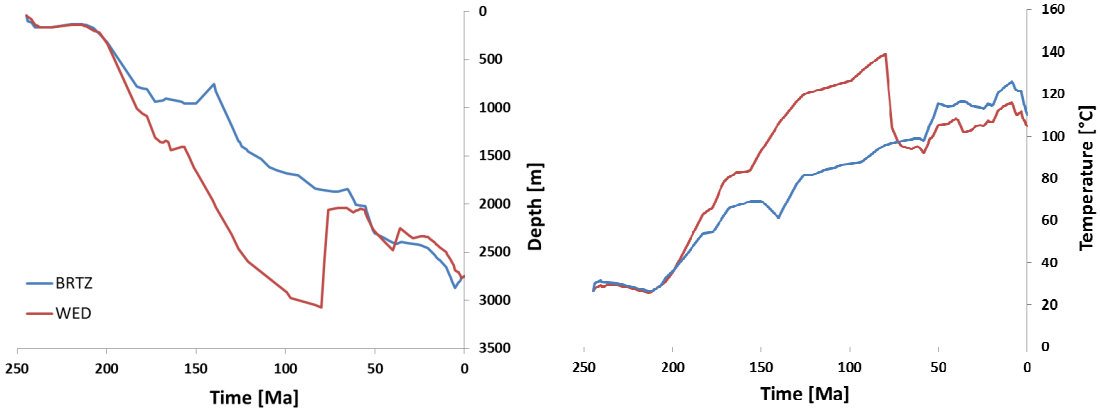

Figure 5. Burial and temperature evolution of the Röt Fringe Sandstone Member in BRTZ-03 and WED-03.

5.4 Gas composition and isotope data

The gas composition and isotope ratios of the BRTZ and the WED3 gas are shown in Table 2. For WED3 one measurement was performed on gas samples from the Röt Fringe Sandstone Member and one from the Hardegsen Formation. The measurement in BRTZ was on gas from either the Sölling or Detfurth Member. This is not clear from the data provided with the sample analysis. The isotope data is based on one measurement for each field.

Carbon isotope ratios are generally defined by the following equation:

$$\delta^{13}C = \left(\frac{\left(\frac{^{13}C}{^{12}C}\right)_{sample}}{\left(\frac{^{13}C}{^{12}C}\right)_{standard}} - 1 \right) * 1000‰$$

The $^{13}C/^{12}C$ standard is generally Pee Dee Belemnite (PDB), which is a Cretaceous marine fossil with a high $^{13}C/^{12}C$ ratio close to 0. Most natural materials have a negative value.

5.4.1 Origin of CO_2

Previous studies on natural analogues have shown that the CO_2 in CO_2-rich reservoirs can have various origins (e.g. Clayton et al. 1990; Sherwood Lollar et al. 1997; Wilkinson et al. 2009). Different carbon sources have a distinct range of $\delta^{13}C_{CO2}$ values. Whycherley et al. (1999) summarized seven possible sources for CO_2-gas and their corresponding $\delta^{13}C_{CO2}$ ranges (Table 3). The $\delta^{13}C_{CO2}$ value of -4.4‰ PDB for WED3 matches with four sources; 1) Magmatic origin; 2) Regional metamorphism; 3) Contact metamorphism of carbonates and 4) Biogenic decay. Biogenic decay generally produces small amounts of CO_2 (e.g. Wycherley et al., 1999 and Zhang et al.2008). CO_2 in large accumulations have relatively heavy stable carbon isotope signatures (between 0 and -10‰ PDB), suggesting an inorganic origin as a result of either metamorphic reactions at greater depth or from magmagenesis (Wycherley et

Table 2. Gas compositions and isotope data for WED3 and BRTZ. Source: www.nlog.nl.

	WED3		BRTZ		WED3	BRTZ
	Röt Fringe	Hardegsen	Sölling/Detfurth		Hardegsen	Sölling/Detfurth
CO_2 (%)	72.0	77.1	0.8	$\delta^{13}C_{CH4}$ (‰)	-33.8	-29.5
CH_4 (%)	23.5	19.7	93.9	$\delta^{13}C_{CO2}$ (‰)	-4.4	-
C_2H_6 (%)	0.6	0.5	3.2	$\delta^{13}C_{C2H4}$ (‰)	-	-24.4
N_2 (%)	3.6	2.3	0.9	δD_{CH4} (‰)	-	-151
				$\delta^{18}O_{CO2}$ (‰)	23.8	-
				$\delta^{15}N_{N2}$ (‰)	-4	-

Table 3. Carbon isotope ranges for specific CO_2 sources. Reference?

Nr.	Process	$\delta^{13}C_{CO2}$ value (‰)
1.	Magmatic origin / mantle degassing	-4 to -7
2.	Regional metamorphism	0 to -10
3.	Contact metamorphism of carbonates	-2 to -12
4.	Marine Carbonates	+2 to -2
5.	Biogenic decay	15 to -30
6.	Breakdown of coaly kerogen type III	-10 to -25
7.	Contact metamorphism of coals	-10 to -20

al. 1999). Regional metamorphism as CO_2 source is not straightforward, since the WNB was not involved in a continent-continent collision or in a subduction related process. There are two remaining possible sources for the CO_2 gas in the WED3 field: 1) Magmatic origin / mantle degassing and/or 2) Contact metamorphism of carbonates. (1999). Noble gas isotopes would be required to further distinguish between these two origins but these are not available. Furthermore, mixing of two sources, or more, is also a possibility. The two possible sources are further discussed in the following sections.

The BRTZ gas contains <1 mol% CO_2. A specific origin for the CO_2 in the BRTZ field cannot be determined, because the $\delta^{13}C_{CO2}$-value is not measured. However, most natural gas accumulations contain small amounts of CO_2 (<10 vol.%) and predominantly have an organic origin (Wycherly et al. 1999).

Magmatic origin

Volcanic rocks linked to several stages of magmatic activity are found in the Dutch sub-surface, including the WNB (van Bergen & Sissigh, 2007) (Figure 2). During Late Kimmerian rifting, volcanism mainly occurred in the WNB, Broad Fourteens Basin and Roer Valley Graben (Figure 2). In the area of WED3, several intrusions of volcanic rocks are registered which are dated aroun 130 Ma (Sissingh, 2004). According to Sissingh (2004) the West Netherlands Igneous Centre (WNB, Broad Fourteens Basin and Roer Valley Graben) is Early Cretaceous in age (140 -130 Ma). These intrusions are characterized by nephelinite and basanites. This was the main volcanic period observed in the WNB. If the CO_2 gas was generated by volcanic activity, it probably occurred around this time. This is after the formation of the tilted fault blocks that form the gas traps. However the timing of CO_2 generation and accumulation within WED3 is not necessarily the same. Migration of gas along dense rocks can take millions of years (Van Balen et al. 2000) and the gas may have been trapped in other structures, before it was released and accumulated in WED3.

Contact metamorphism of carbonates

Based on the $\delta^{13}C_{CO2}$ value it is possible that the CO_2 has a metamorphic origin. Metamorphism of carbonates may be initiated during the Late Kimmerian rifting. The temperature in the crust increased, even initiating volcanism (Sissingh, 2004). Increased temperatures due magma migration through carbonate rocks may have caused contact metamorphism of these rocks below the WED3 reservoir, thereby releasing CO_2 from carbonate minerals. Major heating of shale-carbonate sequences could result in continuous CO_2 loss due to devolatization reactions (Jamtveit et al. 1991). The reactions that cause the release of CO_2 take place at temperatures > 500°C and are accompanied by regionally migrating fluids (Ague and Rye, 1999). For example within the Oslo Rift, Norway, major CO_2 release occurred during contact metamorphism of carbonates (Jamtveit et al. 1991).
Within the WED3 area the CO_2 may be released from the Lower Carboniferous Dinantian limestone sequence during contact metamorphism. The Dinantian limestone is the only large limestone sequence in the WNB below the Triassic reservoirs (De Jager, 1996). However, in literature neither large heat sources nor rocks that experienced contact metamorphism in the WED3 area were found. Only small scale intrusions are present, and those do not occur in limestone. According to Ague and Rye (1999) the CO_2 released during contact metamorphism does not migrate upward, but is dissolved and transported by fluids.

Lack of convincing evidence, indicates that the origin of the CO_2 is probably not metamorphic. Since evidence of volcanism is found close to the WED3 field, the CO_2 release is probably caused by magma/mantle degassing. This gives an upper age constraint of ~130 Ma for CO_2 accumulation. The question remains why the WED3 field is the only field with the high CO_2 accumulation, while close to other gas accumulations also magmatic intrusions were found.

5.4.2 Origin of methane and oil

Two main source rocks have been identified for oil and gas in the WNB: the Carboniferous coals and carbonaceous claystones of the Westphalian A and B, and the Early Jurassic Posidonia Shale (De Jager et al. 1996 and Van Balen et al. 2000). Gas and oil generation and charging were modelled for the whole WNB (De Jager et al. 1996). The results predicted that Carboniferous gas generation from the thick Westphalian coal measures started during Early Jurassic, before the formation of reservoir-seal structures, and continued till Late Tertiary. Acceleration of generation at ~160 Ma during the Late Jurassic was related to an increase in burial rate and heat flow due to rifting (Van Balen et al. 2000). Also significant amounts of oil were generated from Carboniferous source rock.
Trap formations in Triassic Bunter sandstones were formed during the Late Jurassic rifting phase, indicating that hydrocarbon charge occurred from then on. After the rifting ceased during Mid-Cretaceous, the generation decreased but did not stop completely until the end of the Tertiary (De Jager et al. 1996). According to Van Balen et al. (2000) the filling of the gas traps on the SW margin of the WNB with Carboniferous gas occurred between 160-120 Ma. This is before the inversion (Figure 34) of the WED3 reservoir.
The Posidonia Shale was deposited in the Early Jurassic. Hydrocarbon generation started during the Late Jurassic and occurred until late Tertiary. The larger part of the hydrocarbons were generated before trap formation during the Late Cretaceous inversion and were therefore lost to the surface. Significant amounts of oil from the Posidonia were generated and they are mainly trapped in Jurassic and Cretaceous reservoirs.
Loss of hydrocarbons probably occurred during Late Cretaceous inversion episodes. Therefore, the Triassic traps that have had no access to Tertiary hydrocarbon charge after inversion are probably underfilled (De Jager, 1996).

In general, most Carboniferous hydrocarbons (predominantly gas but also oil) has accumulated in the Triassic traps, while Posidonia hydrocarbons (predominantly oil) accumulated in the shallower Jurassic and Cretaceous reservoirs (de Jager et al., 1996 and van Balen et al., 2000). However, the complex geological history of the WNB with tilted fault blocks allowed the occasional juxtaposition or downfaulting of Posidonia next to or below Triassic trap structures. Hence, Carboniferous oil and gas could have migrated into shallower formations.

The BRTZ and the WED3 field contain ~94% and ~24% CH_4 respectively. Methane in most Triassic reservoirs originates from Westphalian (Carboniferous) rocks. In some cases, when the Posidonia shale is down faulted to levels below the Triassic reservoir rocks, mixing with Jurassic Posidonia shale gas is possible, (De Jager, 1996).

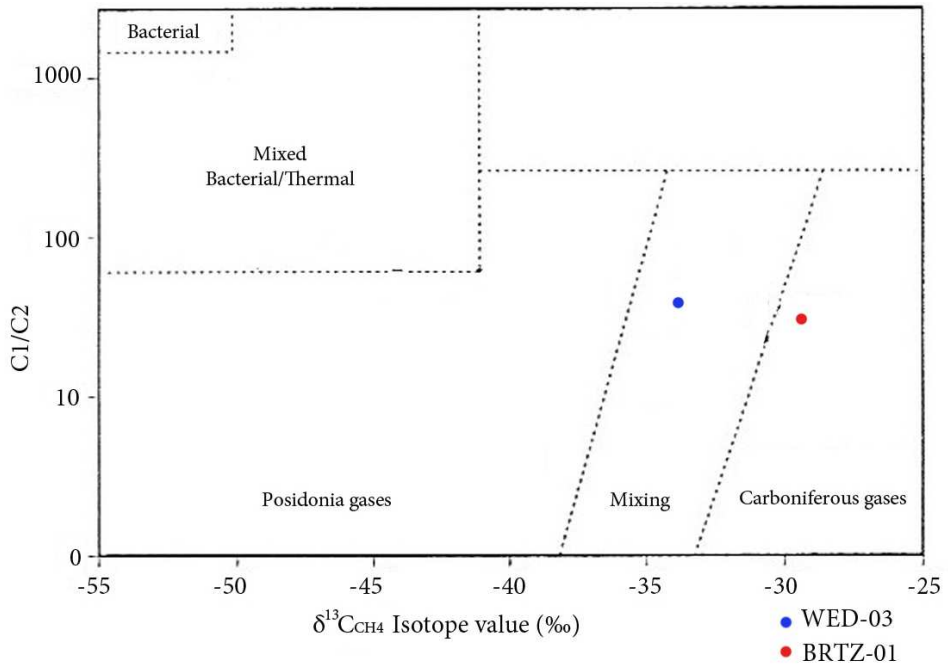

Figure 6. Diagram showing the different origins of CH_4 based on the $\delta 13C_{CH4}$-value and the C1/C2 ratio (methane/ethane ratio). Modified from De Jager et al. (1996).

Figure 6 shows a diagram which is often used to determine the origin of CH_4 for the gas reservoirs in the WNB. The $\delta^{13}C_{CH4}$ value for BRTZ, combined with the methane/ethane ratio falls nicely in the field for Carboniferous gas origin. On the other hand, the WED3 $\delta^{13}C_{CH4}$ value and methane/ethane ratio plot within the mixing area, suggesting that the gas in the WED3 reservoir also contains methane derived from the Posidonia shale. Nowadays the Posidonia shale is not faulted to depths below the WED3 field. However before the Alpine inversion events the Posidonia shale could have been located below the reservoir. Another possibility is that some CH_4 in the WED3 field has the same origin as the CO_2. Unfortunately

large variations in $\delta 13C_{CH4}$-values of mantle derived CH_4 does not give the opportunity to be conclusive (Schoell, 1988).
An oil rim is present below the gas cap in WED3 (Figure 3). Within the WNB three groups of oil have been recognized, based on their geochemical characteristics. The oil is either from Posidonia shale, from Westphalian coal, or mixed source. The oil found in Triassic reservoirs is generally from Carboniferous source rocks or mixed with oil from Posidonia shale if faulting has juxtaposed the Posidonia with the Bunter sandstones or if the Posidonia was brought to even deeper levels (De Jager et al., 1996). With regard to WED3, the oil composition is not known or available. Hence, we do not know whether mixing has occurred.
However, if Posidonia gas and oil are present in the Werkendam field, they must have accumulated in the reservoir before the main inversion, since the reservoir had no access to hydrocarbon charge from the Posidonia shale after inversion.

5.5 Summary and relative timing

Figure 7 gives a summary of the geological and hydrocarbon histories for the BRTZ and WED3 field. The timing of source rock deposition, Röt Fringe Sandstone deposition, Late Kimmerian rifting and trap formation are similar for both fields. As discussed above the main differences between both areas are the inversion events, the hydrocarbon history and the generation of the CO_2. The timing of the CO_2 accumulation in the WED3 field remains unclear.

Geological History Barendrecht Ziedewij area

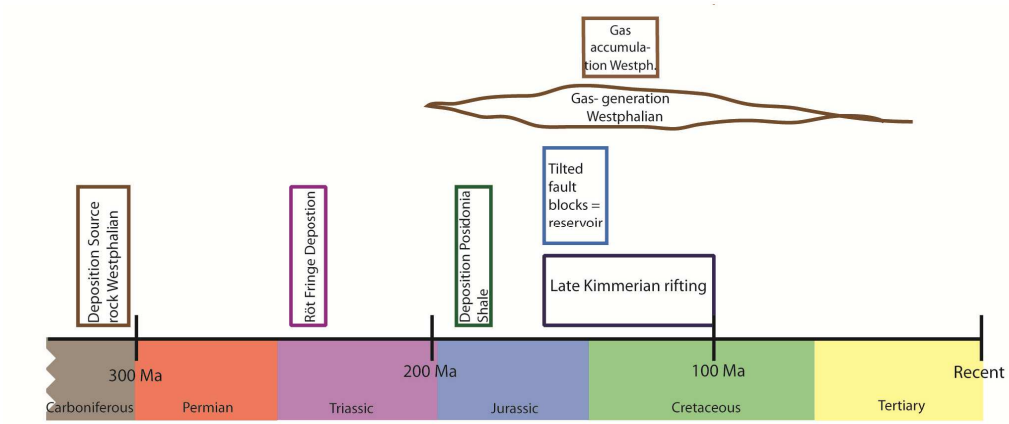

Geological History Werkendam area

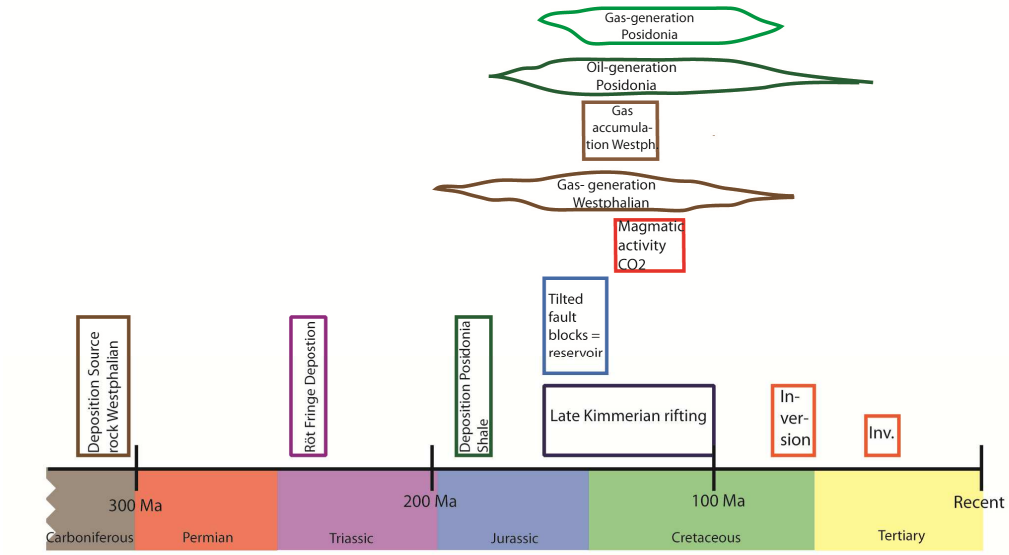

Figure 7. Schematic geological history of the BRTZ field and the WED3 field. The main geological events are placed within a time frame. Note the complexity of the hydrocarbon history and inversion history in the WED3 area. The CO_2 is probably generated during magmatic activity between 130-140Ma. Accumulation of CO_2 in the WED3 field remains unclear but might be related to inversion events.

6 Mineralogy and petrography

6.1 Background on diagenesis

After deposition sediments are subjected to chemical and textural reorganization due to processes such as compaction, cementation, mineral replacement and mineral dissolution (e.g. Worden and Burley, 2003; Milliken, 2005). The general term for these processes at temperatures below 180 to 250°C is diagenesis (Berner, 1980). Three stages of diagenesis can be distinguished; the eogenetic stage (near surface), the mesogenetic stage (burial) and the telogenetic stage (uplift) (Berner, 1980). During diagenesis all chemical processes, including mineral dissolution and precipitation reactions involve interactions between the rock and pore fluid (Milliken, 2005). The microstructural characteristics that develop during diagenesis may give an indication of the depositional environment and the chemistry of the fluids that percolated through the rocks during burial (Harwood, 1988). The timing of diagenetic events during burial is called paragenetic sequence (Harwood, 1988). The influx of large amounts of CH_4-gas will expel pore fluids, and limited amounts of CH_4 dissolve in the pore fluids. The dissolution of CH_4 has negligible effects on pH. The introduction of both gas and oil in a reservoir often decelerates the diagenetic processes (Yurkova,1970).

Since CO_2 storage is suggested as possible solution to reduce the greenhouse effect, the geochemical effects of CO_2 potential for permanent sequestration in rocks is extensively studied (e.g. Wilkinson et al. 2009; Zerai et al. 2005; Hellevang et al. 2005). After injection, CO_2 partially dissolves in the pore fluids, forms carbonic acid and hence lowers the pH, by the following reactions:

$$CO_2\ (aq) + H_2O \leftrightarrow H_2CO_3 \leftrightarrow H^+ + HCO_3^- \leftrightarrow 2H^+ + CO_3^{2-}$$

As a result, the equilibrium stage between minerals and pore fluids changes. The solubility of CO_2 in the pore fluids depends on the activity and the fugacity of the gas (Hellevang et al. 2005), on temperature, but also on the composition and ionic strength of the formation water. An increased ionic strength and a high amount of total dissolved solids will lower the solubility. Elevated CO_2 pressure usually leads to increased acidity of the pore fluids (Worden and Burley, 2003). On the short-term, carbonate minerals dissolve to buffer the pH in the pore fluids (Zerai et al. 2006). On the long-term aluminosilicate dissolution will become more important in the buffering process, thereby liberating cations in the formation water (Zerai et al. 2005). As a result, carbonate minerals can (re-)precipitate using the liberated cations, thereby trapping (sequestering) parts of the CO_2 (e.g. Liu et al., 2011; Wilkinson et al., 2009). The amount and type of reactive aluminosilicates is therefore a crucial parameter in the sequestration process of CO_2.
Pore-filling carbonate minerals, such as calcite, dolomite and siderite commonly form during diagenesis. The CO_2 source is often organic material that disintegrates upon burial. Hence, carbonates are not necessarily the result of high CO_2 concentrations (Wilkinson et al. 2009). The mineral dawsonite ($NaAlCO_3(OH)_2$) is one of the best-known, controversial, and most studied minerals that might form due to increased CO_2 concentrations (e.g. Wilkinson et al. 2009; Hellevang et al. 2005; Worden, 2006; Zerai et al. 2006). Worden (2006) found rocks with up to 8 vol% dawsonite that precipitated under conditions of elevated partial pressure of CO_2. Dawsonite can precipitate at the expense of detrital albite (Worden, 2006), a reaction that can be defined by the following reaction (Zerai et al. 2006):

$NaAlSi_3O_8 + CO_2 + H_2O \rightarrow NaAlCO_3(OH)_2 + 3\ SiO_2$ (aq)

Geochemical models often predict large amounts of CO_2 trapping in dawsonite due to the availability of albite, or high sodium concentrations in the formation water, in combination with other aluminosilicates to provide aluminium. However it is still questionable whether dawsonite sequesters CO_2 for millions of years. According to Hellevang et al. (2005) and Hellevang et al. (2011), the long-term sequestration of CO_2 in dawsonite depends on many parameters. Dawsonite is rarely observed in natural CO_2 reservoirs all over the world. Case studies on natural CO_2 reservoirs in Great-Britain pointed out that long-term CO_2 sequestration in carbonate minerals is relatively small (Wilkinson et al. 2009 and Lu et al. 2011). The same conclusion was obtained from investigation of several natural analogues in North America, China and Europe (Gilfillan et al., 2009).

6.2 Samples

The Röt Fringe Sandstone Member is cored in the WED2, WED3 and BRTZ wells. This Member predominantly consists of greyish/beige sandstones and grey/brown/red clay/siltstone intervals. Samples have been selected from each of the cores. Photographs of the WED3 and BRTZ Röt Fringe Sandstone cores and locations of the selected samples are shown in Appendix B. Figure 8 shows a selection of the rock samples that were taken from the three different fields. In Table 4 an overview is given of the samples and corresponding analyses performed in this project. Twenty Röt Fringe Sandstone samples were taken from the WED3 core (Appendix B), 13 from BRTZ and 6 from WED2. Of these samples, respectively 15, 10 and 5 are sandstone samples which were used for this study. The remaining samples (the missing sample numbers in the table) are shale-rich samples, which were not used in the current study. The WED3 samples at depth greater than 2837m are from the clay-rich interval (Figure 4).

Porosity and permeability values for samples of the three reservoirs are taken from www.nlog.nl. The porosity values vary considerable between 1 and 20% for all three fields, whereas the horizontal permeability values range between <0.01 and 600 mD for WED 3 and BRTZ but are very consistent at ~0.5 mD for WED 2 (Figure 9 and Figure 13). For WED 3 the porosity and permeability values are intermediate (5-15% and 0.5-200 mD respectively) between 14 and 26 m below the top of the Röt Fringe Sandstone Member and decrease to significantly lower values at greater depth (Figure 12). All samples below WED 3.5 (see Table 4) are attributed to a region with low porosity (< 3%) and permeability (< 0.1 mD). This region at the bottom of the core corresponds to the clay-rich interval identified in the well log (Figure 4). For BRTZ only samples from the top to a depth of 17 m are measured. Both the porosity and permeability values vary over the total depth range without significant trend. For WED2 the porosity values increase between 8 and 22 m and then decrease at greater depths, corresponding to the clay-rich interval (Figure 4).

The lithofacies and lithofacies association of the Röt Fringe sandstones from WED3 and BRTZ were determined for several core intervals by Pestman (1991) and Schöbel (1993), respectively. According to Schöbel (1993) the sediments of the BRTZ samples selected for this study were interpreted to be fluvial channel deposits. The sediments from selected WED3 samples are probably fluvial channel deposits, or desert plain sediments intercalated with sheet flood deposits (Pestman, 1991). The clay-rich interval at a depth greater than

2833/2837 m most probably represent another lithofacies. Lithofacies were not reported for WED2.

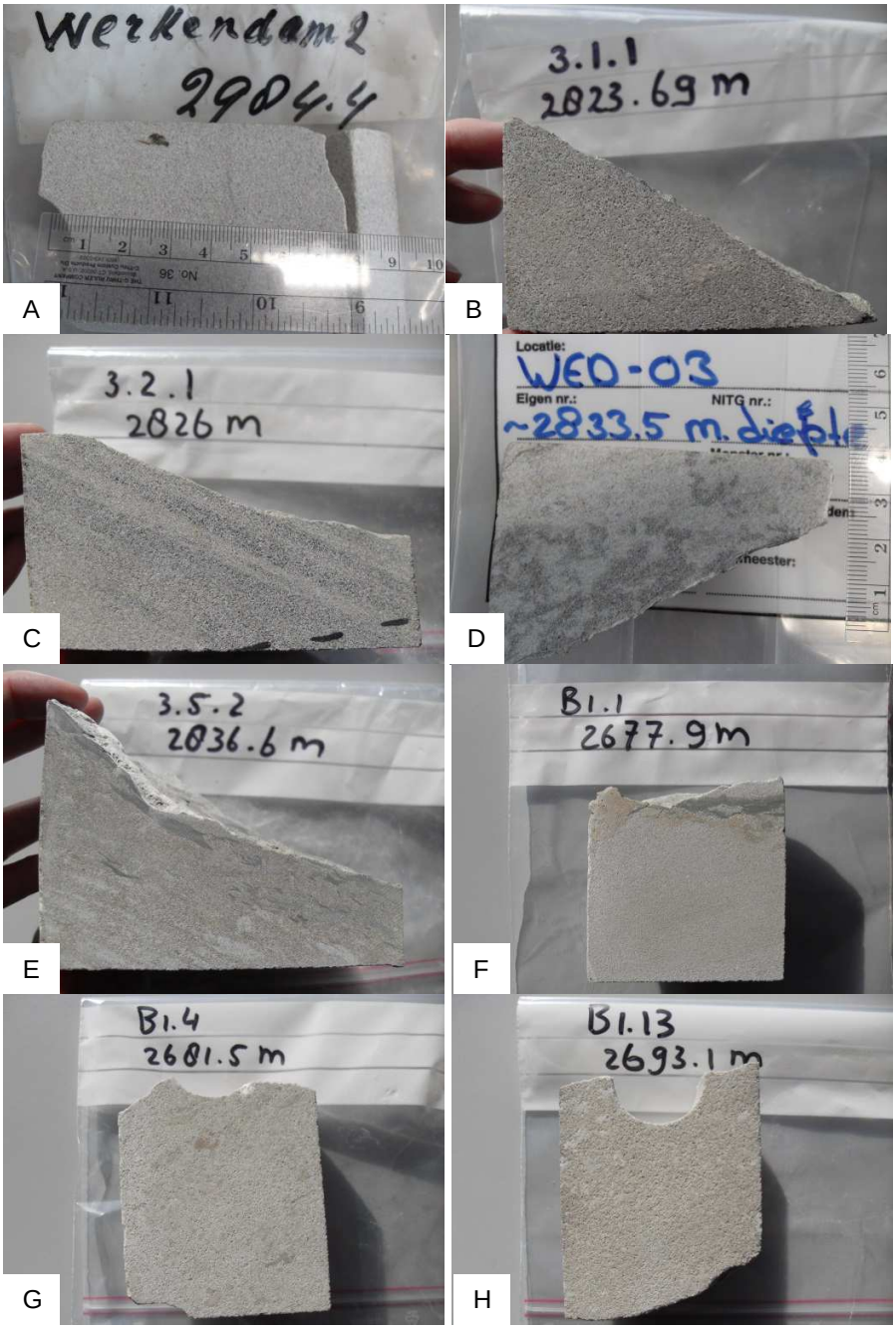

Figure 8. Selection of sample photos, showing the diversity in rock textures. A scale bar is visible in a few photos. All samples are several centimetres wide and long. A: WED2.4, B: WED3.1.1, C: WED3.2.1, D: WED3.5, E: WED3.5.2, F: B1.1, G: B1.4, H: B1.13.

*Table 4. Selected sandstone samples. 'Missing' sample numbers (e.g. WED 3.6) refer to shaley samples, which are not studied within this project. * Samples within clay-rich interval as shown in Figure 4.*

Sample	Depth in m along hole	Lithofacies	SEM	CL	XRD	bulk C13
WED3.1	2821.5	Sheetflood			SGS/Qmin	X
WED3.1.1	2823.7	Sheetflood				
WED3.2	2824.2	Sheetflood			SGS/Qmin	X
WED3.2.1	2826.0	Possibly braided fluvial deposits	X			
WED3.3	2827.0	Possibly braided fluvial deposits	X		SGS/Qmin	X
WED3.3.1	2827.0	Possibly braided fluvial deposits	X		Panterra	X
WED3.3.2	2830.1	Braided fluvial deposits	X		Panterra	
WED3.4	2831.0	Braided fluvial deposits	X		SGS	
WED3.4.1	2832.1	Braided fluvial deposits	X	X	Panterra/Qmin	X
WED3.4.2	2832.8	Braided fluvial deposits	X		Panterra	
WED 3.5	2833.5	Braided fluvial deposits	X	X	SGS	
WED3.5.2	2836.6	Possibly braided fluvial deposits	X		Panterra/Qmin	X
WED3.6.1*	2839.3	Possibly braided fluvial deposits			Qmin	X
WED3.6.3*	2840.4	Possibly braided fluvial deposits				
WED3.6.5*	2844.2	Unknown			Qmin	X
B1.1	2677.9	Possibly braided fluvial deposits			Panterra/Qmin	X
B1.3	2679.7	Possibly braided fluvial deposits	X	X	Panterra/Qmin	X
B1.4	2681.5	Braided fluvial deposits			Panterra	
B1.5	2683.3	Braided fluvial deposits	X		Panterra	
B1.6	2685.1	Braided fluvial deposits	X		Panterra	
B1.8	2685.6	Braided fluvial deposits	X		Panterra	
B1.9	2685.8	Braided fluvial deposits			Panterra	
B1.10	2688.4	Braided fluvial deposits	X	X	Panterra/Qmin	X
B1.13	2693.1	Braided fluvial deposits	X		Panterra/Qmin	X
WED2.1	2976.2	?	X		SGS	
WED2.2	2979.8	?	X		SGS	
WED2.3	2980.7	?	X		SGS	
WED2.4	2984.4	?	X		SGS	
WED2.5	2986.0	?	X		SGS	

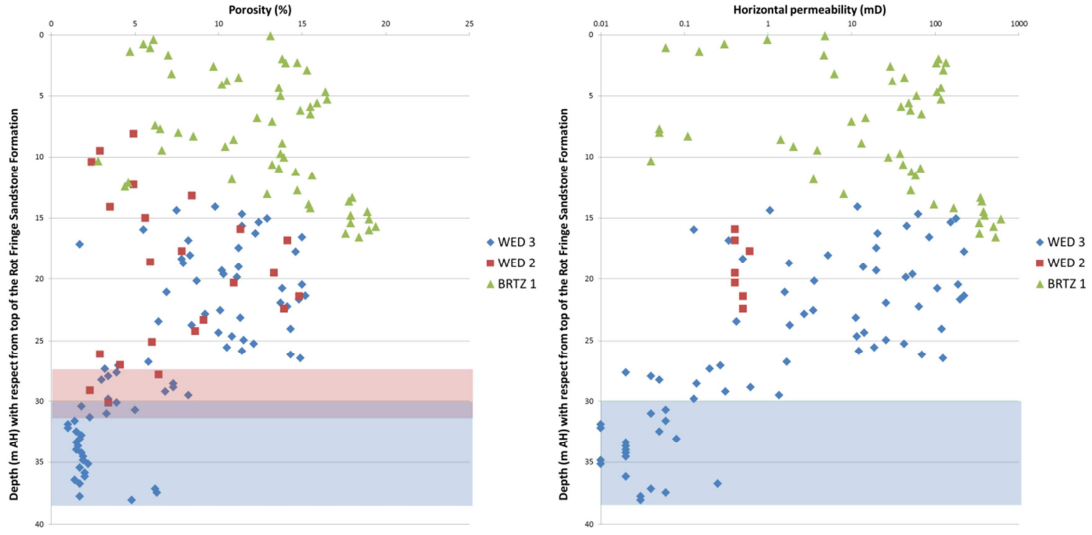

Figure 9. Porosity (%) and horizontal permeability (mD) as a function of depth below top of the Röt Fringe Sandstone Member for WED 3, WED 2 and BRTZ 1. Top of Röt Fringe Sandstone Member is 2807 m, 2963 m and 2660 m along hole (AH) for the fields, respectively. The blue and red boxes represent the clay-rich intervals for WED3 and WED2 respectively. The clay-rich interval of BRTZ is not cored.

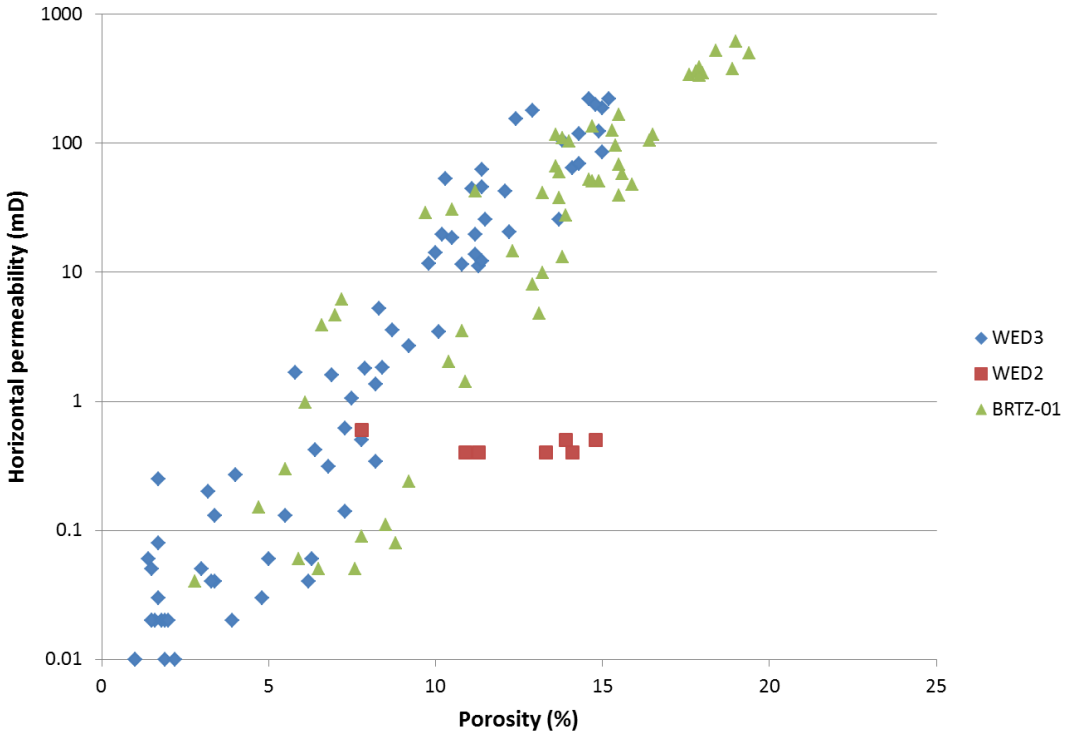

Figure 10. Porosity (%) versus horizontal permeability (mD) for WED3, WED2 and BRTZ.

6.3 Results

6.3.1 XRD and QEMSCAN

The XRD and QEMSCAN results are shown in **Error! Reference source not found.** and summarized in Table 5. The sandstones of the three fields contain mostly quartz, with highly variable amounts of K-feldspar, plagioclase, illite, kaolinite, dolomite, siderite and anhydrite.
We observed that the total quartz, plagioclase and K-feldspar content seem to depend on the laboratory which performed the analysis. Both Panterra and Qmineral calculated higher K-feldspar than plagioclase contents for each of the samples they analyzed, while SGS Horizon obtained systematically higher amounts of plagioclase than K-feldspar. For the samples of WED2 SGS Horizon did not measure any K-feldspar at all. SGS calculated very high quartz content, while Qmineral calculated very low quartz content. Despite the laboratory dependency in quantification of the mineralogy, several differences can be observed between the fields.

Silicates (quartz, feldspar, clay minerals)
BRTZ has the lowest quartz and plagioclase and highest K-feldspar content, while WED2 has highest quartz and lowest K-feldspar. WED3 has intermediate quartz and K-feldspar and highest plagioclase contents (Table 5). All BRTZ samples contain significant amounts of kaolinite, while this clay mineral is completely absent from the WED2 and WED3 samples which contain only illite as a clay phase. WED2 shows variable illite content, which is probably due to the local presence of large clay clasts.

Carbonates (dolomite, ankerite and siderite)
The three fields contain significant amounts of dolomite. The highest total dolomite content can be found in WED2. The samples from WED3 have the highest siderite content (Table 5), and a higher iron content of the dolomite/ankerite compared to BRTZ (Figure 11). In WED2 siderite was not observed in any of the samples. Note that the carbonate mineral dawsonite ($NaAlCO_3(OH)_2$) was not detected within any of the samples.

Sulfates and sulfides
Anhydrite is present in the three fields. The content is highly variable, with values between 0 and 28 wt% (**Error! Reference source not found.**). On average, the content is highest in BRTZ (Table 5). In the analyses by Qmineral barite ($BaSO_4$) was measured in several WED3 samples, but was absent for all BRTZ samples (**Error! Reference source not found.**). Small amounts of pyrite are identified by Qmineral.

Oxides
In the analyses by Qmineral anatase (TiO_2) was measured in several WED3 samples, but not in any of the BRTZ samples (**Error! Reference source not found.**). Iron oxides were not identified by XRD.

Table 5. Average mineral content (wt%) for the three fields based on XRD by Panterra, SGS Horizon, Qmineral and/or QEMSCAN. For the analyses from Qmineral applies that dolomite includes the three ankerite variants. The 2:1 clay minerals are assumed to be illite (Table 11). Note that the QEMSCAN analyses are best compared to the results from Qmineral.

Laboratory	Field	Quartz	Plagioclase	K-feldspar	Total feldspar	Illite	Kaolinite	Dolomite	Siderite	Anhydrite
Qmin	WED3	57.00	6.53	9.84	16.37	15.06	0	4.11	3.19	2.42
Panterra	WED3	79.40	2.00	10	12.00	3.80	0	3.80	0.60	0.40
SGS	WED3	79.64	6.90	2.69	9.59	6.42	0	1.80	0.92	1.63
All XRD	**WED3**	**70.25**	**5.31**	**7.78**	**13.09**	**9.21**	**0**	**3.34**	**2.00**	**1.59**
QEMSCAN	WED3	63.24	6.77	10.35	17.12	9.85	0.10	1.82	2.55	1.98
Qmin	BRTZ	61.93	1.74	13.72	15.46	5.42	3.72	2.71	1.06	8.96
Panterra	BRTZ	67.89	0.67	11.56	12.22	4.11	5.22	4.11	0.22	6.22
All XRD	**BRTZ**	**66.06**	**1.30**	**12.22**	**13.22**	**4.51**	**4.76**	**3.99**	**0.57**	**7.07**
QEMSCAN	BRTZ	59.30	1.72	14.50	16.21	7.45	1.70	5.12	1.25	6.81
SGS	WED2	86.52	3.93	0	3.93	3.72	0.01	5.16	0	0.60
QEMSCAN	WED2	69.10	4.05	0.22	4.26	17.15	0.33	5.80	0.85	1.57

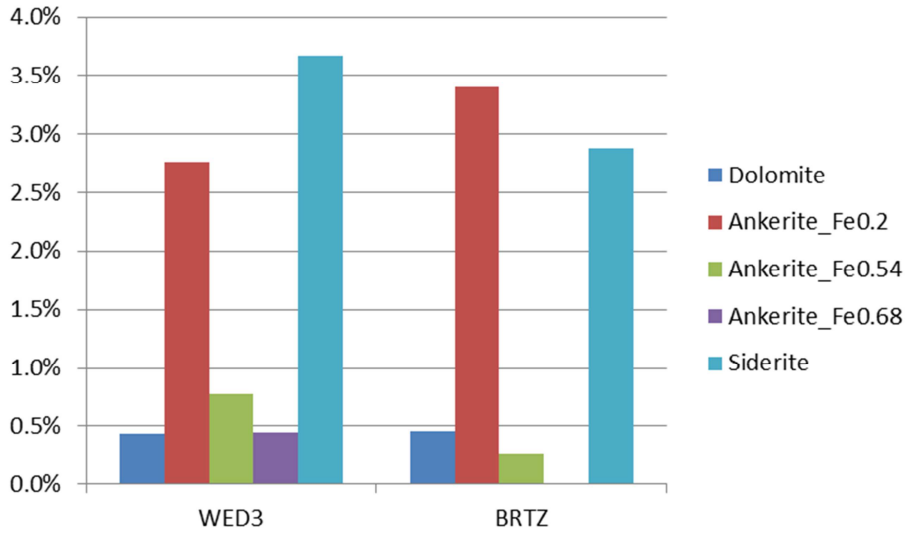

Figure 11. Average carbonate content (mol%) for the samples from WED3 (n=7) and BRTZ (n=5) measured by Qmineral.

6.3.2 Petrographic analysis

QEMSCAN images provide a good impression of the rock textures, which can vary significantly on the macro scale (Appendix D). Detrital grains are highly irregular in shape with sizes from several tens to hundreds of microns in diameter. The texture (layered or patchy), as well as the mineral type (e.g. carbonates, sulfates) of the pore filling cements is visible in QEMSCAN images. Some samples are highly cemented while others are hardly cemented and often show oversized pores. The WED3 samples at a depth greater than 2833 m show more intense cementation than those at shallower depth (Appendix D), which is consistent with the lower porosity and permeability values (see section 6.2; Figure 9).
Light microscopy and SEM analyses are performed to differentiate between primary and secondary minerals, to investigate mineral relations and finally to define a paragenetic sequence. For each field the detrital mineralogy (primary mineralogy which was deposited before onset of diagenesis) consists of quartz, K-feldspar, albite, micas (mainly muscovite, occasionally biotite), heavy minerals (zircon, monazite and apatite) and different kinds of rock fragments like metamorphic clasts and clay-rich clasts (mud clasts).
In the following sections the microscopic observations and mineral relations for each field will be presented, discussed and finally compared among each other.

6.3.2.1 WED3

Oil occurrence

Light microscopy of the thin sections shows the presence of small amounts of oil. Unfortunately, the samples were cleaned prior to thin section preparation and hence, if present, the larger part of the oil has been removed. Relicts of oil have been observed in the rock samples (Figure 8D) and in one sample thin section (WED3.2.1) within most pores. In the petrological analysis performed for the NAM after coring, only small amounts of residual hydrocarbons (dead oil) have been observed within small pores (Pestman, 1991).

Detrital mineralogy

Quartz is the most abundant detrital component. The grains have irregular shapes and show undulose extinction in cross polarized light using light microscopy. Most of the detrital feldspar is K-feldspar, whereas albite (pure Na-feldspar) is rare and/or difficult to distinguish from completely albitized K-feldspar. K-feldspar grains experienced an intensive alteration process during burial: (1) albitization of the detrital grains whereby K is substituted by Na and/or (2) dissolution processes varying from partial dissolution at the rims or along the cleavage planes (Figure 12), to the formation of oversized pores (total dissolution of the grain). Clay-rich rock fragments, from now on referred to as mud clasts, consisting of fine grained clay material of illitic composition, pieces of K-feldspar and quartz and dolomite cement, are abundant. They are often squeezed between mechanically more stable detrital grains (Figure 12). Volcanic rock fragments consisting of fine, intergrown quartz, feldspar, illite/sericite and/or muscovite occur as rounded grains within the samples (Figure 12). Detrital clay is not observed, but is often difficult to discriminate from authigenic clay. Some clays around detrital grains might indicate early, mechanically infiltrated clay coatings, probably smectite. Micas are dominantly muscovite, whereas biotite is rare. Large, detrital muscovite flakes are often squeezed between, or wrapped around, detrital grains. Most muscovite flakes are generally unaltered.
Minor (heavy) minerals include monazites (XPO_4, where X can be any rare earth element), zircons ($ZrSiO_4$) and apatite ($Ca_5(PO_4)_3$) minerals.

Authigenic mineralogy and relative timing

Quartz and K-feldspar

Authigenic quartz is abundant in all WED3 samples investigated in this study. The main type is a syntaxial quartz overgrowth, giving the detrital grains a euhedral shape (Figure 13A). Cathodoluminescence (CL) imaging shows that secondary quartz has grown in different phases, and within open pores zoned, authigenic euhedral quartz crystals can be observed (Figure 14). Pure K-feldspar overgrowth on detrital grains is observed by SEM BSE (Figure 13 B) and CL-imaging (Figure 14). Prior to the formation of authigenic K-feldspar partial albitization (exchange of K by Na) of the grains has taken place. The relative timing of the onset of K-feldspar dissolution is not clear, but occurred at least after K-feldspar overgrowth precipitation.

Early diagenetic carbonates

Dolomite either occurs as pore-filling aggregates within a fine grained illite matrix (most probably residual mud clasts) (Figure 13C), or as large, single crystals within open pores (Figure 13D and 18H). SEM EDX analysis indicates that dolomite zonation (visible by the different grey scales) is caused by varying Fe-contents. The crystals have an Fe-poor core and subsequent zones with higher, but varying Fe concentrations. Occasionally, up to six growth zones can be distinguished (Figure 13D). This is consistent with the XRD results from Qmineral showing varying Fe contents in ankerite minerals (**Error! Reference source not found.**). Dolomite replaces, but is also enclosed by the syntaxial quartz overgrowth. The presence of dolomite and ankerite in between detrital grains suggest an early precipitation. The outer zones of large single dolomite crystals (ankerite rims) have occasionally grown within secondary pore space after K-feldspar dissolution. This implies that ankerite precipitation continues after (the onset of) K-feldspar dissolution.

Clay minerals

Illite mainly occurs in mud clasts (Figure 12) and sporadically as an alteration product of K-feldspar grains (Figure 13E). It is often difficult to distinguish between altered mud clasts and detrital grains which have been replaced by authigenic clay minerals.

Alumino-phosphate-sulphate minerals (APS)

Typical are the small (a few microns) but frequent, euhedral alumino–phosfate-sulfate (APS) minerals which occur frequently as separate mineral grains (Figure 13 H) or as mineral aggregates (Figure 13F). APS minerals have the general formula $AB_3(XO_4)_2(OH)_6$, where A can be occupied by Na^+, K^+, Ca^{2+}, Pb^{2+}, Ba^{2+} or Sr^{2+} and where B is generally occupied by Al^{3+} and XO_4 by SO_4^{2-} or PO_4^{3-} (Spötl, 1990). The APS minerals in WED3 can be classified as a solid solution between the end members goyazite ($SrAl_3(PO_4)_2(OH)_5 \cdot H_2O$), crandallite ($CaAl_3(PO_4)_2(OH)_5 \cdot H_2O$) and alunite ($KAl_3(SO_4)_2(OH)_6$) (Figure 15). In the samples investigated A sites are mainly occupied by Sr and XO_4 sites mainly by PO_4^{3-}. The composition is closest to goyazite, but some PO_4^{3-} is exchanged by SO_4^{2-}, moving towards svanbergite ($SrAl_3(SO_4)(PO_4)(OH)_6$). Furthermore Sr is partially substituted by varying amounts of Ce, La, Ca, K, Na and Mg (up to 40%). The crystals show compositional zoning: The cores of the crystals, having an anhedral shape, are enriched in light rare earth elements (LREE) with 30-40% of the A sites occupied by La and Ce and 35-50% occupied by Sr and 3-4% by K. In contrast, the rims contain less LREE with 5-10% of the A sites occupied by La and Ce, but more Sr (60-65% of the A sites) and K (~10% of the A sites). and SO_4^{2-}. The APS minerals are up to several tens of µm in diameter and generally occur within illitic mud clasts, occasionally in association with dolomite. One APS mineral is found as an

inclusion in dolomite, suggesting that dolomite and APS minerals precipitated simultaneously within the mud clasts.

Ti-oxides

Ti-oxides occur as anhedral and euhedral crystals of various sizes often within, or intergrown with, mud clasts, muscovite grains and volcanic or metamorphic rock fragments. Ti-oxides are enclosed by quartz overgrowths and anhydrite cement. Unclear is whether they are secondary precipitates or inclusions from rock fragments which were liberated after dissolution of the other components.

Sulfates and sulfides

Pyrite occurs as framboids within mud clasts and open pores, or as subhedral crystals within open pores. Framboids sometimes incorporate illite and APS minerals, and are occasionally enclosed by APS aggregates (Figure 13F).

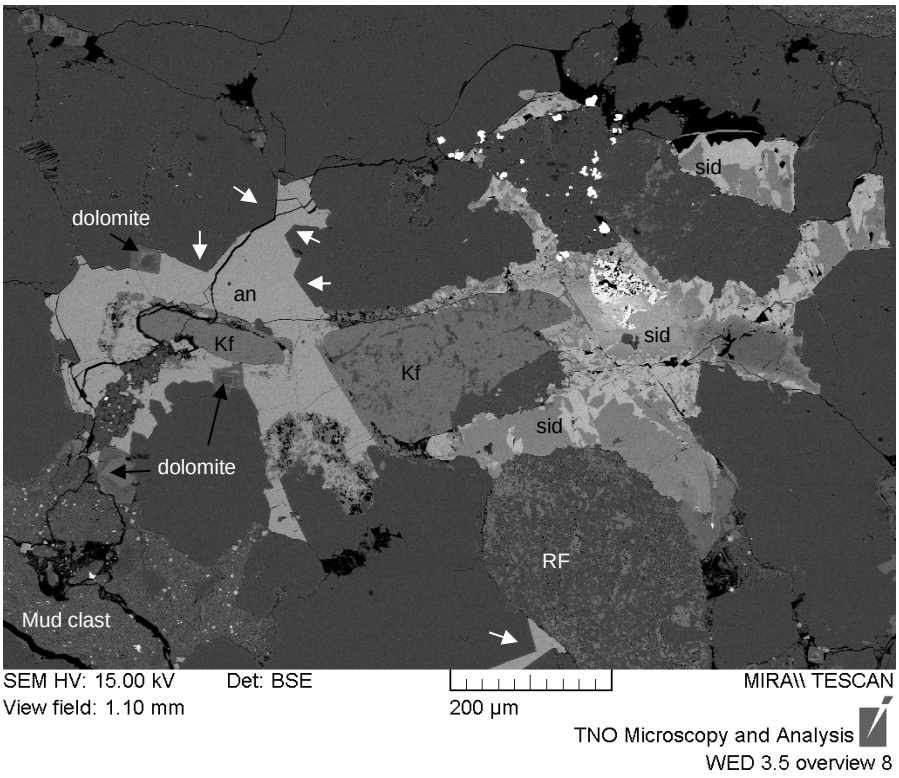

Figure 12. Overview SEM BSE image of WED 3.5 showing detrital quartz and partially albitized K-feldspar (Kf) grains, and a metamorphic or volcanic rock fragment (RF). Anhydrite (an) cement encloses a partially dissolved K-feldspar grain, secondary quartz overgrowths (white arrows) and small, zoned dolomite crystals. The cemented pore space is oversized. Siderite (sid) pore filling cement replaces detrital grains and has a spotted appearance with light and darker zones. The large mass of clay in the lower left corner is a mud clast which is squeezed between the detrital grains. The small white minerals in the middle to upper right are pyrite.

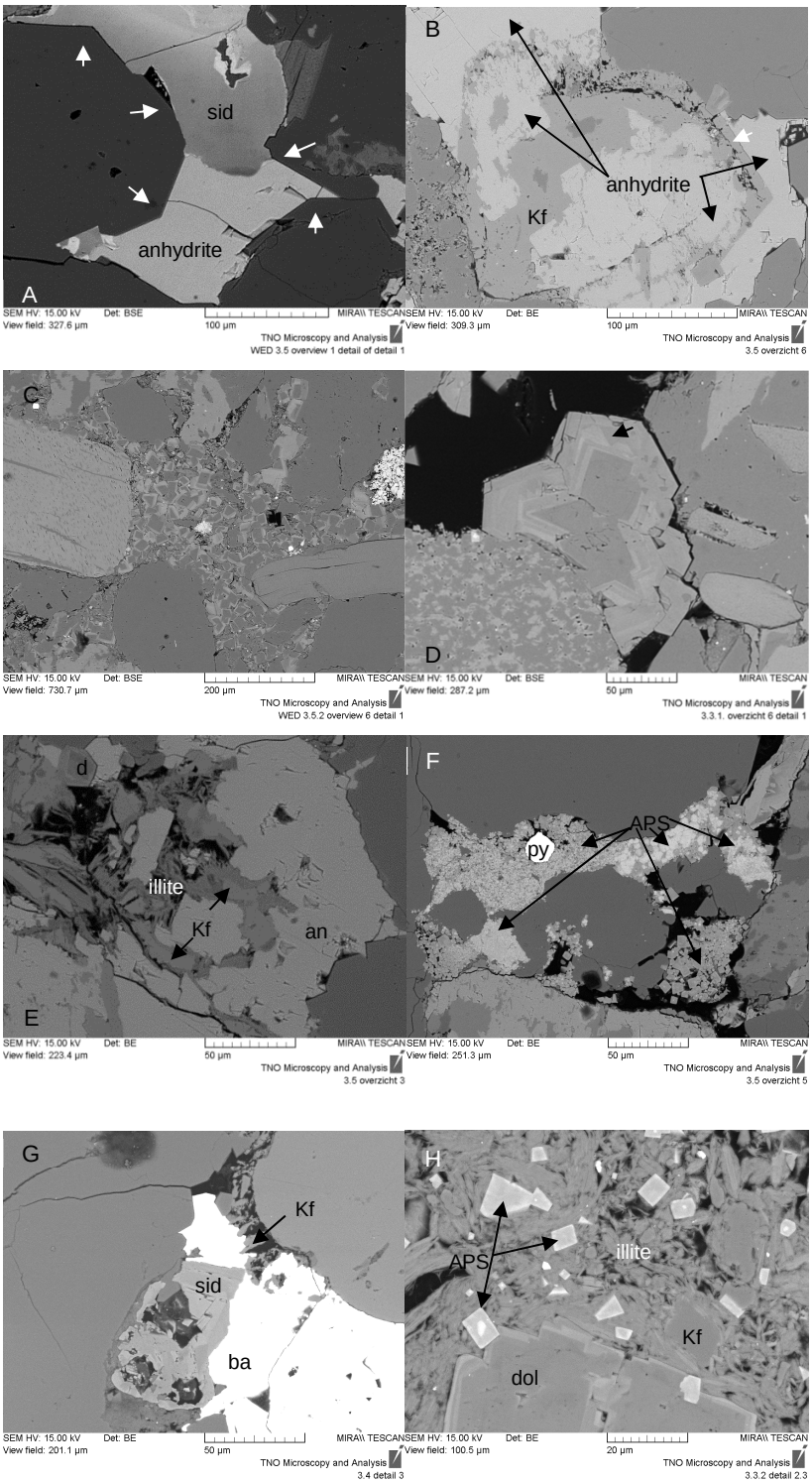

Figure 13 (previous page). SEM BSE images of WED3 samples. A: Quartz overgrowth (white arrows) surrounded by anhydrite and siderite cement. B: K-feldspar with overgrowth (white arrow), partially dissolved and filled with anhydrite cement. C: Zoned dolomites forming pore filling aggregates. D: Large dolomite grain, in between metamorphic rock fragments, showing at least six growth zones and a dissolution phase (black arrow). E: K-feldspar partially altered to illite, and zoned dolomite (d), enclosed by anhydrite cement. F: Pore filling and grain replacement by APS minerals enclosing pyrite (Py). G: Barite cement enclosing K-feldspar remains and siderite cement. H: Euhedral APS minerals within a mud clast in contact with a dolomite crystal.

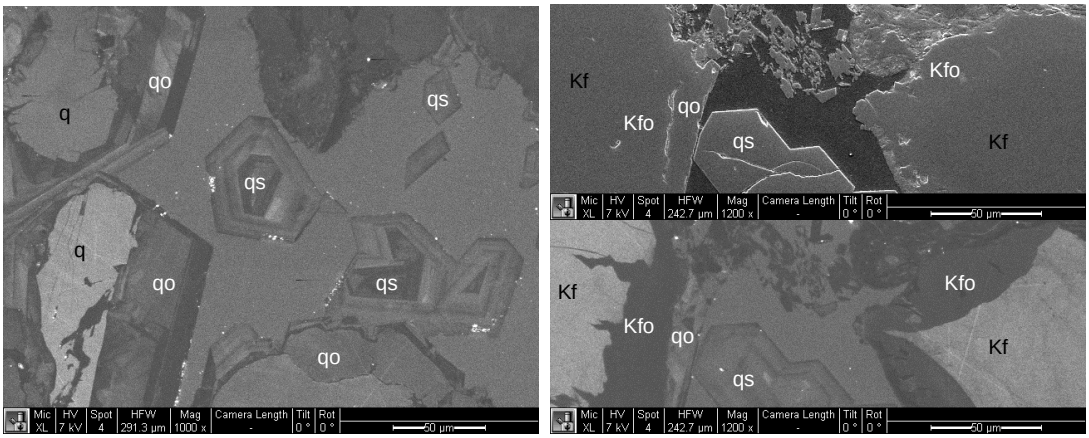

Figure 14. Left: Grayscale CL-image of detrital quartz (q), quartz overgrowth (qo) and euhedral secondary quartz grains (qs). Right: SEM SE image (upper) and corresponding grayscale CL-image (lower) showing euhedral secondary quartz (qs) and K-feldspar detrital grains (Kf) with K-feldspar overgrowth (Kfo) covered by quartz overgrowth (qo).

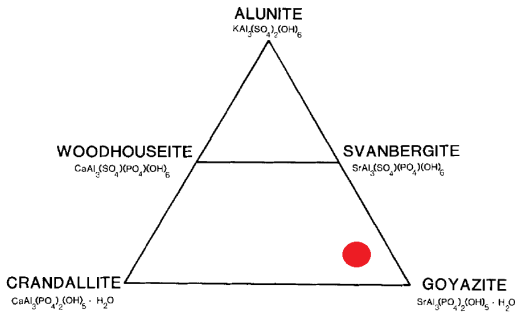

Figure 15. Ternary plot showing the composition of APS minerals in WED3 and WED2. Modified after Spötl (1990).

Anhydrite occurs as isolated, but generally large (few hundreds of microns) patches (or nodules), filling up (oversized) pore space between detrital grains. However, the blocky poikilitic anhydrite cementation is only present in the samples at a depth below ~2833 m AH. Higher up in the reservoir, anhydrite is absent, as also indicated by the XRD results. Where present, it commonly encloses the partially dissolved framework K-feldspars and fills the inter- and intragranular pore space. Anhydrite also encloses, and therefore post-dates, the main quartz overgrowth, pyrite crystals, zoned dolomite/ankerite crystals and illite after K-

feldspar (Figure 13B, E and Figure 17), from which we can conclude that anhydrite is a relatively late phase.
The anhydrite cement is locally (partially) dissolved and replaced by siderite. Charged contrast imaging showed dark spots within the anhydrite cement, which possibly represent hydrated anhydrite as a pre-stage for dissolution (Figure 17).
Barite cement occurs very local, but can be observed in all samples. It encloses dolomite, pyrite, Ti-oxides and siderite cement (Figure 13I). It is probably the latest authigenic phase.

Late diagenetic carbonates

A late Mg-rich siderite cementation event is abundant in most samples, filling up residual pore space and replacing detrital and authigenic minerals. In the samples that contain anhydrite, siderite precipitated after anhydrite dissolution, thereby enclosing the anhydrite remains (Figure 16). The siderite cement is patchy in color in SEM BSE imaging, with varying grey shades. EDX analyses show varying magnesium contents of the patchy zones. This is also visualized in EDX element maps (Figure 16). Often, the lighter and darker zones of the siderite (as indicated by SEM analysis) have a very abrupt interface (Figure 12), while occasionally the interface is much more gradual (Figure 13A). The more pure siderite with low Mg content is often present at the outer part of the pore filling cements. The range in Mg and Fe content of siderite is large. SEM EDX analyses and element maps indicate varying Mg concentrations (from 2 to 10 mol %) (Figure 16). The results are plotted in a ternary plot in Figure 21, which also includes the results for dolomite.

Oil occurence

Some oil is observed in contact with quartz overgrowth and adjacent to, but not infiltrating, a K-feldspar skeleton, suggesting oil charging after quartz overgrowth (or at least the onset of quartz overgrowth), but prior to (the end of) K-feldspar dissolution. This particular sample contains a large amount of the late stage siderite cement.

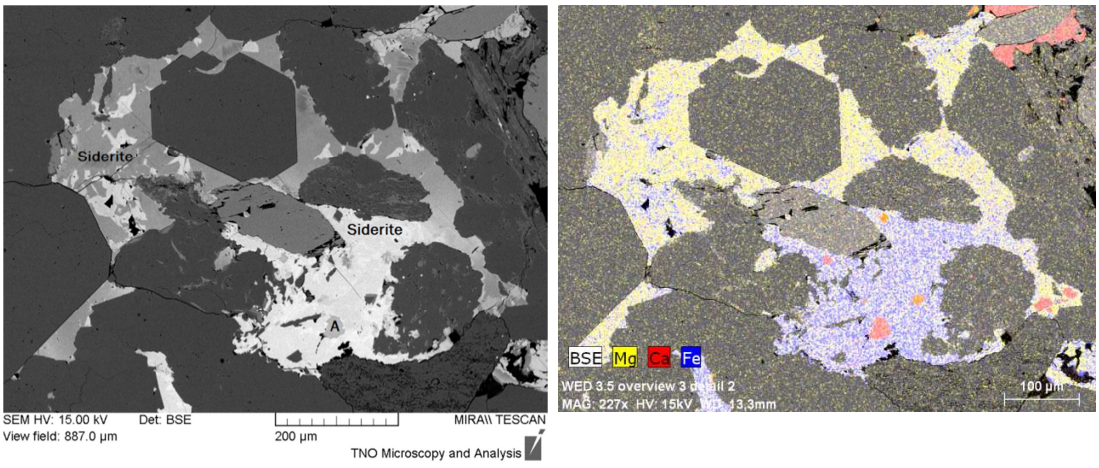

Figure 16. SEM BSE image (left) and corresponding element map (right), showing siderite cement with varying Mg content, enclosing anhydrite (A) remnants (Ca-rich spots within siderite, visible in the element map), quartz overgrowth, partially leached K-feldspar and several rock fragments.

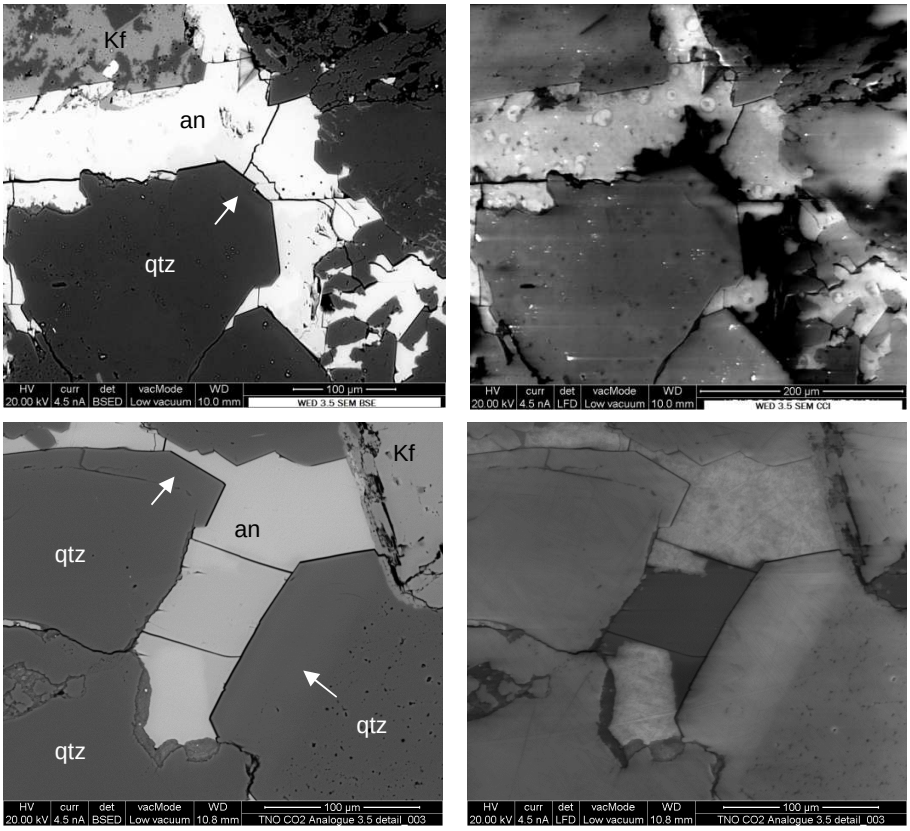

Figure 17. SEM BSE images of anhydrite cement (an) enclosing partially dissolved and albitized K-feldspar (Kf) and quartz overgrowth (white arrows)(upper and lower left) and corresponding Charge Contrast Images (CCI) (upper and lower right). The CCI images show some dark spots within the anhydrite, possibly showing mineral hydration as a preliminary stage for dissolution.

6.3.2.2 BRTZ

Detrital mineralogy

The detrital mineralogy of BRTZ is similar to WED3. The dominant detrital mineral within the sandstones is quartz. The detrital quartz grains have a rounded or elongated shape. Grains can show undulose extinction in crossed polarized light. The quartz is probably magmatic as well as metamorphic in origin. K-feldspar is the most common type of feldspar while (detrital) albite is rare, as was also shown by the XRD analyses (Table 10). The K-feldspar grains often contain fractures. Most feldspars show dissolution along cleavage planes and/or have corroded rims, but dissolution is not as extensive as in WED3. Few grains experienced major dissolution leaving only a framework structure, but many are partially replaced by clay minerals (mainly kaolinite).

The dominant micas are muscovite and biotite, whereas biotite is absent in WED3. Detrital mica is often deformed or squeezed between K-feldspar or quartz grains. Biotite and occasionally muscovite are partially replaced by authigenic minerals.

Heavy minerals occur as single grains or as inclusions within detrital quartz and feldspar grains. The dominant heavy minerals are zircon and monazite. Apatite is more common here than in WED3, although both contain <1% apatite.
The main rock fragments are mud clasts, having an illite/smectite content with low K (<1.5 wt%), Mg (<0.5 wt%) and Fe (<1.0 wt%) content. Those clasts are often squeezed between the detrital grains. Fine grained volcanic rock fragments are also present. These clasts have a sub-rounded shape and consist of intergrown K-feldspar, quartz and muscovite crystals.

Authigenic mineralogy
The mineral relations observed in the samples show a complex paragenetic sequence which could only be partially unraveled.

Quartz and K-feldspar
Most of the K-feldspar grains are partially albitized, generally with a preferred orientation along the cleavage planes. The albitized zones terminate against K-feldspar overgrowth (Figure 18A), implying albitization before overgrowth precipitation. Mechanical compaction resulted in fractures within detrital grains, mainly in K-feldspar (Figure 18A and B). They run through albitized zones and overgrowth (Figure 18A) and are therefore post albitization and overgrowth formation. K-feldspar dissolution and alteration post-date K-feldspar overgrowth ((Figure 18A, B and D).
Syntaxial quartz overgrowth is observed in the samples (Figure 18E and F) but is not as abundant as in WED3. The quartz overgrowth is generally euhedral in shape and shows signs of zoning in CL imaging.

Clay minerals
Kaolinite is the main clay mineral present within the samples, apart from (primary) illite in clay clasts. Vermicular type of kaolinite occurs either as an alteration product of K-feldspar (Figure 18D) and mica (mainly biotite, occasionally muscovite)(Figure 18B), or within the intergranular pore space. The kaolinite in primary pores is present as booklets. Occasionally, the larger booklets show alternating crystals of kaolinite and either illite or biotite. The illite/biotite layers are rich in K with significant amounts of Mg and Fe. These features can be interpreted as either biotite alteration to kaolinite, or illitization of kaolinite. Hence, the kaolinite is either the result of biotite alteration or is a product of K-feldspar leaching. The relative timing of mica and K-feldspar alteration to kaolinite is not clear. K-feldspar alteration to kaolinite occurred at least after K-feldspar overgrowth.

Early diagenetic carbonates
Zoned dolomites are abundant. Compared to WED3 they are smaller and contain only two, maximally three growth zones. They were interpreted to be early diagenetic, with Fe-rich dolomite precipitation continued after the formation of kaolinite.
In total 5 different types of siderite (sid 1 – 5) have been recognized based on their morphologies and association. When kaolinite is replacing biotite, it is often associated with anhedral, granular siderite crystals (sid 1)(Figure 18A and B). Siderite with the same morphology is also frequent within clay clasts (sid 2). Occasionally it is observed to enclose K-feldspar overgrowth implying precipitation post K-feldspar. The zoned dolomites are most often surrounded by small patches of siderite (sid 3) (Figure 18C). Also larger, pore-filling siderite cement (sid 4) can be observed which replaces earlier authigenic quartz (Figure 18E). In addition, euhedral siderite grains (sid 5), forming aggregates are observed which have grown adjacent to, or replaced quartz overgrowth (Figure 18F).

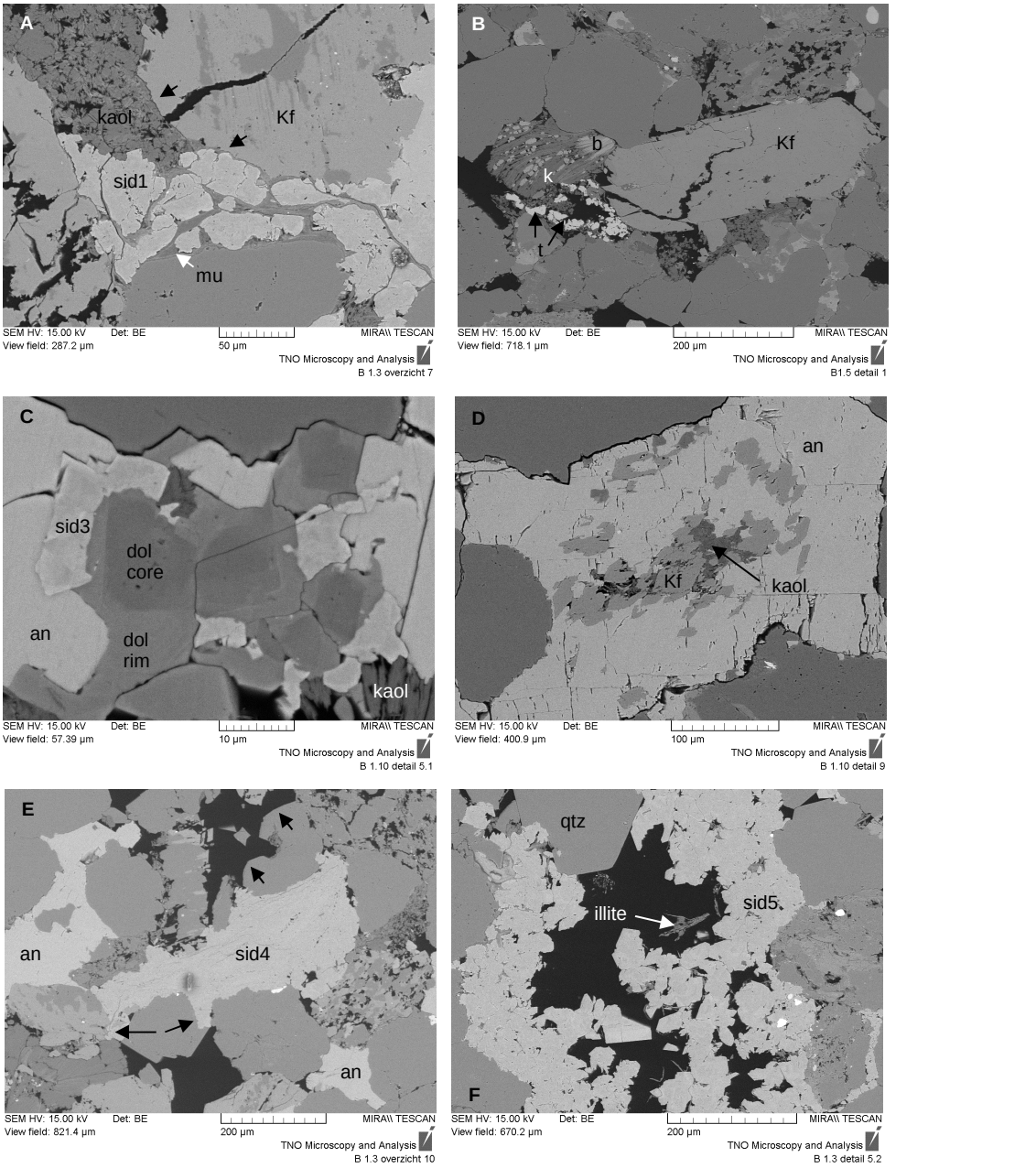

Figure 18. SEM BSE images of BRTZ samples. A: Partially albitized K-feldspar grain. The albitized zones terminate against K-feldspar overgrowth (black arrows). A fracture runs right through the grain, including the overgrowth. Almost complete replacement of muscovite (mu) by (partially intergrown) kaolinite and siderite (sid 1). B: Fractured K-feldspar grain with overgrowth. Biotite flake (b) replaced by kaolinite (k) and anhedral siderite nodules (sid 1). Right below, kaolinite with authigenic Ti-oxide (t). C: Zoned dolomites (dol), surrounded by siderite (sid 3) and anhydrite (an). D: K-feldspar (Kf) alteration to kaolinite (kaol), secondary pore space cemented by anhydrite. E: Pore-filling anhydrite (an) and siderite cement (sid 4). Siderite replaces quartz overgrowth (black arrows). F: Euhedral siderite aggregate (sid 5) intergrown with fibrous illite, growing adjacent to, or replacing quartz overgrowth.

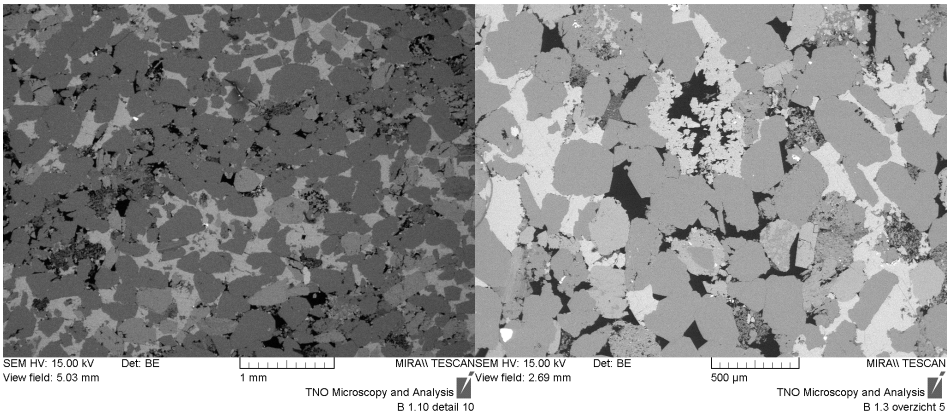

Figure 19. SEM BSE overview photos showing anhydrite cementation of oversized pore space.

The relative timing of the different siderites is not straightforward. Siderite 1 and 2 are post K-feldspar overgrowth, but any further restriction to timing cannot be made since the siderite is always present within respectively the altered micas or clay clasts. Siderite 3 is post dolomite and prior to anhydrite. Siderite 4 and 5 are post quartz overgrowth.

Ti-oxides

Ti-oxides are occasionally associated with biotite alteration. The Ti-oxide minerals are <15 µm in size, have an euhedral or anhedral shape and are common in all samples. They often form together with kaolinite in open pore space and occasionally with siderite. The Ti-oxides are enclosed by quartz overgrowth and are therefore prior to authigenic quartz. They seem to have precipitated simultaneously with kaolinite from biotite and/or K-feldspar alteration.

Sulfates and sulfides

Early formed pyrite crystals locally occur in most samples and have a euhedral shape. The size of the crystals vary from 1 – 100 µm.
The most common and extensive cement is anhydrite, which is present in most of the samples. It forms large patches of blocky, poikilitic, pore-filling cement.
It encloses intragranular kaolinite within residual K-feldspar grains (Figure 18D), indicating K-feldspar alteration to kaolinite prior to anhydrite cementation. Anhydrite also encloses siderite (sid 3), which in turn encloses dolomite (Figure 18C), allowing the following sequence to be deduced: zoned dolomite, siderite (sid 3) and anhydrite. Anhydrite is one of the latest phases. The areas within the sample that are highly cemented with anhydrite or siderite do not show major quartz overgrowth. The areas without cementation clearly show more syntaxial quartz overgrowth. This suggests that some quartz precipitation occurred after cementation.
Furthermore, anhydrite fills large pores, suggesting a major dissolution event which occurred prior to or during cementation (Figure 19). This dissolution event could be related to continued K-feldspar leaching, with or without kaolinite precipitation, but could also be linked to an early framework cement.

Alumino-phosphate-sulphate minerals (APS)

Small APS minerals (<1 µm) are present within the illitic clay clasts. The exact mineral composition is unknown, since the small grains size does not allow exact EDX-analysis.

6.3.2.3 WED2

Detrital mineralogy

For WED2 three samples were analysed. The detrital mineralogy of WED2 is similar to WED3 and BRTZ and consists mainly of quartz, K-feldspar and micas (mainly muscovite, rarely biotite flakes). Dolomitic mud clasts consist mainly of illite, muscovite, zoned dolomite, Ti-oxides (anatase?) and apatite. They also contain APS minerals, which are probably authigenic. These mud clasts are squeezed between the detrital grains, forming a pseudomatrix. Unclear is whether the zoned dolomites are part of the mudclasts or if they replaced them. Lithoclasts (fine grained metamorphic clasts) are very common. The rounded, fine grained metamorphic clasts consist of quartz or albite with muscovite/illite and occasionally Ti-oxide (rutile or anatase) and apatite. These clasts are more rigid than the mud clasts. Much mechanical compaction occurred, during which the detrital grains, mud clasts and lithoclasts are compressed, resulting in rugged grain contacts between them (Figure 20 A).

Authigenic mineralogy

Quartz and K-feldspar

K-feldspar grains are heavily dissolved and often only skeletons of the grains remain. Occasionally, the K-feldspar re-precipitated as small crystals of subhedral albite. Syntaxial quartz overgrowth is common (Figure 20 B).

Clay minerals

K-feldspar grains were occasionally altered to kaolinite or illite. Occasionally, kaolinite is observed adjacent to, or intergrown with illite. Aggregates of illite and kaolinite are observed with the shape of the original feldspar grain. Remaining pieces of K-feldspar do not show signs of albitization. Kaolinite booklets are also present in intergranular pore space.

Early diagenetic carbonates

Zoned dolomites are large (up to 200 µm) and abundant (up to 22 wt%, see Table 10) and occur as large single crystals adjacent to quartz grains (Figure 20 B) or as aggregates of intergrown, euhedral minerals (Figure 20 C). The zoned dolomite minerals appear to be an early phase. They are present in between the detrital grains, suggesting that they have precipitated prior to major mechanical compaction.
The ankerite rims of zoned dolomite crystals seem to have formed simultaneously with major quartz overgrowth (Figure 20 B and C). Ankerite (without Fe-poor core) is observed in secondary pore space after K-feldspar alteration to illite.

Sulfates and sulfides

Anhydrite is the most common cement. It encloses zoned dolomites and early quartz overgrowth. Often, anhydrite precipitated within the illite clay after K-feldspar alteration (Figure 20 D). Barite cement is common and seems to be a late phase cement, after K-feldspar alteration to clay and quartz overgrowth (Figure 20 E).

Alumino-phosphate-sulphate minerals (APS)

APS minerals are abundant, sometimes in large aggregates associated with illite (Figure 20 F). They have a chemical composition in between svanbergite ($SrAl_3(SO_4)(PO_4)(OH)_6$) and woodhouseite ($CaAl_3(SO_4)(PO_4)(OH)_6$) similar to those in WED3 (Figure 15).

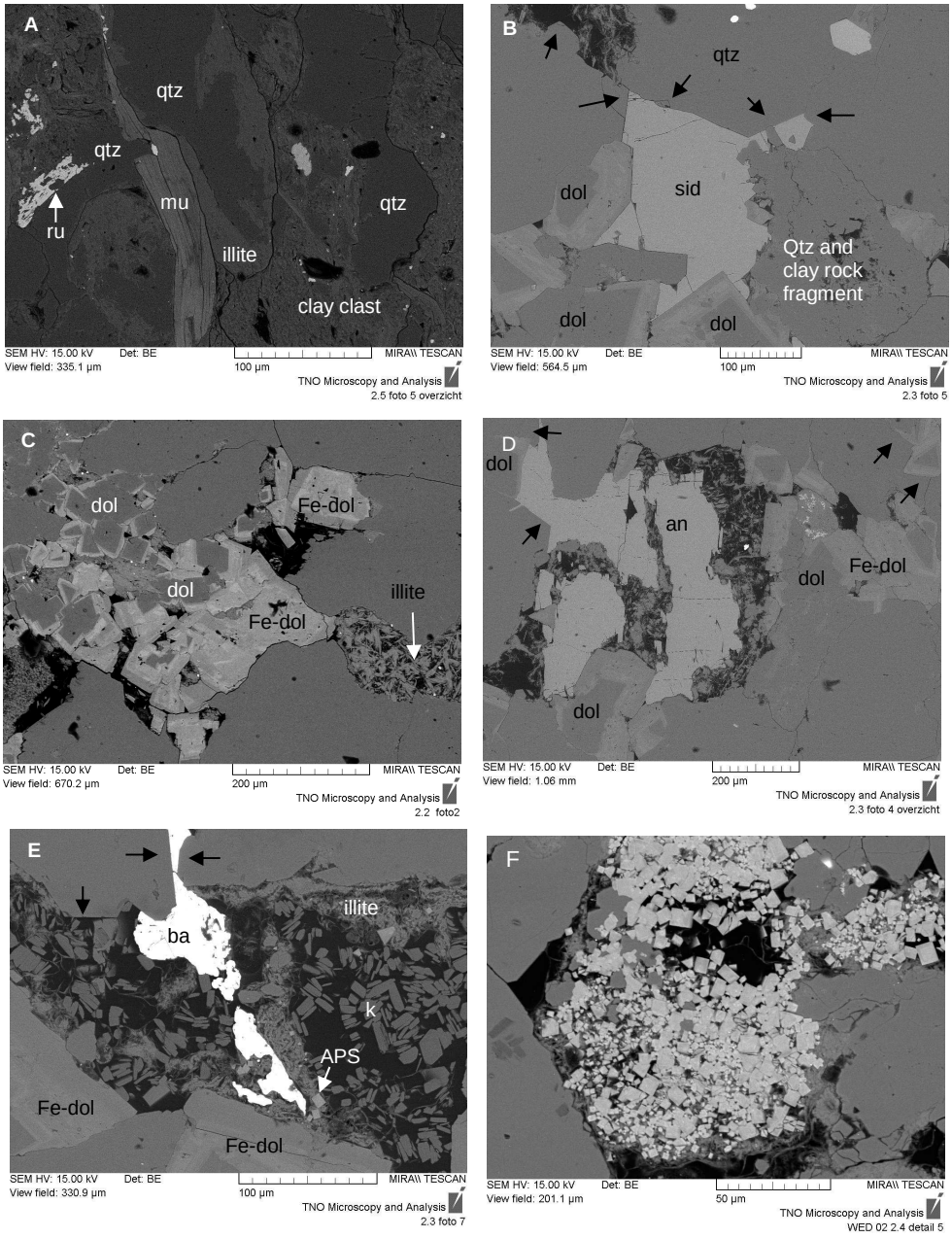

Figure 20. A: Detrital minerals, clay clasts and rock fragments are compressed during compaction. B: Quartz grains with syntaxial quartz overgrowth (black arrows). Large, zoned dolomite minerals as well as syntaxial quartz overgrowth are enclosed by pore filling siderite. C: Aggregate of zoned dolomites. Illite fibres seem to have replaced a K-feldspar detrital grain. D: Large, zoned dolomites, adjacent to quartz overgrowth (black arrows). In the top left corner, quartz overgrowth encloses the Fe-dolomite rim. Feldspar altered to illite, potentially signs of kaolinite precursors present. Secondary pore space filled by anhydrite cement, which surrounds the zoned dolomite and quartz overgrowth. E: Illite clay adjacent to quartz overgrowth and zoned dolomites. Kaolinite booklets (k) in open pore. Barite (ba) cement encloses quartz overgrowth (black arrows), illite and kaolinite. Few APS minerals are present within the illite clay. F: aggregate of APS minerals intergrown with illite and authigenic albite.

6.3.2.4 Comparison of the fields

The different fields show similar, but also deviating mineral relations, as described in the previous sections. The main differences will be described in this section.

Quartz and K-feldspar

K-feldspar dissolution is much more extensive in the WED2 aquifer than in the WED3 CO_2-field and BRTZ CH_4-field, and much authigenic albite or albitized remains after K-feldspar dissolution is present. Authigenic syntaxial quartz overgrowth is much more extensive in WED3 and WED2 than in BRTZ.

Clay minerals

Kaolinite is a very common clay mineral in all samples from BRTZ. In BRTZ both detrital K-feldspar and biotite altered to kaolinite. In sample from WED2, but especially in those from WED3, detrital biotite and authigenic kaolinite are rare or absent. In these samples most of the reaction products from K-feldspar dissolution have been transported out of the sandstones since authigenic clay as an alteration product is rare. Occasionally, illite is observed as a reaction product of K-feldspar alteration. In BRTZ illite is mainly present in clay clasts.

Sulfates

Anhydrite cement is present in the three fields but is most extensive in BRTZ. In the samples from WED2, anhydrite often grew in between illite clay, which was not observed in the other fields. In WED3 anhydrite is only present in the lower part of the Röt Fringe Sandstone Member. It is partially dissolved and replaced by siderite. In WED3 anhydrite cementation occurred well after the major quartz overgrowth phase and major compaction. In BRTZ anhydrite cementation occurred, before major quartz cementation.

Carbonates

Siderite in BRTZ has a very different occurrence than in WED3 and a different timing. In BRTZ five different morphologies were recognized, interpreted to have potentially precipitated in several phases. These phases are probably all prior to anhydrite cementation. In WED3 more siderite is present, but only one type of morphology is observed. Furthermore, this siderite precipitated *after* anhydrite cementation. In WED2, siderite cement is also present but rare. For this field, the relative timing of anhydrite and siderite is not clear since contact between the minerals was not observed and no other indications for relative timing were found.

Figure 21 shows the cation composition of the siderite and dolomite phases in the WED3, BRTZ and WED2 Röt Fringe Sandstones. All dolomites have a narrow range in Ca content between 0.5 and 0.6 and a more variable Mg and Fe content with Fe between 0 and 0.28. Only for BRTZ, the Fe content of the dolomites remains below 0.15. This is consistent with the XRD results from Qmineral (Table 11). The siderite composition is most variable for WED3, with Mg contents between 0.15 and 0.57 and very low Ca contents.

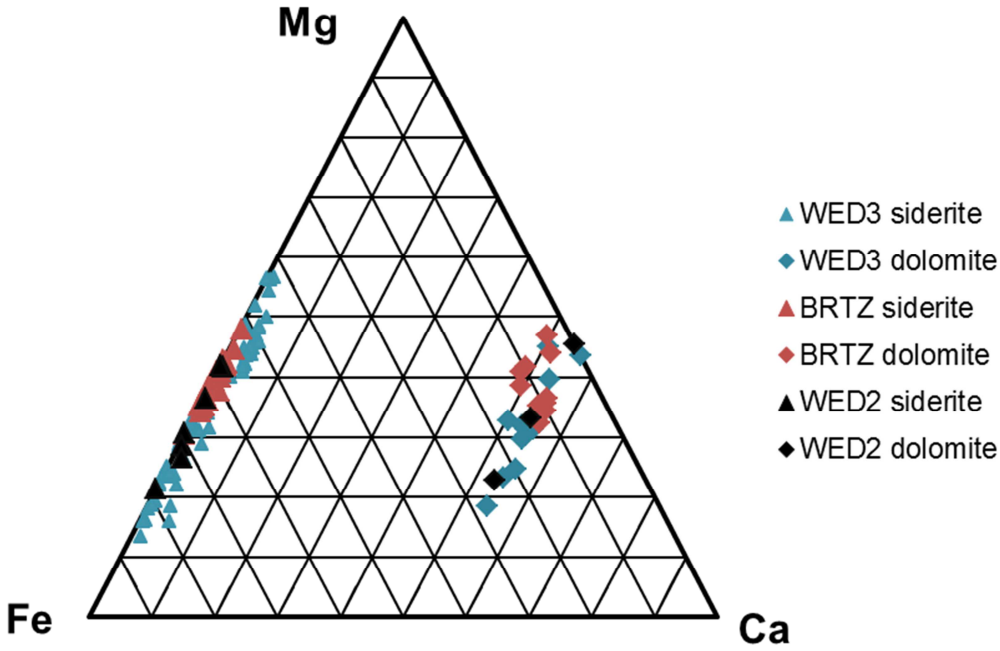

Figure 21. Ternary plots showing the Fe, Mg and Ca content for WED3, WED2 and BRTZ siderite and dolomite.

7 Isotope analysis

Carbon and oxygen isotope analysis is performed on bulk carbonates for selected samples. The procedure for the analysis is based on the methodology as described by McCrea (1950). For each sample 500 mg of the submitted powdered samples was loaded into sample reaction tubes and placed in a reaction vessel containing 4 ml of anhydrous phosphoric acid. Then, the vessels were evacuated to > 1.0^{-4} mb to remove atmospheric carbon dioxide and moisture. The reaction vessels were sealed and placed in a controlled temperature water bath at 100^{o}C and allowed to thermally equilibrate for approximately 30 minutes. Reaction occurs by introducing the acid into sample tubes within the sealed, evacuated vessel. The vessels were intermittently agitated and then left for 4 days to ensure reaction has gone to completion.
The resultant gas is cleaned up cryogenically by expanding it through an acetone cold trap maintained at >-90^{0}C and collected in clean dry collection vessels using liquid nitrogen. The vessels were sealed and transferred to the VG Optima - a duel inlet gas source mass spectrometer - for analysis.
Each batch of unknown samples is run with 3 primary standards with known values with respect to NBS-19 (VPDB) and a duplicate.
The resultant gas values are further corrected using Craig's correction to adjust for small levels of ^{17}O isotopes, normalised through the primary standard and corrected to the solid carbonate value using a fractionation factor to account for the incomplete liberation of the oxygen in phosphoric acid. For siderites this factor is 1.00881 at 100^{o}C.

Different carbonate minerals react at differing temperatures according to thermal stability. By reacting the samples at 100^{o}C CO_2 from all carbonates present will have been liberated and corrected as for siderite.

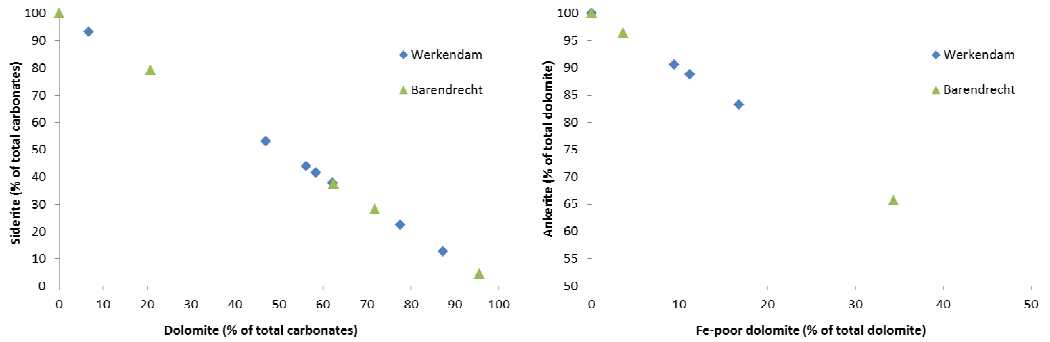

Figure 22. Carbonate content for samples selected for isotope analysis. Left graph: dolomite vs. siderite. Note the wide spread in dolomite/siderite ratio for both fields. Right graph: Fe-poor vs Fe-rich dolomite (ankerite). Note the different axe-scales for Fe-poor and Fe-rich dolomite. The Fe-rich dolomite includes Ankerite_Fe0.2 to Ankerite_Fe0.68 (see Table 11).

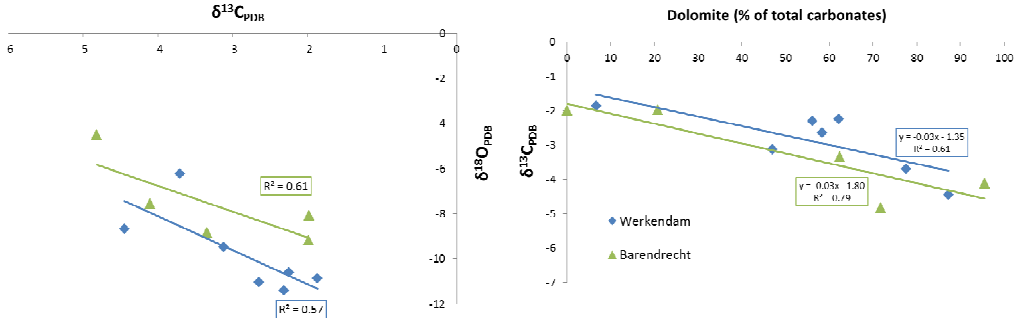

Figure 23. Isotope analysis results. Left graph: Oxygen versus carbon isotope values. Right graph: carbon isotope values as a function of the percentage dolomite (Fe-poor and Fe-rich) of the total carbonate content.

For both WED3 and BRTZ the selected samples have a wide range in dolomite versus siderite content (Figure 22). Most of the dolomite can be classified as ankerite (Fe-rich dolomite). See also the XRD results in Table 11 and in Figure 11.

Figure 23 shows the results of the stable isotope analysis. For both WED3 and BRTZ a negative correlation exists between $\delta^{13}C$ and $\delta^{18}O$ with a R^2 of 0.57 and 0.61 respectively. $\delta^{13}C$ values are -1.9 to -4.4‰ and -2.0 to -4.8‰, and $\delta^{18}O$ values are -6.2 to -11.4‰ and -4.5 to -9.2‰ for WED3 and BRTZ respectively. A negative correlation exists between the amount of dolomite (as a percentage of total carbonate) and $\delta^{13}C$. The linear equations for the fields with R^2 of respectively 0.61 and 0.79 indicate $\delta^{13}C$ values of -1.35‰ and -1.80‰ for WED3 and BRTZ at a dolomite concentration of zero, implying these are the average values for the siderite. The $\delta^{13}C$ values for dolomite is respectively -4.11‰ and -4.68‰. Since the R^2 values are only moderate, the differences in $\delta^{13}C$ values for siderite and dolomite between the two fields cannot be considered to be highly significant. Hence, no conclusions can be drawn for the sources of the siderite in WED3 versus BRTZ.
For WED3, the samples which contain Fe-poor dolomite (WED 3.1, WED3.6.1 and WED 3.6.5) all lie below the regression line, while the ones without Fe-poor dolomite (except for WED 3.2 which has an overall low dolomite content) lie above the line. This might indicate a lower $\delta^{13}C$ value for the Fe-poor dolomites which make up the cores of the grains (as shown by the SEM images in section 6.3.2). The ankerite rims with variable Fe content then have a slightly less negative $\delta^{13}C$ value. Also for BRTZ the higher Fe content of the dolomites seems to increase the $\delta^{13}C$ value.
No significant correlation exists between the carbonate content and $\delta^{18}O$ values.

Table 6. XRD results on carbonate content and whole rock stable isotope results of the carbonate content.

	WED 3.1	WED 3.2	WED 3.3 + 3.3.1	WED 3.4.1	WED 3.5.2	WED 3.6.1	WED 3.6.5	B1.1	B1.3	B1.10	B1.11	B1.13
Dol total	**3.5%**	**0.6%**	**1.5%**	**1.5%**	**3.8%**	**13.5%**	**4.4%**	**8.1%**	**0.0%**	**2.4%**	**5.9%**	**0.3%**
Of which dol	0.4%	0.0%	0.0%	0.0%	0.0%	2.3%	0.4%	0.3%	0.0%	0.0%	2.0%	0.0%
Of which Ankerite_Fe0.2	2.6%	0.3%	1.1%	1.2%	2.5%	8.6%	3.1%	7.4%		2.2%	3.9%	0.1%
Of which Ankerite_Fe0.54	0.6%	0.1%	0.4%	0.4%	1.2%	1.9%	0.9%	0.4%		0.2%		0.2%
Of which Ankerite_Fe0.68		0.2%				0.7%						
Of which ankerite in total	3.1%	0.6%	1.5%	1.5%	3.8%	11.2%	4.0%	7.8%	0.0%	2.4%	3.9%	0.3%
Siderite	**0.5%**	**8.2%**	**1.2%**	**0.9%**	**2.7%**	**3.9%**	**5.0%**	**0.4%**	**1.3%**	**1.5%**	**2.3%**	**1.2%**
Total carbonate	**4.0%**	**8.8%**	**2.6%**	**2.5%**	**6.4%**	**17.4%**	**9.4%**	**8.5%**	**1.3%**	**3.9%**	**8.2%**	**1.5%**
Dol total % of total carbonates	**87.2**	**6.7**	**56.1**	**62.2**	**58.4**	**77.5**	**47.0**	**95.5**	**0.0**	**62.4**	**71.8**	**20.8**
dol% of total dolomite	11.1	0.0	0.0	0.0	0.0	16.7	9.4	3.6	0.0	0.0	34.3	0.0
dol % of total carbonates	9.7	0.0	0.0	0.0	0.0	13.0	4.4	3.4	0.0	0.0	24.7	0.0
Fe-dol % of total dolomite	88.9	100.0	100.0	100.0	100.0	83.3	90.6	96.4	0.0	100.0	65.7	100.0
Fe-dol % of total carbonates	77.5	6.7	56.1	62.2	58.4	64.6	42.6	92.1	0.0	62.4	47.1	20.8
Sid % of total carbonates	**12.8**	**93.3**	**43.9**	**37.8**	**41.6**	**22.5**	**53.0**	**4.5**	**100.0**	**37.6**	**28.2**	**79.2**
$\delta^{13}C_{PDB}$ (‰) of carbonates	-4.4	-1.9	-2.3	-2.2	-2.6	-3.7	-3.1	-4.1	-2.0	-3.3	-4.8	-2.0
$\delta^{18}O_{PDB}$ (‰) of carbonates	-8.7	-10.8	-11.4	-10.6	-11.0	-6.2	-9.5	-7.5	-9.2	-8.8	-4.5	-8.1

8 Diagenetic history

The observed mineral relations as described in the previous chapter are integrated with the results from the XRD analyses, the temperature evolutions from basin modelling (only for WED3 (Röt Fringe Sandstone Member only) and BRTZ) and literature data on sandstone diagenesis. The latter includes mineral stability fields and typical temperature values for diagenetic processes. The results of this integration for WED3 and BRTZ are shown in Figure 24 and Figure 25 respectively. Exact timing of the mineral reactions is difficult, resulting in uncertainty ranges for the different phases. The results for WED2 are described, since basin modelling was not performed.

8.1 Paragenetic sequence

The dolomite minerals in each of the fields are considered as one of the earliest phases in the paragenetic sequence. They are zoned, having a Fe-poor core and several zones with higher, but varying iron contents (Fe-rich dolomite or ankerite rims). Fe-poor dolomite is generally related to early diagenetic processes under oxic conditions when iron is bound in Fe-oxyhydroxides and/or Fe-oxides, indicating precipitation prior to pyrite which requires reducing conditions. The carbon for early diagenetic carbonates is often supplied by thermal decay of organic matter in the soil and from atmospheric CO_2 and this process also controls the isotopic ratios within the carbonates (Morad, 1998, Irwin et al. 1977 and Curtis 1978, in Lu et al. 2011). The $\delta^{13}C$ values of these type of dolomites are generally between -10‰ and -3‰ (Morad, 1998), which is consistent with the values obtained from the isotope analysis performed for this study (-4.1‰ and -4.7‰ for WED3 and BRTZ respectively). The Fe-rich dolomite/ankerite zones have grown in later stages. The increased Fe content of dolomite zones is generally the result of iron reduction under increasingly reducing conditions, and hence the composition is highly dependent on the amount of initial Fe-oxyhydroxides and/or Fe-oxides in the sandstone and the redox state of the formation water. Iron could also originate from smectite to illite transition. Smectite is not detected by XRD, but the illite of the mud clasts and potentially grain coatings might be the result of a smectite precursor. The dolomites in WED3 and WED2 contain more zones than those in BRTZ, possibly indicating an initially higher content of Fe-oxyhydroxides, Fe-oxides or smectite or availability of carbon. According to Worden and Burley (2003) authigenic ferroan dolomite growth is kinetically favored at similar or somewhat higher temperatures than illite and quartz cements (~100°C).

Pyrite is a common early precipitate in sedimentary rocks (Pettijohn et al., 1987) after conditions change from oxidizing to reducing (or at least locally), with iron-oxides or smectite as a source for iron. We can assume that precipitation was soon after sediment deposition.

Albitization is common in the three fields. XRD and QEMSCAN analyses show that the total feldspar content is similar for WED3 and BRTZ, but the amount of K-feldspar is much higher and the plagioclase (albite) content much lower in BRTZ. This is due to lesser albitization of the K-feldspar in BRTZ, as shown by the petrographic study. The samples of WED 2 contain less feldspar, both K-feldspar and albite, possibly due to the high water content available for dissolution. K-feldspar albitization during burial diagenesis can occur at temperatures >65°C (Saigal et al., 1988 and Worden and Morad, 2000) but becomes pervasive at temperatures >100°C. Potential Na-sources can be North Sea pore waters, supplemented by Na from

Permian (Zechstein) and/or Triassic evaporites, or illitization of smectite (Saigal et al., 1988). Since K-feldspar overgrowth does not show signs of albitization in any of the samples, we concluded that the overgrowth precipitated after albitization.

BRTZ and WED2 contain kaolinite in addition to illite while WED3 contains only illite. In BRTZ the kaolinite is associated with anhedral siderite crystals as replacement for mica, especially biotite and possibly muscovite. Mica alteration results in the formation of kaolinite, K-feldspar, quartz and siderite, a reaction which commences in sandstones at a temperature <50-70˚C (Bjørkum and Gjelsvik, 1988, Morad, 1990). This suggests that the timing of biotite alteration might be simultaneous with timing of K-feldspar and quartz overgrowth. The siderite in the BRTZ samples is rich in Mg, suggesting that, in addition to Fe, the Mg from biotite is incorporated in the siderite. This siderite has a very different morphology than the pore-filling and grain replacing siderite in WED3. The absence of abundant (remnants of) biotite grains in WED3 explains the lack of an early siderite phase in this field.
Authigenic kaolinite in BRTZ also occurs as replacement of K-feldspar. The kaolinite booklets *in open pores* could be the result of feldspar alteration as well. The reaction by which K-feldspar is replaced by kaolinite is (Lanson et al., 1996):

$$2\ \text{K-feldspar} + 2\ H^+ + H_2O \rightarrow \text{kaolinite} + 4\ \text{quartz} + 2\ K^+$$

This reaction is sensitive to the pH and the aqueous activity of potassium (Worden and Morad, 2003). At higher potassium activity and/or lower acidity, illite can be formed instead of kaolinite, even at temperatures as low as 60°C (Worden and Morad, 2003):

$$3\ \text{K-feldspar} + 2\ H^+ + H_2O \rightarrow \text{illite} + 6\ \text{quartz} + 2\ K^+$$

The different clay minerals as reaction products of K-feldspar dissolution for BRTZ and WED3 therefore seems to be the result of different formation water composition. K-feldspar dissolution generally occurs at temperatures >50°C (Wilkinson et al., 2001 as referred by Worden and Burley, 2003).
In WED3 many K-feldspar skeletons leave empty pore space, which is sometimes filled with anhydrite in the deepest samples of the Röt Fringe Sandstone Member. Within the secondary pore space cemented by anhydrite, clay minerals as an alteration product of the feldspar are only rarely observed. Illite as alteration product is only occasionally observed and pre-dates anhydrite cementation.
Both K-feldspar alteration reactions result in the liberation of silica for the formation of quartz cement and hence we can assume quartz overgrowth simultaneously with K-feldspar alteration. Quartz cementation in the form of syntaxial overgrowth is present in the BRTZ and the WED3 samples. The formation of secondary quartz is temperature dependent and can occur over a wide range of temperatures, related to varying diagenetic reactions at which silica is released (Worden and Morad, 2000). Quartz cementation has been observed in sandstones at temperatures as low as 40-60°C, but the rate of precipitation is low (Worden and Morad, 2000). In many sandstones quartz cementation only occurs at temperatures >70-80°C (Worden and Morad, 2000 and Giles et al., 2000 as referred by Worden and Burley, 2003). According to fluid inclusion studies within quartz cement from sandstones in the North Sea Basin, *major* quartz cementation started at ~90°C and continues during further subsidence (Bjorlykke and Egeberg, 1993). This would imply that major quartz cementation started around 160 Ma in WED3 and 90 Ma in BRTZ (Figure 24 and Figure 25 respectively). Fischer et al. (2012) on the other hand, observed early diagenetic, major poikilotopic quartz

cement in German Upper Rotliegend sandstones, which was responsible for a high intergranular cement volume. In addition, Henares et al. (in press), identified well-developed quartz overgrowth as early diagenetic cement in Upper Permian Rotliegend sandstones in the Southern Permian Basin. Hence, the absolute timing of quartz cementation is complex. In WED3 the main phase of syntaxial quartz overgrowth occurred *before* anhydrite cementation. In BRTZ this occurred *after* the anhydrite cementation and the major syntaxial quartz overgrowth seems to be one of the latest stages in the paragenetic sequence. Within the WED3 samples syntaxial quartz overgrowth is more abundant than in the BRTZ samples. In addition, individual quartz cement crystals formed in the WED3 samples, *after* the anhydrite cementation.

The four types of siderite in BRTZ other than the one associated with biotite alteration are probably from a different phase, having a different cation source. The source for Mg and Fe is unclear, but could be smectite to illite transition within clay clasts. Timing of these types is difficult, but at least part of the siderite is post dolomite and prior to anhydrite.

Anhydrite cement occurs locally as nodules and is a relatively late phase in the three fields since it encloses many early carbonate phases as well as K-feldspar skeletons, illite or kaolinite after K-feldspar dissolution, and quartz overgrowth. However, it also fills up oversized pore space since the detrital framework grains practically float in the anhydrite cement. In zones which are essentially free of anhydrite cement, the degree of compaction is higher. This suggests early cementation of anhydrite or replacement of another early cement. Anhydrite fills up secondary pore space after dissolution of detrital K-feldspar and partial alteration to illite in WED2 and WED3 or kaolinite in BRTZ. The calcium and sulfate for anhydrite precipitation is possibly related to circulation of evaporate pore waters (Worden and Burley, 2003), likely of Triassic evaporates as Zechstein is not present, or from early gypsum. In WED3 the anhydrite is only present in the deepest part of the Röt Fringe Sandstone Member at a depth below ~2833m AH, and is virtually absent higher up in the stratigraphy and in the samples from the Hardegsen Formation. This might indicate that the lowest part represents a different lithofacies in which gypsum nodules were formed. Another possibility is that fluid influx occurred from below, and prevention of upward flow due to low permeable shaley intervals within the reservoir. In BRTZ the anhydrite cementation is also restricted to few samples, but without any depth relation (see also the XRD analyses in Table 10). Since the BRTZ samples analysed are rom braided fluvial deposits like the samples from the upper part of WED3 which lack anhydrite, the hypothesis of a different lithofacies for the lowest part of the WED3 core is not likely. The anhydrite cemented interval in WED3 coincides with the low porosity and permeability in the lowest part of the core (see Figure 9, a depth of 26 m below the top of the Röt Fringe Sandstone Member coincides with a depth of 2833 m AH), suggesting that porosity and permeability appear closely related to the presence or absence of anhydrite.

In WED3 the siderite pore-filling cement is very local but occurs in all samples. In the samples where anhydrite is present, the siderite partially replaces the anhydrite cement. The anhydrite dissolution and siderite precipitation possibly occurred in a replacement reaction, thereby preserving the oversized pore cementation structure. In the samples which lack an earlier anhydrite cementation event, the siderite has the same morphology as the siderite which replaced anhydrite, with Mg-rich and highly Mg-rich patches, filling up pore space and replacing detrital minerals. The siderite seems to be initially richest in Mg and becomes more Fe-rich with time, suggestion an enrichment of the formation water with iron. El-ghali et al.

(2006) explain this patchy type of siderite as partial dissolution of Mg-poor siderite and replacement by Mg-rich siderite. In the samples investigated, this should be the other way around. But we also occasionally observed a more gradual increase in the Fe-content of siderite in the cemented zones. This late phase of anhydrite dissolution and siderite cementation event is not observed in the samples from BRTZ. In WED2, the relative timing of siderite and anhydrite could not be established but anhydrite dissolution did not occur. Therefore, we believe that the anhydrite dissolution and replacement by siderite is the result of the influx of CO_2.

The individual, euhedral quartz cement grains in WED3 are never surrounded by anhydrite and may have formed as one of the latest authigenic phases, more or less contemporaneously with siderite cement. The presence of a late phase of quartz precipitation was also concluded by Pestman (1991) for WED3. Barite is interpreted as the latest authigenic phase since it encloses siderite cement.
According to Pestman (1991) both siderite and barite are early phase cements in WED3, with the main phase of siderite pre-dating anhydrite and co-precipitating barite. Based on the interpretation in this study, we have to conclude that siderite and barite (predominantly) post-date anhydrite.

8.2 Geochemical reactions induced by CO_2

Based on the observations, we assigned the following overall reaction to the CO_2 in WED3:

$$\text{K-feldspar} + \text{anhydrite} + Mg^{2+} + Fe^{2+} + CO_2 \rightarrow$$
$$\text{Mg-rich siderite} + \text{quartz} + \text{barite} + Ca^{2+} + K^{+} + Al^{+}$$

The late quartz and barite cements are probably the result of the additional K-feldspar dissolution. K-feldspar is known to contain barium as a trace element. Upon dissolution, the barium will become available for barite precipitation, probably using sulfate from anhydrite dissolution. Dolomite and ankerite are known to (partially) dissolve at low pH conditions. We did not find any indication for late stage dissolution of these minerals. Since dolomite and probably ankerite are oil wet, and oil charging occurred prior to CO_2 accumulation, oil rims could have developed, and protected these carbonates from dissolving after CO_2 influx. The mineralogy of BRTZ does not indicate a potential source of iron and magnesium for the Mg-rich siderite. Biotite is present in BRTZ, but there are no indications that biotite used to be present in WED3. A possibility is that the iron was provided by hematite. Hematite is known to reduce due to hydrocarbon charging thereby liberating the iron and bleaching initially red sediments (Gaupp and Okkerman, 2011). After CO_2 influx, it could react with the dissolved CO_2 to form the siderite cement. The potential source of magnesium is currently unknown. Also, we did not find any sinks for calcium, potassium and aluminium in the samples from WED3. The lack of sources and sinks for several cations suggests mass transfer to and from the sandstones investigated.

Our interpretations suggest a certain amount of CO_2 trapping in Mg-rich siderite. The siderite cementation is local and highly variable between the samples. The average siderite content varies between 0.6 wt% (results from Panterra, see Table 10) and 3.2 wt% (results from Qmineral, see Table 11). A rough calculation based on these values and using an average porosity of the sandstones of 7.2%, a gas saturation of 0.8 and a density of the supercritical CO_2 of 420 kg/m^3 (after Tambach and Obdam, 2007) results in an estimate of 20-58% of the CO_2 which is sequestered in the Mg-rich siderite.

8.3 Timing of CO_2 charging

According to the paragenetic sequence, CO_2 influx was post anhydrite cementation and prior to siderite precipitation. Absolute timing of anhydrite cementation and of the diagenetic processes *prior* to anhydrite cementation are therefore crucial in the absolute timing of CO_2 charging. However, as discussed in the previous section, each of the reactions which occurred prior to anhydrite precipitation, including quartz overgrowth, can occur during eogenesis, but are generally slow at low temperatures. Our hypothesis is based on the interpretation that major quartz overgrowth does not occur until the formation temperature reaches values >90°C. In this case, major quartz overgrowth in WED3 would have started during Late Jurassic (around 160 Ma) and anhydrite cementation started during Early Cretaceous. The tilted half blocks, which were able to trap gas, were formed in WNB during Late Jurassic rifting. As discussed in section 5.4.2, hydrocarbon charging in Triassic reservoirs occurred from Late Jurassic (~160 Ma), after the formation of tilted fault blocks and hence more or less simultaneously with the onset of major quartz overgrowth, until Mid-Cretaceous. CO_2 charging was after hydrocarbon charging since oil relicts are still present in the samples. Based on the relative timing of these events, we believe that the influx of CO_2 could very well be linked to the major uplift during late Cretaceous (Figure 24). Since the CO_2 is thought to be associated with Early Cretaceous volcanism (140 -130 Ma), this would imply CO_2 trapping in a deeper formation and subsequent migration caused by the fault movement and corresponding uplift of the WED3 reservoir.

If the quartz overgrowth in WED3 and subsequent anhydrite cementation occurred during early diagenesis, the absolute timing of the observed mineral reactions prior to anhydrite dissolution would shift to earlier times. Based on the timing of hydrocarbon charging, starting during Late Jurassic, the CO_2 charging could have occurred at any time between Early Cretaceous and the uplift during Late Cretaceous.

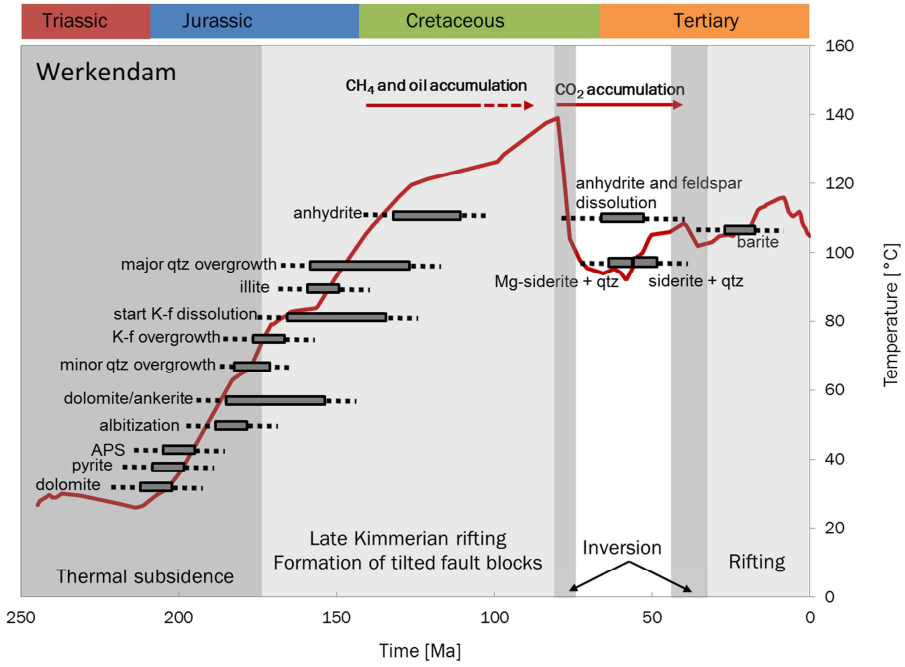

Figure 24. Paragenetic sequence for WED3 integrated with the temperature evolution from basin modelling.

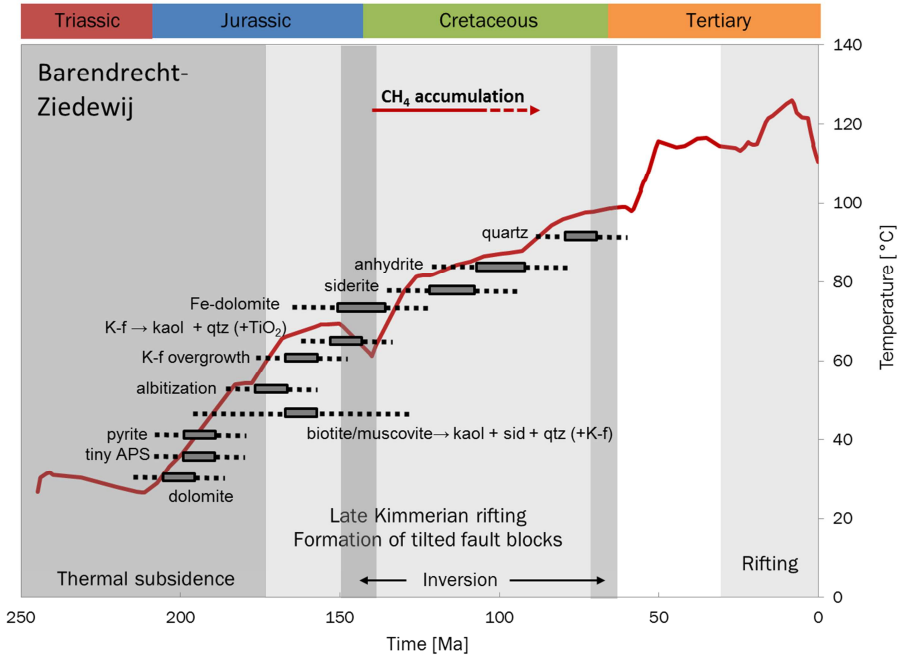

Figure 25. Paragenetic sequence for BRTZ integrated with the temperature evolution from basin modelling.

8.4 Comparison to other case studies

More natural analogue studies to the long term influence of CO_2 on reservoir rocks (sandstones) were published. Three recent studies will be shortly discussed and compared with our results.

8.4.1 Miller field, UK

The gas/oil Miller field in the western margin of South Viking Graben, UK North Sea, contains high concentrations of CO_2 (~28 mol% gas content and 16.8 M tonnes CO_2 in oil) for the last ~70Ma (Lu et al. 2011). Lu et al. (2011) performed a petrographic and stable isotope study to investigate the amount of trapping in carbonates. Calcite is the only carbonate mineral present in the reservoir samples. Stable isotope signatures suggested that most of the calcite concretions were due to early diagenetic precipitation. A late phase of calcite cementation, post-dating CO_2 accumulation, was concluded to be related to the CO_2, allowing the estimation of 6-24% of the CO_2 trapped in calcite. The composition of several formation water samples used in geochemical modelling showed that all carbonate minerals are highly oversaturated. They argue that the high salinity of the brine might inhibit significant CO_2 dissolution and as a result prevent further mineral trapping.

8.4.2 Fizzy field, UK

The Fizzy and Orwell reservoirs are inland dessert sandstones and belong to the Early Permian Rötliegend Group. The Fizzy gas accumulation exist of ~50% CO_2, while the Orwell accumulation has a low CO_2 content. Wilkinson et al. (2009) compared these reservoirs to identify which carbonate minerals are associated with the CO_2. They estimated that CO_2 accumulation occurred more than 50 Ma ago within the Fizzy field. Their results showed that 0.5-30% of the CO_2 is trapped in carbonates, mainly dolomite and to a lesser extent dawsonite.

8.4.3 Montmiral natural analogue, France

The Montmiral natural analogue is reported by Gaus et al. (2004) and Czernichowski-Lauriol et al. (2006). This natural CO_2 field is similar to Werkendam since both are Triassic sandstone reservoirs at high temperature (100°C in Montmiral) and very high CO_2 concentration (97-99% in Montmiral). Mineral dissolution reactions identified to be the result of CO_2 are also similar: K-feldspar and anhydrite dissolution. The precipitation reactions are somewhat different: kaolinite precipitation in secondary porosity, barite and Fe-Mn dolomite/ankerite cementation. A late phase of ankerite corrosion was observed. Geochemical modelling showed that precipitation of quartz should occur, but this was not observed. An explanation for this could not be found. From the paper it is not clear what the source for Mg and Fe is for dolomite/ankerite precipitation. The main difference with our observations in the Werkendam natural analogue is the precipitation of Mg-siderite in WED3 instead of dolomite/ankerite, and the lack of significant clay formation after K-feldspar dissolution.

9 Geochemical modelling

9.1 Introduction

According to our interpretation on the integrated basin modelling and paragenetic sequence, CO_2 accumulation occurred when the Röt Fringe Sandstone Member of WED3 was at roughly 2 kilometre depth, having a temperature between 100 to 110 °C. Prior to the accumulation major uplift (~ 1km.) occurred with corresponding cooling of the reservoir by approximately 40°C. Since burial continued after the uplift event, this final phase is characterised by continuous heating up to 130°C. The described burial history indicates that WED3 underwent major changes in pressure, temperature, and solution chemistry by CO_2 influx. These changes resulted in mineral reactions which define the observed paragenetic sequence. According to our interpretation, dissolution of anhydrite and feldspars took place during or after CO_2 accumulation. Subsequently, siderite, quartz and barite precipitated.
Geochemical batch modelling was performed using PHREEQC to investigate the potential to simulate the CO_2-brine-mineral reactions as observed in WED3. The approach of the modelling was to investigate which model conditions need to be applied to simulate the paragenetic sequence observed in the samples. For this study we focussed on the partial mineral dissolution of anhydrite and K-feldspar and precipitation of siderite (and potentially dolomite) with additional quartz growth. The precipitation of barite is not considered since barium is thought to originate from K-feldspar in which it is present as trace element. The BRTZ mineralogy was equilibrated with CO_2 at a partial pressure of 210 bar to see whether the same mineral reactions would be predicted as observed in WED3. Furthermore, we investigated whether the mineralogy of WED3 is currently in equilibrium with the high CO_2 partial pressure.

9.2 Model input

The WED3 and BRTZ mineral compositions used in the modelling are based on XRD data of Röt Fringe sandstones. They represent average values for the samples. The mineralogy in weight percentage is converted to molar concentrations scaled to 1 litre of brine, using the miner specific density and molar volume, and assuming a porosity of 20% and a gas saturation of 0.5 (Table 7).
EDX analyses showed that illite is essentially iron-free and contains small amounts of magnesium. Magnesium-rich illite is initially used in the modelling. A sensitivity study is performed with respect to the type of illite used in the model and the addition of iron containing minerals to provide iron for siderite precipitation. Pressure changes are not considered in PHREEQC modelling and are therefore neglected. Since the temperature conditions within the reservoir has changed during and after the influx of CO_2 the effect of temperature was investigated.
The CO_2 partial pressure is 210 bar, the temperature in the base case is 120°C.

Table 7. WED and BRTZ mineralogy (mol).

Minerals	Average WED-03	Average BRTZ-01
Quartz	321.41	270.29
Albite	3.19	0.88
Microcline	6.74	10.20
Illite-Mg	1.84	1.24
Kaolinite	-	2.91
Dolomite	3.71	6.69
Siderite	0.69	0.37
Anhydrite	0.85	4.69

9.3 Results

9.3.1 The effect initial Fe concentration in formation water

Werkendam samples showed a late stage siderite cementation that is not observed in Barendrecht samples. The early phase siderite in BRTZ is not observed in the WED3 samples. We tested the hypothesis that siderite can form by addition of CO_2 to a siderite free mineral composition by excluding siderite from the BRTZ mineral composition. For the first model runs, the initial formation water was calculated *in equilibrium with a surplus amount of siderite*. Three models were run for different illite phases, containing iron (FeII and FeIII) or magnesium. Since illite-Fe could be a source of iron, this phase may lead to enhanced siderite formation.

The model results are presented in Table 8. The illite-Mg and illite-FeIII scenarios result in some siderite dissolution during equilibration of the formation water and a corresponding low concentration of Fe. For illite-Mg, most of the dissolved iron is re-precipitated as siderite when equilibrated with CO_2, while no siderite precipitates in the illite-FeIII scenario, but illite-FeIII. For illite-FeII, the model predicts some additional Illite-FeII but no siderite precipitation when equilibrated with CO_2. Instead, a small amount of siderite was predicted to precipitate during the equilibration of the formation water, leading to a low iron content of the solution.

Table 8. Initial brine equilibration with surplus mineralogy and results after equilibration of the brine and BRTZ mineralogy with CO_2 for the three model runs with a different illite phase. The results are shown for the simulated pH, Fe concentration in the brine (mol/L), initial illite and siderite concentration and changes in illite and siderite (mol).

Illite-Mg	pH	Fe	Illite-Mg	d_Illite-Mg	Siderite	d_Siderite
Initial brine	5.56	2.90E-4	surplus	-3.08E-2	surplus	-2.90E-4
CO_2 equilibration	5.12	5.59E-5	1.90E+00	6.47E-2	2.35E-4	2.35E-4
Illite-FeII	pH	Fe	Illite-FeII	d_Illite-FeII	Siderite	d_Siderite
Initial brine	6.76	7.41E-5	surplus	-1.43E-3	surplus	2.85E-4
CO_2 equilibration	4.79	1.10E-12	1.84E+00	2.96E-4	0	0
Illite-FeIII	pH	Fe	Illite-FeIII	d_Illite-FeIII	Siderite	d_Siderite
Initial brine	6.54	4.57E-4	surplus	-1.51E-3	surplus	-7.95E-5
CO_2 equilibration	4.80	9.62E-9	1.84E+00	1.83E-3	0	0

For each of the scenarios, the iron concentration of the solution after equilibration with CO_2 is lower than initially, suggesting that iron present in the formation water could be a source for siderite upon CO_2 influx. According to the illite-FeII and FeIII scenarios, illite is more stable as iron containing mineral than siderite. The model results show that this can be implemented by equilibration of the solution with siderite before CO_2 influx as indicated above, when illite-Mg is considered. As siderite is not expected to be abundant before CO_2 influx, iron probably has a different source. Siderite can form when iron is added to the solution by equilibrating the brine with the element Fe to assess the dependence of siderite formation on the iron content of the formation water. However, if iron illite is allowed to form, iron illite precipitation is still thermodynamically more stable over siderite. Therefore we decided to perform subsequent modelling using Illite-Mg.

The model results show that at a CO_2 partial pressure of 210 bar, iron solubility is 5.59E-05 mol/L for the illite-Mg scenario (Table 8). We investigated whether an increased iron concentration higher than 5.59E-05 mol/L will directly result in enhanced siderite precipitation. For this purpose, elemental iron was added to the formation water. The results show that the amount of siderite precipitation is equal to the iron added minus 5.59E-05 (Figure 26). When the initial solution is already equilibrated with siderite, the amount of siderite formed is equal to 2.35E-04 plus the mol amount of iron added (Figure 26).

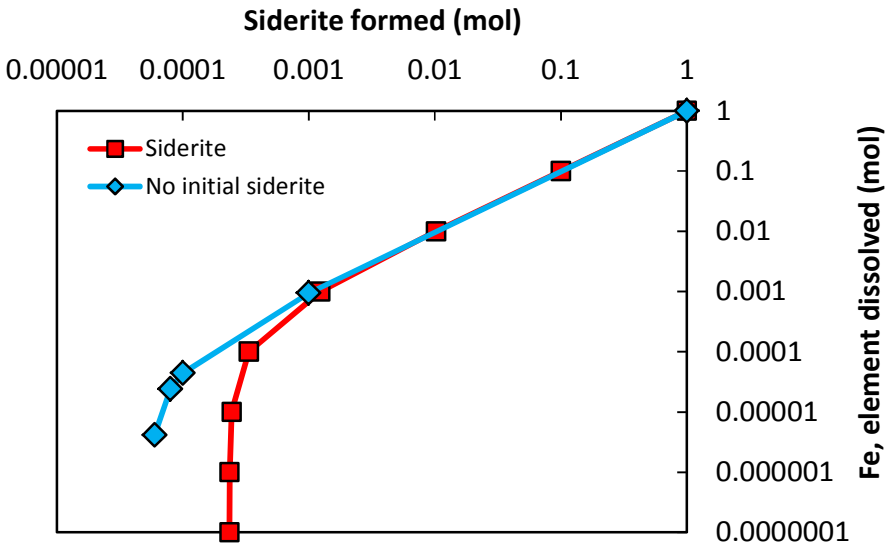

Figure 26. The amount of siderite formed as a function of the amount of iron added to the solution. The model results are presented for an initial formation water with and without equilibration with siderite.

9.3.2 The effect of temperature on precipitation

In addition to the effects of gas influx, the current mineralogy of the Werkendam field has been influenced by the temperature changes due to uplift and burial. The stability of the mineral composition for a range in temperature is calculated with and without CO_2, using the base case at 120°C as a reference implying zero precipitation/dissolution for the minerals at 120°C in the no-CO_2 case (Figure 27). The results show that the temperature dependence is very small for siderite. The effect of CO_2 is larger, yielding increased siderite precipitation.

Quartz precipitation decreases with higher temperatures. The decrease is more pronounced for the case with CO_2. At the modelled temperature range, CO_2 results in a higher amount of quartz precipitation. The CO_2-free case shows quartz dissolution at temperatures above the 120°C base case temperature. Anhydrite has a larger temperature dependence than quartz and siderite. Furthermore, the temperature dependence is reversed showing precipitation with heating and dissolution with cooling. The additional effect of CO_2 is small. The temperature effect of microcline is practically zero, while the addition of CO_2 causes a significant dissolution.

In the no-CO_2 case, the model furthermore predicts additional formation of dolomite, illite and microcline while albite dissolves. Addition of CO_2 shows overall albite dissolution and illite precipitation, but this effect is more pronounced at lower temperatures. Dolomite is now predicted to dissolve instead of precipitate with cooling.

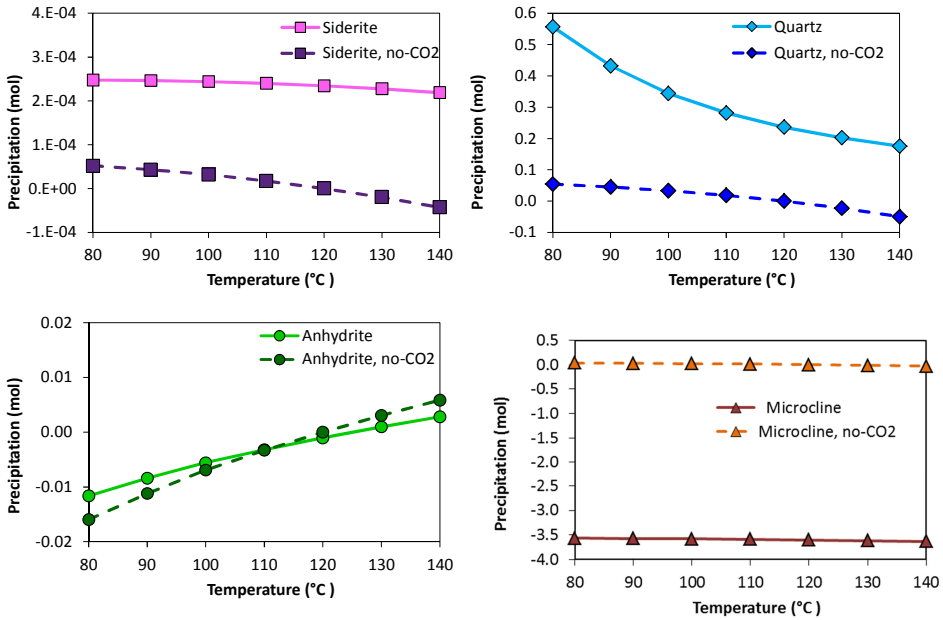

Figure 27. The temperature dependence of siderite, quartz, anhydrite and microcline (K-feldspar) with and without CO_2.

9.4 WED3 and BRTZ model results

Both models are first run using initial siderite equilibration to simulate the composition of the formation water in section 9.4.1. In section 9.4.2 the results are shown for models runs where siderite is excluded from the computation of the initial formation water.

9.4.1 Initial siderite equilibration

The present average mineral compositions of WED3 and BRTZ (including initial siderite) are equilibrated with CO_2 to assess if the WED3 mineralogy is in equilibrium with CO_2 as expected and if the BRTZ composition will move towards the WED3 composition when equilibrated with CO_2. The main difference between the compositions is the lack of kaolinite

in the WED3 reservoir. This results in a distinctly different formation water composition when brine is equilibrated with surplus amounts of the minerals. The solution for BRTZ contains more carbon and calcium. When reacted with CO_2, both WED and BRTZ show minor reactions (Figure 28, upper). The reactions are different for dolomite, microcline and illite, showing opposite precipitation and dissolution reactions. This is probably due to the conversion of illite-Mg to kaolinite with additional formation of dolomite and microcline. Kaolinite precipitation was not included in the WED model.

For all minerals, Werkendam is closest to equilibrium with CO_2 in agreement with the hypothesis of long-term CO_2 sequestration in the field. Additional quartz is predicted to form suggesting that the mineralogy is not yet equilibrated with respect to this mineral. Siderite precipitation in negligible in BRTZ.

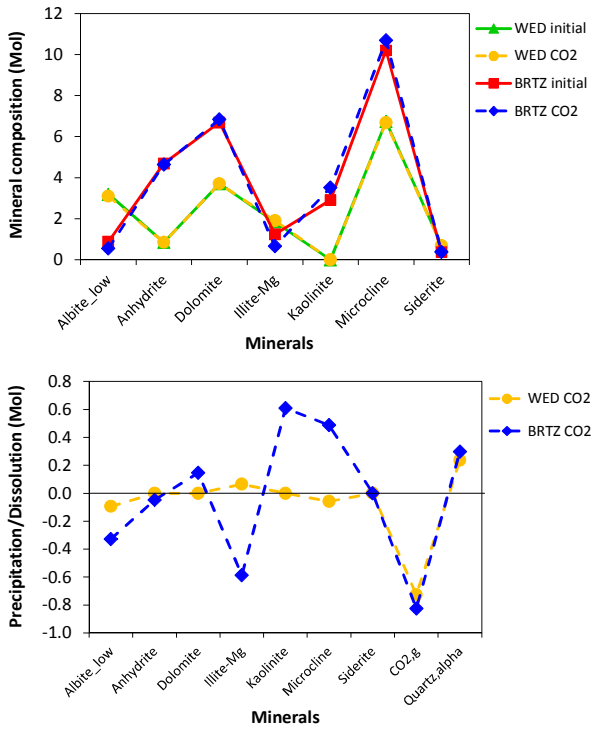

Figure 28. The initial and CO_2 reacted WED and BRTZ mineral compositions (upper) and the mineral changes (lower).

9.4.2 Excluding initial siderite

When the initial formation water is not equilibrated with siderite, the mineral will not form when CO_2 is added. This was discussed in section 9.3.1 for WED3 and also holds for BRTZ. Including Illite-Fe does not induce siderite precipitation. Furthermore, the differences between the fields remain the same. Addition of elemental iron to the solution does result in siderite precipitation (Figure 29). However, quartz is now partially dissolved for both fields. Reactions computed for WED3 and BRTZ are more similar than when equilibrated with siderite except for albite which dissolves for BRTZ and precipitates for WED3. However, when kaolinite is allowed to form in the WED3 model, the mineral changes are approximately

equal. Still the final mineralogy is quite different with complete reaction of illite to kaolinite for BRTZ and partial conversion of illite to kaolinite for WED3 (Figure 30). Kaolinite is predicted to form initially in Werkendam as a result of formation water calculation, and even more when equilibrated with CO_2. Remarkably, kaolinite is only observed in BRTZ and not in the CO_2 containing WED3 field.

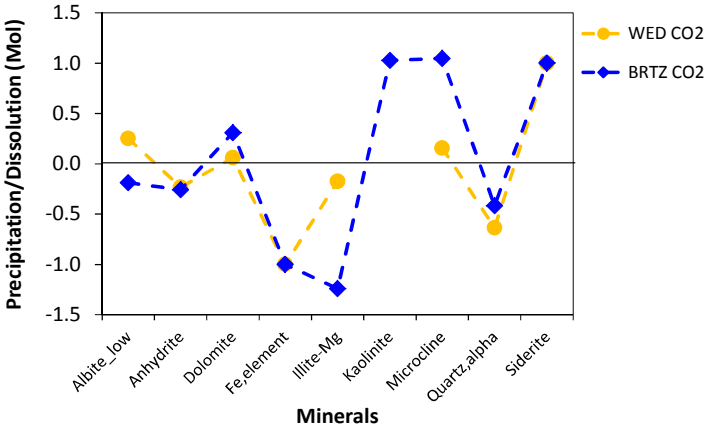

Figure 29. Changes in mineralogy of WED3 and BRTZ when equilibrated with CO_2.

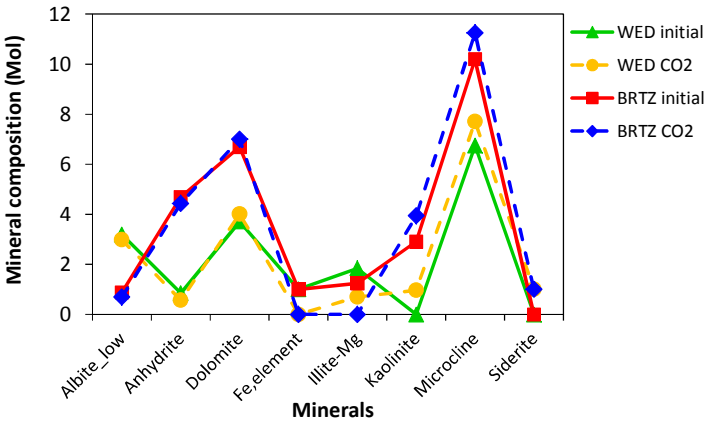

Figure 30. The initial and final mineralogy after equilibration with CO_2 of WED3 and BRTZ .

9.4.3 Additional iron sources

In the previous sections, illite was used as a possible source of iron. However, several other options are available, such as: biotite, glauconite, mica, pyrite and rock fragments. Although Illite-Fe did not induce siderite precipitation, other minerals may. SEM analysis has shown that ferroan dolomite (ankerite), biotite, pyrite and muscovite are present within WED3 and BRTZ, although these are not detected by XRD. This could be due to concentrations below detection limit or due to overlap in peaks (e.g. illite and muscovite/biotite, dolomite and ankerite). For appropriate minerals, the iron containing minerals in BRTZ are considered, since they might have completely reacted in WED3. Both biotite and rock fragments are detrital minerals/grains and should contribute to initial iron content of the rocks. Iron sulphates or oxides can form during diagenesis and provide an iron source for late siderite cementation. Ferroan dolomite cementation is also indicated prior to siderite and hence

could supply iron when dissolved. However, SEM analysis does not show signs of an ankerite dissolution phase in WED3.

Including a small amount of annite (iron endmember of biotite: $KFe_3(AlSi_3)O_{10}(OH)_2$) (0.69 mol) as mica mineral to the BRTZ mineral composition yields an initially stable mineralogy. A comparison is made between two models including and excluding siderite for initial equilibration of the formation water. The formation water has a different composition if annite is included than when equilibrated with only siderite as iron source. Siderite formation caused reduced carbon and iron in solution while calcium is increased by dolomite dissolution. The CO_2 related reactions are not changed by the initial presence of siderite. The model predicts that annite and Illite completely dissolve, albite dissolves partially and anhydrite in lesser amounts. Siderite is predicted to precipitate with kaolinite, microcline, dolomite and quartz. The addition of annite to the mineralogy increases the amount of siderite formed in contact with CO_2 from 4.83E-05 to 6.98E-01. This is consistent with both siderite cementation during CO_2 influx as concluded for WED3, and siderite precipitation in an earlier stage as observed in the BRTZ samples. A model run excluding the high CO_2 partial pressure shows that in BRTZ iron and carbonate are available from respectively biotite and dolomite, stabilizing siderite. Hence, according to the model results a high CO_2 partial pressure is not required for biotite alteration and precipitation of siderite.

Besides annite, iron containing minerals possibly present in WED3 and BRTZ are pyrite, hematite, goethite, ferrihydrite and ilmenite. Models are run for each of these minerals, adding 0.69 mol for each mineral, and combinations of several minerals.
The different minerals have a large effect on the iron concentration of the initial formation water and therefore probably on siderite precipitation. The simulated iron concentration is very low for hematite, goethite and ferrihydrite, higher for pyrite and ilmenite and highest for annite (Figure 31).
The modeled mineral reactions are very similar for model runs which include only hematite, goethite, ferrihydrite, pyrite or ilmenite as iron containing mineral, yielding no siderite precipitation (Table 9). When all iron containing minerals but annite are included in the model (0.69 mol for each mineral) more siderite is formed (2.96 mol siderite), than when only annite is used as iron phase (2.07 mol siderite). Including all iron phases *including* annite, the amount of siderite increases to 5.03 mol (Table 9). In addition to siderite formation, mineral reactions in general are affected (Figure 32). For Werkendam, increased iron leads to more pronounced reactions. This effect is largest for albite, illite and quartz. BRTZ models show a more distinct effect of changing precipitation and dissolution for minerals. This can be attributed to the effect of kaolinite presence.

In conclusion, we currently do not know what the iron source is for the precipitation of siderite, but according to our model results, the presence of annite could result in a considerable amount of siderite when equilibrated with CO_2. In BRTZ the alteration of biotite and corresponding siderite precipitation have occurred regardless of a high CO_2 partial pressure. If annite would have been the iron source for siderite in WED3, the question remains why this reaction did not occur in an earlier phase like in BRTZ. Other iron containing minerals may significantly contribute to the amount of siderite formed.

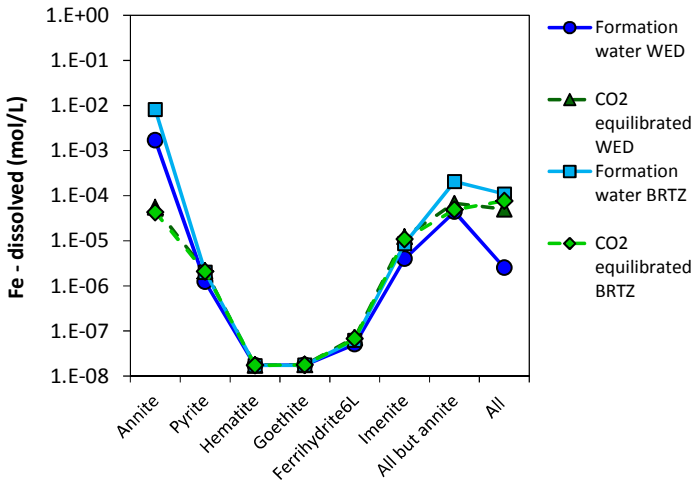

Figure 31. The iron content of the formation water and CO_2 equilibrated fluid.

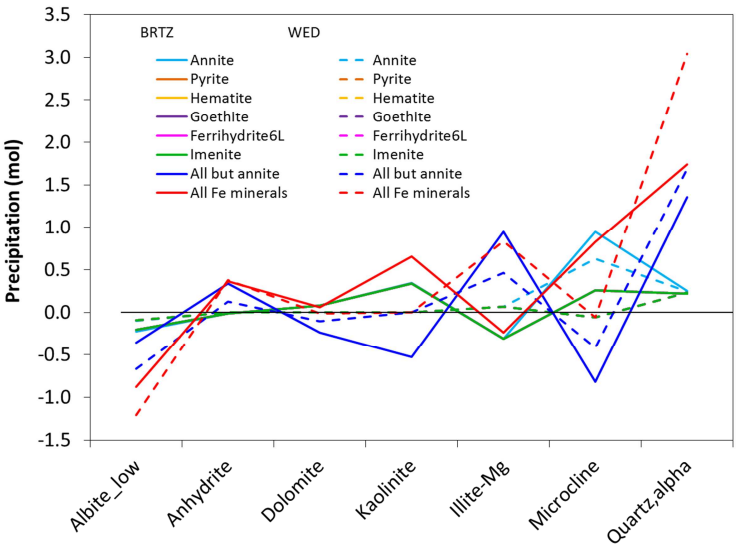

Figure 32. Mineral reactions for the different models with different iron minerals added to the mineralogy.

Table 9. Precipitation and dissolution of the iron containing minerals.

WED	Siderite	d_Siderite	Annite	d_Annite	Pyrite	d_Pyrite	hematite	d_hematite	goethite	d_goethite	ferrihydrite6L	d_ferrihydrite6L	imenite	d_imenite
Annite	2.07	2.07	0	-0.69	0	0	0	0	0	0	0	0	0	0
Pyrite	0	0	0	0	0.69	-9.2E-7	0	0	0	0	0	0	0	0
Hematite	0	0	0	0	0	0	0.69	-1.9E-11	0	0	0	0	0	0
Goethite	0	0	0	0	0	0	0	0	0.69	-1.5E-10	0	0	0	0
Ferrihydrite6L	0	0	0	0	0	0	0	0	0	0	0.69	-2E-08	0	0

Imenite	0	0	0	0	0	0	0	0	0	0	0	0	0.69	-8.3E-6
All but annite	2.96	2.96	0	0	0.49	-0.20	0	-0.69	0	-0.69	0	-0.69	0.69	-2.5E-6
All Fe minerals	5.03	5.03	0	-0.69	0.49	-0.20	0	-0.69	0	-0.69	0	-0.69	0.69	-2.8E-6
BRTZ	Siderite	d_Siderite	Annite	d_Annite	Pyrite	d_Pyrite	hematite	d_hematite	goethite	d_goethite	ferrihydrite6L	d_ferrihydrite6L	imenite	d_imenite
Annite	2.08	2.08	0	-0.69	0	0	0	0	0	0	0	0	0	0
Pyrite	0	0	0	0	0.69	-7.7E-08	0	0	0	0	0	0	0	0
Hematite	0	0	0	0	0	0	0.69	-3.6E-12	0	0	0	0	0	0
Goethite	0	0	0	0	0	0	0	0	0.69	-3E-11	0	0	0	0
Ferrihydrite6L	0	0	0	0	0	0	0	0	0	0	0.69	-4.5E-9	0	0
Imenite	0	0	0	0	0	0	0	0	0	0	0	0	0.69	-2.1E-6
All but annite	2.96	2.96	0	0	0.49	-0.20	0	-0.69	0	-0.69	0	-0.69	0.69	-2.5E-6
All Fe minerals	5.03	5.03	0	-0.69	0.49	-0.20	0	-0.69	0	-0.69	0	-0.69	0.69	-2.7E-6

9.5 Implications

The model results show that initial iron in the formation water, as well as a range of minerals could provide the iron for siderite. This was also pointed out by Xu et al. (2004), showing a dependence of secondary carbonate formation (including siderite) on either the amount of clinoclore and daphnite or glauconite present for different rock types. Glauconite combined with smectite (Pham et al., 2011) and chlorite (Kihm et al., 2012) were also proposed as an iron source for siderite. (Liu et al., 2012) found siderite in the vicinity of pyrite suggesting that pyrite could also be source of iron for siderite. Natural analogues indicated that clay and rock fragments could act as a source for iron (Worden, 2006). Clays may supply iron since smectite is known to release iron during illitization upon burial and diagenesis (e.g. Worden and Morad, 2003). Natural analogues also show that iron could be used to form ankerite instead of siderite (Liu et al., 2011, Lu et al., 2011). Considering the replacement of anhydrite by siderite and a corresponding calcium release, the formation of ankerite would have been more straightforward. Although the source for iron and hence the mineralogy of a rock is very important, the amount of siderite which forms also depends on the brine composition, temperature, and initial CO_2 fugacity; of which initial CO_2 fugacity and brine composition have by far the greatest impact (Zerai et al., 2006). In addition to the mineralogy of the reservoir, the caprock mineralogy could be of importance as iron can diffusion from shale caprock (Xu et al., 2005) and interlayer shale or shale-smear in faults (Tenthorey et al., 2011) into the reservoir. To investigate any interaction between shale, either as caprock or as an interval within the sandstone, and sandstone a reactive transport model would have to be developed.

Another possibility is an influx of iron rich brine contemporaneous with CO_2 charging, since CO_2 can mobilise metals and be responsible for the iron source by reducing the pH, causing dissolution of minerals. Experiments by Alemu et al. (2011) showed that addition of supercritical CO_2 to shale samples increases both iron and silica in solution. However, this is in contradiction to our model results which showed a decrease in iron solubility after equilibration with CO_2. In addition to brine, metals can dissolve in CO_2 therefore mobilizing metals directly by flow of CO_2 (Rempel et al., 2011). Mobilization of metals is also found for CO_2 seepage through sediments (Ardeland and Steinnes, 2010). Kharaka et al. (2010) measured an increase of elements in solution for a field test and attributed this to the dissolution of carbonate minerals and desorption-ion exchange resulting from lowered pH values. Experimental work of Wigand et al. (2008) showed that the increase in solutes could be ascribed to dissolution of dolomite, K-feldspar and albite. Luquot et al. (2012) linked the release of iron to the dissolution of chamosite. Xu et al. (2010) showed that the amount of Fe in solution may again be lowered by CO_2 due to carbonate formation. Wigand et al. (2008) measured an increase in dissolved Fe probably attributed to a lack of carbonate precipitation. The influx of an external iron source is not considered in this study but needs further investigation.

Siderite could be an important mineral for CO_2 trapping by mineral sequestration since iron can be found in several minerals that are common in reservoir rocks and siderite forms by consuming CO_2. Effective siderite mineral trapping is proposed for iron rich sediments such as redbeds (Palandri and Kharaka, 2005 and Palandri et al., 2005) containing: goethite (Garcia et al., 2012), hematite (Murphy et al., 2011), iron oxyhydroxide polymorphs lepidocrocite, goethite, and akaganeite (Lammers et al., 2011) and ferrihydrite (Murphy et al.,

2010). The ferric iron in the deposits must be reduced to ferrous iron to precipitate as siderite, with possible reductants including organic matter, SO_2 (as impurity or waste gas) or H2S (Palandri and Kharaka, 2005). However, addition of sulfur to the system could also lead to pyrite formation in addition to or instead of siderite formation (Murphy et al., 2011, Schoonen et al., 2012). Contrary to siderite, pyrite does not trap CO_2.
Geochemical modelling shows that the observed feldspar/anhydrite dissolution and siderite and quartz (and potentially dolomite) precipitation as a result of CO_2-brine-rock interactions can be simulated. Also the illitization of kaolinite in the presence of K-feldspar is shown. However, the model results highly depend on the assumptions made. A number of input parameters are varied in a sensitivity study indicating that the presence of Al-illite and Fe-minerals are required to simulate the mineral reactions as observed in the petrographic study. Under the conditions applied in this run, the model predicted that the amount of siderite precipitation depends on the type and amount of (minor) iron containing minerals present. More detailed investigation and modelling is required, including reactive transport modelling to explore the possibility of an external iron, to better constrain the amount and type of Fe-minerals required to form the observed amount of siderite. In addition, the source for the high magnesium contents of the siderite, and the stability of Mg-rich siderite should be further explored.

To conclude, geochemical modeling is able to predict the long-term mineral reactions induced by high partial pressures of CO_2, as observed in WED3. It can therefore be a powerful tool in site specific research or reservoir screening. However, the input parameters need to be chosen with great care. Relatively simple XRD mineralogical analyses are not adequate as input. Detailed petrographic analyses and data on brine composition are necessary. Also, an expert opinion on diagenetic processes is required to guide the modelling into the right direction.

10 Summary and concluding remarks

Based on an integrated study including mineralogical and petrographic analysis, basin modelling and literature review, the diagenetic history is assessed for the Werkendam natural analogue and its CO_2-free references; the Werkendam aquifer and Barendrecht-Ziedewij gas field. Comparison of the three fields showed that slight differences in the detrital mineralogy and in burial history result in different paragenetic sequences, regardless of the presence of a high CO_2 partial pressure. This is an important insight which needs to be taken into account when comparing natural analogues with CO_2-free reference cases.
Nonetheless, the comparison allowed us to identify a series of mineral reactions in the samples of the natural analogue which are thought to be induced by the presence of a high partial pressure of CO_2. These include:

- Partial dissolution of anhydrite cement;
- Enhanced dissolution of detrital and authigenic K-feldspar, occasional alteration to illite;
- Replacement of anhydrite cement and detrital grains by Mg-rich siderite with decreasing Mg content in time;
- Precipitation of additional quartz and barite cement.

Geochemical modelling shows that anhydrite dissolution could also be due to a temperature decrease, which occurred as a result of uplift and erosion during the late Cretaceous. However, the anhydrite cement in WED2, which is thought to have experienced a similar uplift as WED3, does not show signs of dissolution. This supports our hypothesis that anhydrite dissolution in WED3 is caused by the presence of CO_2. The early diagenetic dolomite minerals with ankerite rims have not been affected by the CO_2. Since dolomite and probably ankerite are oil wet, and oil charging occurred prior to CO_2 accumulation, we believe that oil rims have developed, and protected these carbonates from dissolving after accumulation and subsequent dissolution of the CO_2.
The iron for siderite precipitation is possibly provided by hematite. Oil charging prior to CO_2 influx might have reduced the hematite, thereby liberating the iron. Subsequent reaction with dissolved CO_2 could have sequestered the iron and carbon as siderite. In the geochemical model, various sources for iron were investigated, including hematite. The model results showed that hematite would not provide iron for siderite in the presence of CO_2. However, the effect of hydrocarbons on hematite reduction cannot be included in such models.
Both the precipitation of quartz and barite are thought to be the result of K-feldspar dissolution. A sink for the released potassium is not observed. No signs for the illitization of initially present kaolinite have been observed. Direct precipitation of illite from K-feldspar is observed, but rare. The absence of kaolinite for illitization or the direct precipitation of illite, and hence the lack of a sink for potassium, might be the reason that K-feldspar dissolution ceased. K-feldspar is often thought to be the most reactive mineral in CO_2 reservoirs, and the presence of K-feldspar in natural analogues is used as an argument that equilibrium is not yet reached. However, we think that equilibrium could have been reached without the complete dissolution of K-feldspar if a suitable sink for potassium is not available. In fact, several natural analogue cases in sandstone reservoirs still contain K-feldspar (e.g. Wilkinson et al., 2009, Lu et al., 2011). Another possibility for the lack of a potassium sinks in the sandstone rocks is the mass transfer of potassium out of the sandstones, possibly into the shaley intervals.

Our conclusions are mainly based on the observations in the petrographic analysis and comparison between the fields. However, there are some unresolved issues with regard to sources and sinks of cations. Like for potassium, we could not find any sink for the calcium from anhydrite which is dissolved and/or replaced by siderite. The anhydrite is only present in the lower part of the Röt Fringe Sandstone Member. A possibility is that CO_2 entered through the fault from one side, migrated laterally due to shaley intervals which acted as caprock, dissolved anhydrite and transported the dissolution products on its way. Since core material is only available at one location within the reservoir, this hypothesis cannot be verified. Furthermore, it is unclear what the source is for magnesium for Mg-rich siderite precipitation. The magnesium concentrations in illite clay within mud clasts in WED3 are slightly higher than in BRTZ, suggesting that magnesium leaching of these mud clasts did not take place. Another possibility is that the magnesium is provided by the shaley intervals, suggesting diffusion of magnesium from the shaley intervals to the sandstones.
Future research should include the assessment of the complete reservoir including the shaley intervals to constrain the potential sources and sinks of cations from dissolved and precipitated minerals. This would allow an improved insight in the dynamic processes related to migration of CO_2 and the importance of mass transfer in the geochemical evaluation of the long-term fate of CO_2 in storage reservoirs. Such an assessment would benefit from a 1-D or even a 2-D reactive transport model which enables the migration of aqueous species between the different intervals.

11 References

Alemu, B.L., Aagaard P., Munz I.A., and Skurtveit E. (2011). Caprock interaction with CO2: A laboratory study of reactivity of shale with supercritical CO2 and brine, Appl. Geochem., 26(12), 1975-1989.

Ague, J.J. and Rye, D.M. (1999). Simple Models of CO2 Release from Metacarbonates with Implications for Interpretation of Directions and Magnitudes of Fluid Flow in the Deep Crust. Journal of Petrology 40: 1443-1462

Ardelan, M.V. and Steinnes E. (2010). Changes in mobility and solubility of the redox sensitive metals Fe, Mn and Co at the seawater-sediment interface following CO2 seepage, Biogeosciences, 7(2), 569-583.

Balen van, R.T., Bergen van, F., Leeuw de, C., Pagnier, H., Simmelink, H., Wees van, J.D., Verweij, J.M. (2000). Modelling the hydrocarbon generation and migration in the West Netherlands Basin, the Netherlands, Geologie en Mijnbouw / Netherlands J of Geosci 79: 29-44.

Barclay S.A. and Worden R.H. (2000). Effects of reservoir wettability on quartz cementation in oil fields. In: Quartz cementation in sandstones: Special Publication 29 of the IAS. ISBN 0-632-05482-4, p 103-118.

Bergen van, M.J., Sissingh, W. (2007). Magmatism in the Netherlands: expression of north-west European rifting history. Edited by Wong, Th.E., Batjes, D.A.J., Jager de, J., Geology of the Netherlands, 197-221.

Berner R.A. (1980). Early diagenesis: A theoretical approach. Princeton University Press, ISBN 0-691-08258-8, 241p.

Bjørkum, P.A., Gjelsvik, N., 1988, An isochemical model for formation of authigenic kaolinite, K-feldspar and illite in sediments. J of Sedim Petrology 58: 506-5011

Bjorlykke, K., Egeberg, P.K., (1993). Quartz cementation in sedimentary basins. AAPG Bulletin 77, 1538 – 1548.

Carothers, W.W., Adami, L.H., Rosenbauer R.J. (1988), experimental oxygen istope fractionation between side&-water and phosphoric acid liberated CO2 – siderite. Geoch et Cosmoch 52, 2445-2450.

Chuhan, F.A., Bjorlykke, K., Lowrey, C. (2000). The role of provenance in illitization of deeply buried reservoir sandstones from Haltenbanken and north Viking Graben, ofshore Norway, Marine and Petroleum Geology 17, 673-689.

Clayton, J. L., Spencer, C. W., Koncz, I., & Szalay, A. (1990). Origin and migration of hydrocarbon gases and carbon dioxide, Békés Basin, southeastern Hungary. Organic Geochemistry, 15, 233-247.

Czernichowski-Lauriol I., Rochelle C., Gaus I., Azaroual M., Pearce J. and Durst P. (2006). Geochemical interactions between CO_2, pore-waters and reservoir rocks. In: Nato Science Series: IV: Earth and Environmental Sciences 65, 157-174.

Dethlefsen, F., Haase, C., Ebert, M., Dahmke, A. (2011). Uncertainties of geochemical modeling during CO2 sequestration applying batch equilibrium calculations. Environmental Earth Sciences, 1-13.

Dieckmann, V., Schenk, H.J., Horsfield, B., Welte, D.H. (1998). Kinetics of petroleum generation and cracking by programmed-temperature closed-system pyrolysis of Toarcian Shales. Fuel 70, 23-31

Dill, H.G., 2001, The geology of aluminium phosphates and sulphates of the alunite group minerals: a review. Earth Science Reviews 53: 35−93

El-ghali M.A.K., Tajori K.G., Mansurbeg H., Ogle N. and Kalin R.M. (2006). Origin and timing of siderite cementation in Upper Ordovician glaciogenic sandstones from the Murzuq basin, SW Libya. Marine and Petroleum Geology 23, 459-471.

Fischer C., Dunckl I., von Eynatten H., Wijbrans J.R. and Gaupp R. (2012). Products and timing of diagenetic processes in Upper Rotliegend sandstones from Bebertal (North German Basin, Parchim Formation, Flechtingen High, Germany). Geological Magazine 149 (5), 827-840.

Garcia, S., Rosenbauer R.J., Palandri J. and Maroto-Valer M.M. (2012). Sequestration of non-pure carbon dioxide streams in iron oxyhydroxide-containing saline repositories. International Journal of Greenhouse Gas Control 7, 89-97.

Gaupp R. and Okkerman J.A. (2011). Diagenesis and reservoir quality of Rotliegend sandstones in the northern Netherlands – A review. In: The Permian Rotliegend of the Netherlands. SEPM Special Publication No. 98, 193-226.

Gaus I., Le Guern C., Pauwels H., Girard J.-P., Pearce J., Shepher T., Hatziyannis G. and Metaxas A. (2004). Comparison of long term geochemical interactions at two natural CO_2-analogues: Montmiral (Southeast Basin, France) and Messokampos (Florina Basin, Greece) case studies. GHGT7 – 7th International Conference on Greenhouse Gas Control Technologies, Vancouver, Canada, 5-9 September 2004, 9 p.

Gaus I., Audigane P., André L., Lions J., Jacquemet N., Durst P., Czernichowski-Lauriol I. and Azaroual M (2008). Geochemical and solute transport modelling for CO_2 storage, what to expect from it? International Journal of Greenhouse Gas Control 2, 605-625.

Geluk M.C. (2005). Stratigraphy and tectonics of Permo-Triassic basins in the Netherlands and surrounding areas. PhD thesis, Utrecht University, the Netherlands. ISBN 900-393-3911-2.

Gilfillan S.M.V., Lollar B.S., Hollan G. et al. (2009). Solubility trapping in formation water as dominant CO_2 sink in natural gas fields. Nature 458, 614-618

Harwood, G. (1988). Microscopic techniques: II. Principles of sedimentary petrography. Edited by Maurice Tucker, Techniques in Sedimentology, 108-173

Hellevang, H., Aagaard, P., Oelkers, E., Kvamme, B. (2005). Can Dawsonite Permanently trap CO2. Environmental Science and Technology 39, 8281-8287.

Hellevang, H., Declercq, J., Aagaard, P. (2011). Why is dawsonite absent in CO2 charged reservoirs. Oil & Gas Science and Technology 66, 119-135.

Henares S., Bloemsma M.R., Donselaar M.E., Mijnlieff H.F., Redjosentono A.E., Veldkamp H.G. and Weltje G.J. (in press). Detrital anhydrite occurrence in aeolian sandstone diagenesis: Implication for prediction of reservoir quality – Upper Rotliegend, The Netherlands.

Jager de, J., Doyle, M.A., Grantham, P.J., Mabillard, J.E. (1996). Hydrocarbon habitat of the West Netherlands Basin. Rondeel et al. Geology of gas and oil under the Netherlands, 191-206

Jager de, J. (2003). Inverted basins in the Netherlands, similarities and differences. Geologie en Mijnbouw / Netherlands Journal of Geosciences 83, 355-366.

Jager de, J. (2007). Geological development. Edited by Wong, Th.E., Batjes, D.A.J., Jager de, J., Geology of the Netherlands, 5-26.

Jamtveit, B., Bucher-Nerminen, K., Stijfhoorn, D.E. (1991). Contact metamorphism of layered shale-carbonate sequences in the Oslo rift: I Buffering, infiltration and the mechanisms of mass transport. Journal of Petrology 33, 377-422.

Jonas E.C. and McBride E.F. (1977). Diagenesis of sandstone and shale: application to exploration for hydrocarbons. Department of geological sciences, the University of Texas at Austin, Texas.

Kampman N., Bickle M.J., Maskell A. et al. (2014). Drilling and sampling a natural CO_2 reservoir: Implications for fluid flow and CO_2-fluid-rock reactions during CO_2 migration through the overburden. Chemical Geology 369, 51-82.

Kaszuba, J.P., Viswanathan, H.S., Carey, J.W. (2011). Relative stability and significance of dawsonite and aluminum minerals in geological carbon sequestration, Geophysical research letters 38, 1-15.

Kharaka, Y.K., Thordsen J.J., Kakouros E., Ambats G., Herkelrath W.N., Beers S.R., Birkholzer J.T., Apps J.A., Spycher N.F., Zheng L., Trautz R.C., Rauch H.W. and Gullickson K.S. (2010). Changes in the chemistry of shallow groundwater related to the 2008 injection of CO2 at the ZERT field site, Bozeman, Montana. Environmental Earth Sciences 60(2), 273-284.

Kihm, J., Kim J., Wang S. and Xu R. (2012). Hydrogeochemical numerical simulation of impacts of mineralogical compositions and convective fluid flow on trapping mechanisms and

efficiency of carbon dioxide injected into deep saline sandstone aquifers. Journal of Geophysical Research B Solid Earth, 117(6).

Koenen, M., Wasch, L.J., 2012, KIP Schoon Fossiel 2011 - Application of QEMSCAN analyses in geochemical evaluations. TNO internal report, 34 p.

Koenen M., ter Heege J. and Peeters R. (2014). Transport properties of intact caprocks and effects of CO_2-water-rock interaction – CO_2 induced mineral reactions in sandstone reservoirs. CATO-2 Deliverable WP 3.3 –D12.

Lanson B, Beaufort D, Berger G., Baradat J and Lacharpagne J-C. (1996). Illitization of diagenetic kaolinite-to-dickite conversion series : late-stage diagenesis of the lower Permian Rotliegend Sandstone reservoir, offshore of the Netherlands. Journal of Sedimentary Research 66 (3), 501-518.

Lammers, K., Murphy R., Riendeau A., Smirnov A., Schoonen M.A.A. and Strongin D.R. (2011). CO2 sequestration through mineral carbonation of iron oxyhydroxides. Environmental Science and Technology 45(24), 10422-10428.

Liu, N., Liu L., Qu X., Yang H., Wang L. and Zhao S. (2011). Genesis of authigene carbonate minerals in the Upper Cretaceous reservoir, Honggang Anticline, Songliao Basin: A natural analog for mineral trapping of natural CO2 storage. Sedimentary Geology 237(3-4), 166-178.

Lu, J., Wilkinson, M., Haszeldine, R.S., Boyce, A.J. (2011). Carbonate cements in Miller field of the UK North Sea: a natural analog for mineral trapping in CO2 geological storage. Environmental Earth Sciences 62(2), 507–517.

Luquot, L., Andreani M., Gouze P. and Camps P. (2012). CO2 percolation experiment through chlorite/zeolite-rich sandstone (Pretty Hill Formation – Otway Basin–Australia). Chemical Geology 294–295(0), 75-88.

McCrea, J. (1950). On the isotopic chemistry of carbonates and palaeo-temperature scale. The Journal of Chemical Physics 18, 849-57.

Milliken, K.L. (2005). Late Diagenesis and Mass Transfer in Sandstone-Shale Sequences. In: Sediments, diagenesis, and sedimentary rocks, volume 7 treatise on geochemistry. Edited by F.T. Mackenzie, 159-190.

Morad, S. (1998). Carbonate cementation in sandstones: distribution patterns and geochemical evolution. In: Carbonate cementation in sandstones: distribution patterns and geochemical evolution. ISBN 0-632-04975-8.

Morad, S. (1990). Mica alteration reactions in Jurassic reservoir sandstones from the Haltenbaken area, offshore Norway. Clays and Clay Minerals 38, 584-590.

Murphy, R., Lammers K., Smirnov A., Schoonen M.A.A. and Strongin D.R. (2011). Hematite reactivity with supercritical CO2 and aqueous sulfide. Chemical Geology 283(3-4), 210-217.

Murphy, R., Lammers K., Smirnov A., Schoonen M.A.A. and Strongin D.R. (2010). Ferrihydrite phase transformation in the presence of aqueous sulfide and supercritical CO2, Chemical Geology 271(1-2), 26-30.

Nelskamp S., Verweij, J.M. (2012). Using basin modeling for geothermal energy exploration in the Netherlands – an example from the West Netherlands Basin and Roer Valley Graben, TNO internal report, 1-113.

Palandri, J.L. and Kharaka Y.K. (2005). Ferric iron-bearing sediments as a mineral trap for CO 2 sequestration: Iron reduction using sulfur-bearing waste gas. Chemical Geology 217(3-4 SPEC. ISS.), 351-364.

Palandri, J.L., Rosenbauer R.J. and Kharaka Y.K. (2005). Ferric iron in sediments as a novel CO2 mineral trap: CO 2-SO2 reaction with hematite. Applied Geochemistry 20(11), 2038-2048.

Pe-Piper, G., Dolansky L.M. (2005). Early diagenetic origin of Al phosphate-sulfate minerals (woodhouseite and crandallite series) in terrestrial sandstones, Nova Scotia, Canada, American Mineralogist 90, 1434-1441.

Pe-Piper, G., Karim, A., Piper, D.J.W. (2011). Authigenesis of titania minerals and the mobility of Ti: new evidence from pro-deltaic sandstones, Cretaceous Scotian Basin, Canadian Journal of Sedimentary Research 81, 762-773.

Pestman P.J. (1991). Sedimentology, petrology and reservoir properties of cores 1, 2 and 3 from well Werkendam-3. Final Report prepared for Nederlandse Aardolie Maatschappij B.V.

Pettijohn F.J., Potter P.E. and Siever R. (1987). Sand and Sandstone, second edition. ISBN 0-387-96355-3.

Pham V.T.H., Lu P., Aagaard P, Zhu C. and Hellevang H. (2011). On the potential of CO 2-water-rock interactions for CO 2 storage using a modified kinetic model. International Journal of Greenhouse Gas Control, 5(4), 1002-1015.

Pudlo D., Reitenbach V., Albrecht D., Ganzer L., Gernert U., Wienand J., Kohlhepp B. and Gaupp R. (2012). The impact of diagenetic fluid-rock reactions on Rotliegend sandstone composition and petrophysical properties (Altmark area, central Germany). Environmental Earth Sciences 67, 369-384.

Rasmussen, B. (1996). Early-diagenetic REE-phosphate minerals (florencite, crandallite, gorceixite and xenotime) in marine sandstones: A major sink for oceanic phosphorus. Americal Journal of Science 296, 601–632.

Rasmussen, B., Buick, R., Taylor, W.R. (1998). Removal of oceanic REE by authigenic precipitation of phosphatic minerals. Earth and Planetary Science Letters 164, 135–149.

Rempel, K.U., Liebscher A., Heinrich W., and Schettler G. (2011). An experimental investigation of trace element dissolution in carbon dioxide: Applications to the geological storage of CO 2, Chem. Geol., 289(3-4), 224-234.

Rosenbaum, J., Sheppard, S.M.F. (1986). An isotopic study of siderites, dolomites and ankerites at high temperatures. Geochimica et Cosmochimica Acta 50, 1147-1150.

Saigal, G.C., Morad, S., Bjorlykke, K., Egeberg, P.K., Aagaard P. (1988). Diagenetic albitization of detrital K-feldspar in Jurassic lower Cretaceous, and Tertiary clastic reservoir rocks from offshore Norway, I. Textures and origin. Journal of Sedimentary Petrology 58, 1003-1013.

Schoell, M. (1988). Multiple origins of methane in the Earth. Chemical Geology 71, 1-10.

Schoonen, M.A.A., Sklute E.C., Dyar M.D. and Strongin D.R. (2012). Reactivity of sandstones under conditions relevant to geosequestration: 1. Hematite-bearing sandstone exposed to supercritical carbon dioxide commingled with aqueous sulfite or sulfide solutions. Chemical Geology 296-297, 96-102.

Sherwood-Lollar, B., Ballentine, C. J., & O'Nions, R. K. (1997). The fate of mantle-derived carbon in a continental sedimentary basin: Integration of C/He relationships and stable isotopic signatures. Geochimica et Cosmochimica Acta 61, 2295-2307.

Sissingh, W. (2004). Paloeozoic and Mesozoic igneous activity in the Netherlands a tectonomagmatic review. Geologie en Mijnbouw / Netherlands Journal of Geosciences 83: 113-134

Spötl, C. (1990). Authigenic aluminium phosphate-sulphates in sandstones of the Mitterberg Formation, Northern Calcareous Alps, Austria. Sedimentology 37, 837−845.

Tambach T.J. and Obdam A.N.M. (2007). Phase behavior of CO_2-gas mixtures including adiabatic processes. TNO internal report. 2007-U-R0732/B

Tenthorey, E., Boreham, C.J., Hortle, A.L., Underschultz, J.R. and Golding, S.D. (2011). Importance of mineral sequestration during CO2 gas migration: A case study from the Greater gorgon area. Energy Procedia 4, 5074 – 5078.

Watson M.N., Zwingmann N. and Lemon N.M. (2004). The Ladbroke Grove-Katnook carbon dioxide natural laboratory: A recent CO_2 accumulation in a lithic sandstone reservoir. Energy 29, 1457-1466.

Wigand, M., Carey J.W., Schütt H., Spangenberg E., and Erzinger J. (2008). Geochemical effects of CO2 sequestration in sandstones under simulated in situ conditions of deep saline aquifers. Applied Geochemistry 23(9), 2735-2745.

Wilkinson, M., Haszeldine, R.S., Fallick, A.E., Odling, N., Stoker, S.J., Gatliff, R.W. (2009). CO2-mineral reaction in a natural analogue for CO2 storage—implications for modeling. Journal of Sedimentary Research 79, 486–494.

Wolterbeek, T. (2010), Anhydrite Caprock dissolution Behaviour: Mechanisms and Implications for Sealing Capacity. Igitur (Master thesis abstract).

Worden, R.H. and Burley, S.D. (2003). Sandstone diagenesis: the evolution of sand to stone. Edited by Burley S.D., Worden, R.H., Sandstone diagenesis Recent and Ancient, Reprint Series Volume 4 of the International Association of Sedimentologists, 3-44.

Worden, R.H. (2006). Dawsonite cement in the Triassic Lam Formation, Shabwa Basin, Yemen: A natural analogue for a potential mineral product of subsurface CO2 storage for greenhouse gas reduction. Marine and Petroleum Geology 23, 61-77.

Worden R.H. and Morad S. (2000). Quartz cementation in oil field sandstones: a review of the key controversies. In: Quartz cementation in sandstones, edited by R. Worden and S. Morad. ISBN 0-632-05482-4.

Worden R.H. and Morad S. (2003). Clay minerals in sandstones: controls on formation, distribution and evolution. In: Clay mineral cements in sandstones, edited by R. Worden and S. Morad. ISBN 1-40510-587-9.

Wycherley, H., Fleet, A. and Shaw, H. (1999). Some observations on the origins of large volumes of carbon dioxide accumulations in sedimentary basins. Marine and Petroleum Geology 16, 489-494.

Xu, T., Apps J.A., and Pruess K. (2004). Numerical simulation of CO2 disposal by mineral trapping in deep aquifers. Applied Geochemistry, 19(6), 917-936.

Xu, T., Apps J.A., and Pruess K. (2005). Mineral sequestration of carbon dioxide in a sandstone-shale system, Chem. Geol., 217(3-4 SPEC. ISS.), 295-318.

Xu, T., Kharaka Y.K., Doughty C., Freifeld B.M., and Daley T.M. (2010). Reactive transport modeling to study changes in water chemistry induced by CO 2 injection at the Frio-I Brine Pilot. Chemical Geology, 271(3-4), 153-164.

Yurkova, R.M. (1970). Comparison of post-dedimentary alterations of oil-, gas- and water-bearing rocks. Sedimentology 15, 53-68.

Zerai, B., Saylor, B.Z., Matisoff, G. (2006). Computer simulation of CO2 trapped through mineral precipitation in the Rose Run Sandstone, Ohio. Applied Geochemistry 21, 230–240.

Zhang, T., Zhang, M., Bai., B., Wang, X., Li, L. (2008). Origin and accumulation of carbon dioxide in the Huanghua depression, Bohai Bay Basin, China. AAPG Bulletin 92, 348 -358.

Appendix A

Chronostratigraphy		BRTZ-03 Stratigraphic unit	Top	Bottom	WED-03 Stratigraphic unit	Top	Bottom
Cenozoic	Neogene	Upper North Sea Group	0	415	QUATER. UNDIFF.	0	59
					Maassluis Formation	59	200
					Oosterhout Formation	200	368
					Breda Formation	368	514
	Oligocene	Middle North Sea Group	415	534	Rupel Clay Member	514	586
					Vessem Member	586	593
	Eocene	Asse Member	534	563	Unconformity - possible erosion ~200 m		
		Brussels Sand Member	563	722			
		Ieper Member	722	880	Ieper Member	593	593
		Basal Dongen Sand Member	880	900	Basal Dongen Sand Member	593	683
					Dongen Formation	683	697
	Paleocene	Landen Formation	900	941	Unconformity - possible erosion ~900 m		
Cretaceous	Late Cretaceous	Houthem Formation	941	998			
		Ommelanden Formation	998	1412			
		Texel Formation	1412	1425			
	Early Cretaceous	Upper Holland Marl Member	1425	1457			
		Middle Holland Claystone Member	1457	1476			
		Holland Greensand Member	1476	1589			
		Lower Holland Marl Member	1589	1680			
		De Lier Member	1680	1740			
		Nieuwerkerk Formation	1740	2191	Alblasserdam Member	717	1680
Jurassic	Late Jurassic				Middle Brabant Marl Member	1680	1686
	Middle Jurassic	Unconformity - possible erosion ~200 m			Middle Brabant Limestone Member	1686	1756
					Lower Brabant Marl Member	1756	1806
					Lower Brabant Limestone Member	1806	1843
		Werkendam Formation	2191	2370	Upper Werkendam Member	1843	1913
					Middle Werkendam Member	1913	1973
					Lower Werkendam Member	1973	2197
	Early Jurassic				Posidonia Shale Formation	2197	2220
		Aalburg Formation	2370	2595	Aalburg Formation	2220	2569
Triassic	Late Triassic	Sleen Formation	2595	2618	Sleen Formation	2569	2601
		Upper Keuper Claystone Member	2618	2654	Upper Keuper Claystone Member	2601	2615
		Dolomitic Keuper Member	2654	2679	Dolomitic Keuper Member	2615	2640
		Red Keuper Claystone Member	2679	2681	Red Keuper Claystone Member	2640	2648
	Middle Triassic	Unconformity			Middle Muschelkalk Marl Member	2648	2660
					Muschelkalk Evaporite Member	2660	2672
		Lower Muschelkalk Member	2681	2699	Lower Muschelkalk Member	2672	2710
		Upper Röt Fringe Claystone Member	2699	2724	Upper Röt Fringe Claystone Member	2710	2727
		Röt Fringe Sandstone Member	2724	2767	Röt Fringe Sandstone Member	2727	2786
		Lower Röt Fringe Claystone Member	2767	2788	Lower Röt Fringe Claystone Member	2786	2819
	Early Triassic	Solling Claystone Member	2788	2810	Solling Claystone Member	2819	2833
		Basal Solling Sandstone Member	2810	2813	Basal Solling Sandstone Member	2833	2839
		Unconformity			Hardegsen Formation	2839	2859
					Upper Detfurth Sandstone Member	2859	2891
		Lower Detfurth Sandstone Member	2813	2843	Lower Detfurth Sandstone Member	2891	2907
		Upper Volpriehausen Sandstone Member	2843	3035	Upper Volpriehausen Sandstone Member	2907	2982
					Lower Volpriehausen Sandstone Member	2982	3023
					Lower Buntsandstein Formation	3023	3125

Figure 33. Lithostratigraphy for BRTZ3 and WED3. True vertical depths and thicknesses of the Members that are present in both wells. The lithostratigraphic data are adapted from www.nlog.nl. Unconformities in the stratigraphy could indicate possible erosion or no deposition.

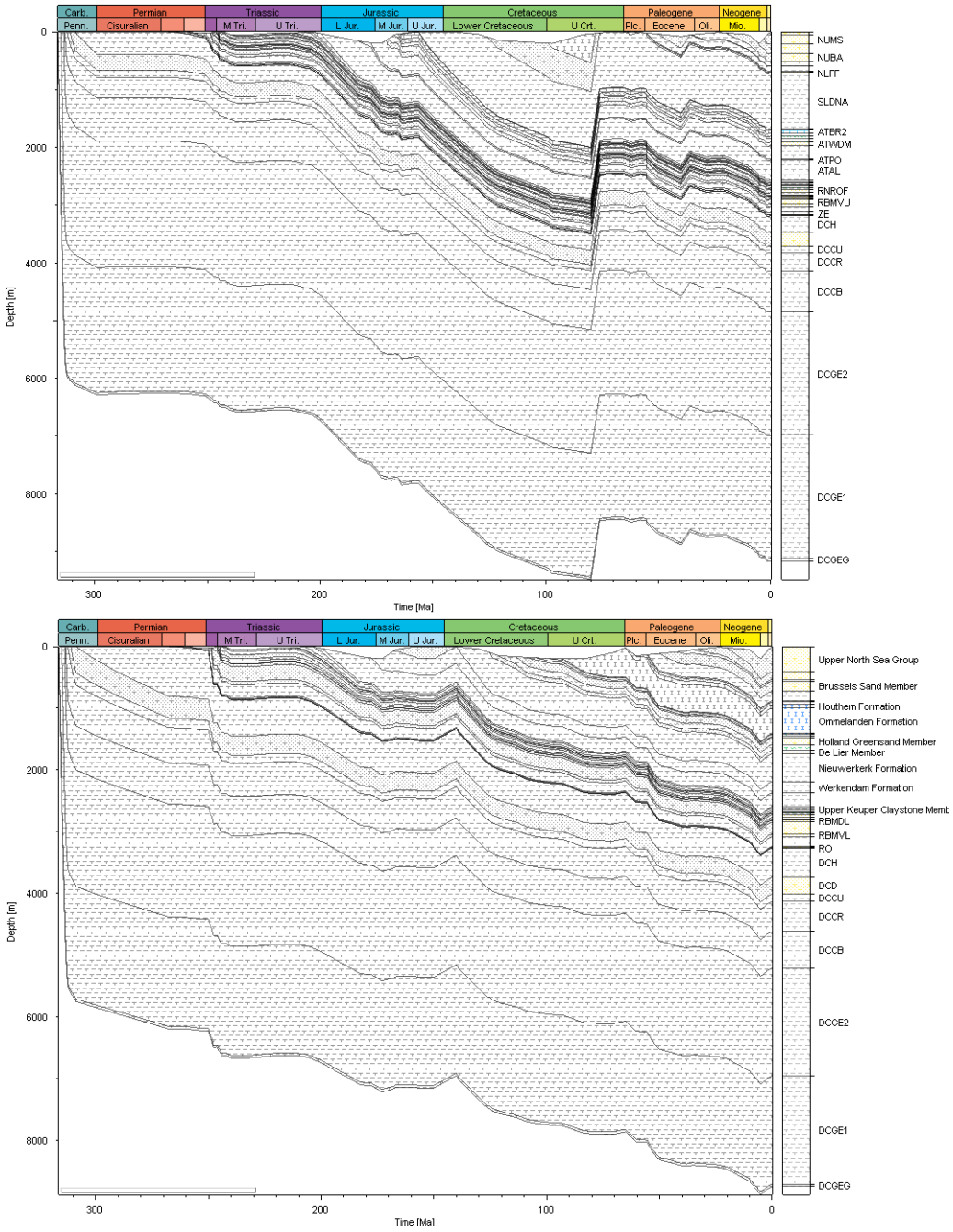

Figure 34. Burial history of sediment sequence in WED3 (upper) and BRTZ3 (lower). The Röt Fringe Sandstone Member is the RNROF-layer.

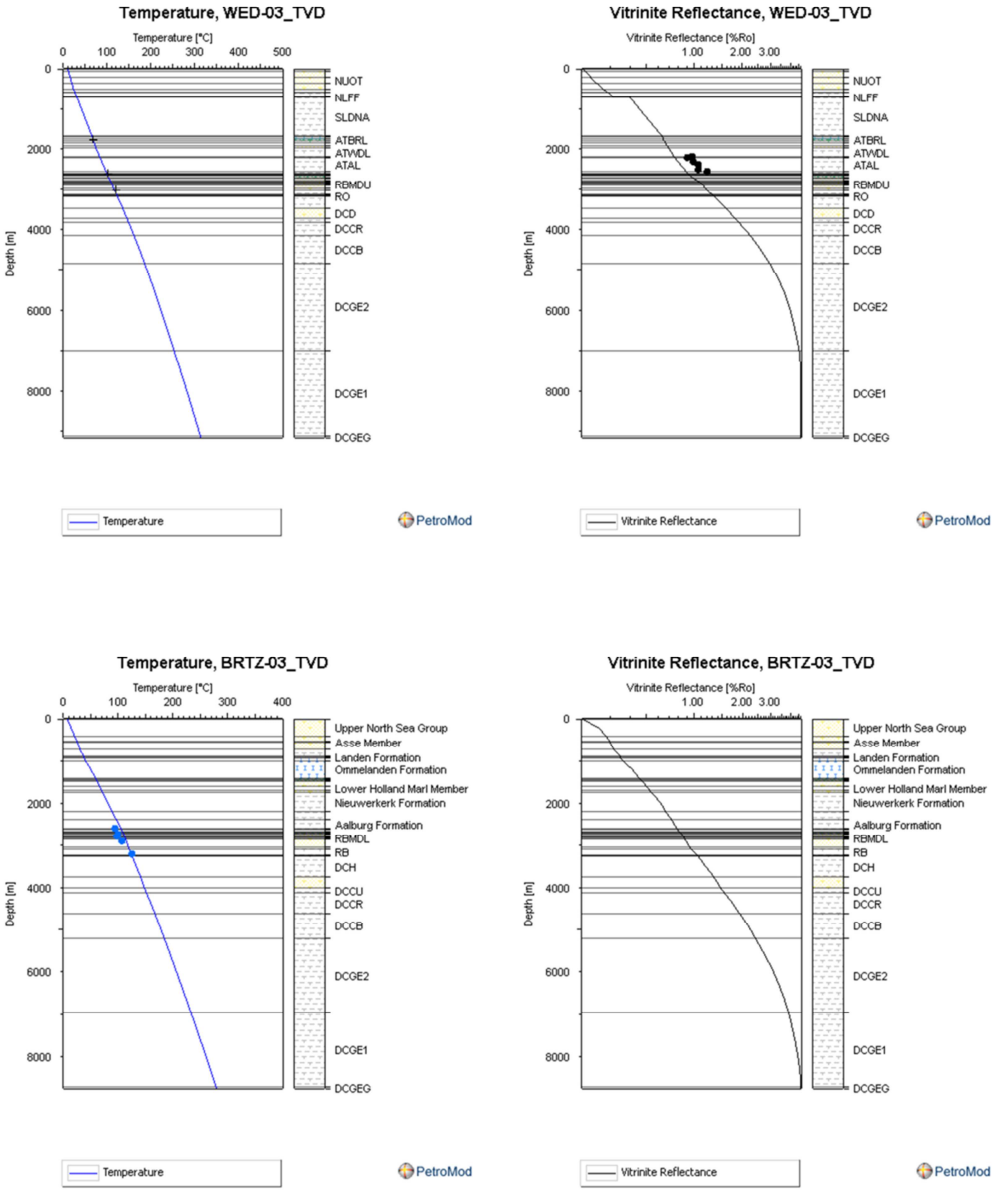

Figure 35. Left: Present day temperature calibration; The black crosses and blue dots represent temperature measurements from well WED3 and BRTZ3, respectively. Right: Vitrinite reflectance calibration; The black dots in the upper right figure represent vitrinite reflectance measurements for WED3. Vitrinite reflectance measurements were not performed for BRTZ3.

Appendix B

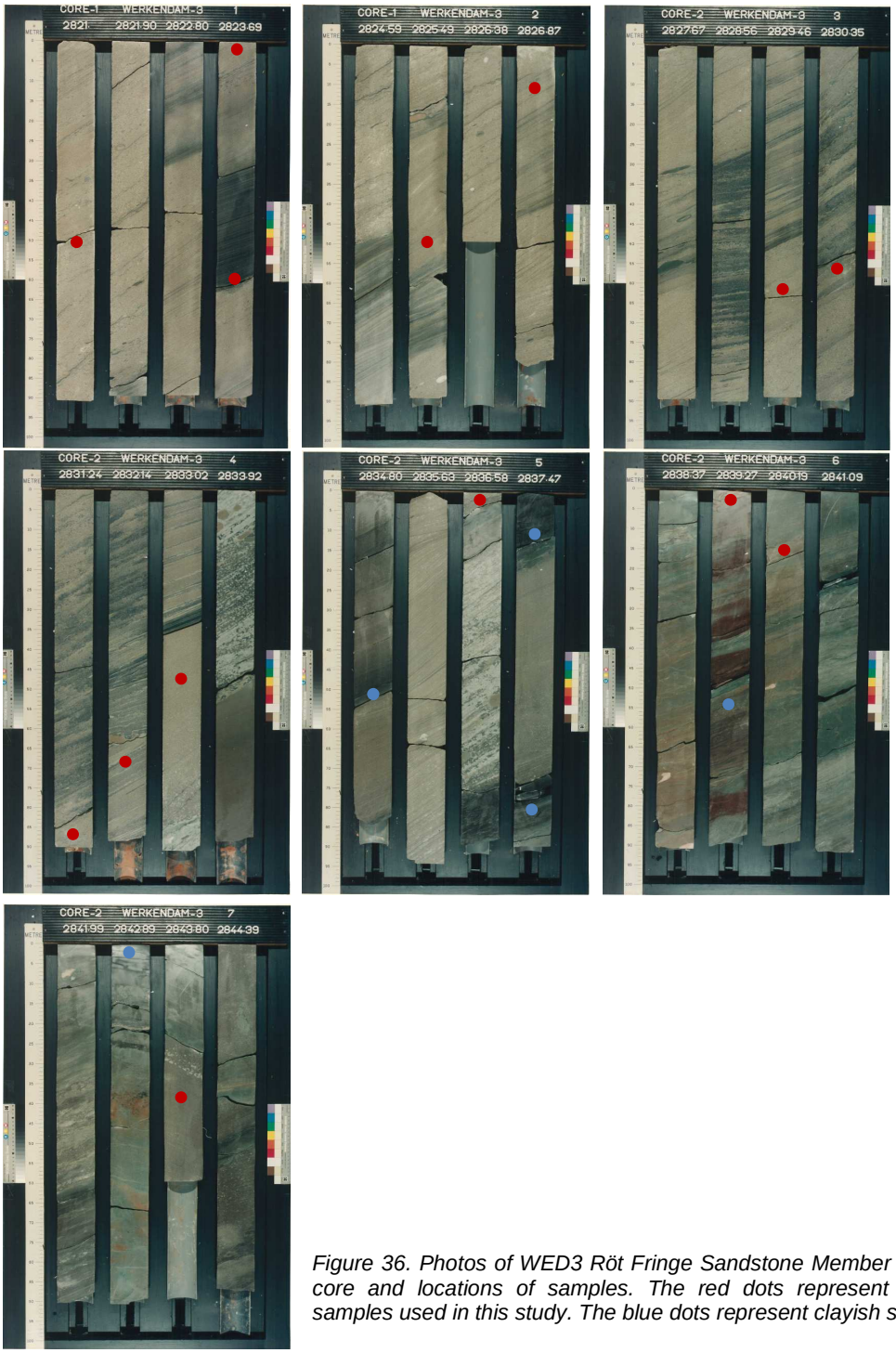

Figure 36. Photos of WED3 Röt Fringe Sandstone Member (CO_2 reservoir) core and locations of samples. The red dots represent the sandstone samples used in this study. The blue dots represent clayish samples.

Figure 37. Photos of BRTZ Röt Fringe Sandstone Member (CO_4 reservoir) core and locations of samples. The red dots represent the sandstone samples used in this study. The blue dots represent clayish samples.

Appendix C

*Table 10. Whole rock XRD results, obtained from SGS and Panterra. * Measured by Panterra, with a less extensive list of minerals. - = not measured. Tr = trace amount. Note that XRD is not able to distinguish between illite and muscovite, and between kaolinite and chlorite. Green: sheetflood lithofacies.*

	Quartz	Plagioclase	K-feldspar	Illite	Kaolinite	Dolomite	Siderite	Anhydrite	Apatite	Total feldspar
WED 3.1	87.81	2.50	0.02	1.73	0	7.94	0	0	0	2.52
WED 3.2	57.21	8.98	3.69	27.02	0	0	3.09	0	0	12.68
WED 3.3	85.62	7.71	4.27	1.58	0	0.01	0.80	0	0	11.98
WED 3.3.1*	80	2.00	10	3.00	0	4.00	1.00	0	-	12.00
WED 3.3.2*	83.00	2.00	7.00	4.00	0	4.00	tr	0	-	9.00
WED 3.4	86.12	8.80	3.84	1.18	0	0.04	0	0	0	12.64
WED 3.4.1*	80	2.00	13.00	3.00	0	1.00	1.00	0	-	15.00
WED 3.4.2*	80	2.00	11.00	4.00	0	3.00	tr	0	-	13.00
WED 3.5	81.43	6.50	1.63	0.61	0	1.00	0.70	**8.13**	0	8.12
WED 3.5.2*	74.00	2.00	9.00	5.00	0	7.00	1.00	**2.00**	-	11.00
B1.1*	66.00	1.00	14.00	3.00	**5.00**	10	0	1.00	-	15.00
B1.3*	56.00	1.00	10	1.00	**4.00**	0	0	28.00	-	11.00
B1.4*	69.00	tr	9.00	1.00	**2.00**	17.00	0	2.00	-	9.00
B1.5*	76.00	1.00	11.00	2.00	**6.00**	1.00	1.00	2.00	-	12.00
B1.6*	74.00	1.00	12.00	4.00	**7.00**	1.00	1.00	0	-	13.00
B1.8*	68.00	1.00	11.00	13.00	**5.00**	2.00	0	0	-	12.00
B1.9*	68.00	tr	9.00	10	**9.00**	4.00	0	0	-	9.00
B1.10*	60	1.00	12.00	1.00	**4.00**	2.00	tr	20	-	13.00
B1.13*	74.00	tr	16.00	2.00	**5.00**	tr	tr	3.00	-	16.00
WED 2.1	82.16	9.72	0	8.13	0	0	0	0	0	9.72
WED 2.2	92.54	0	0	1.61	0.03	4.09	0	1.70	0	0
WED 2.3	76.98	0	0	0.01	0	21.70	0	1.30	0	0
WED 2.4	92.66	5.92	0	1.15	0	0	0	0.01	0	5.92
WED 2.5	88.26	4.00	0	7.72	0.01	0	0	0	0	4.00

Table 11. XRD results from Qmineral for samples selected for isotope analysis, with special focus on the carbonate content. Note that XRD is not able to distinguish between illite and muscovite, and between kaolinite and chlorite. The Fe/Mg ratio of ankerite was modelled based on the asymmetry of the ankerite peaks. The Fe content of ankerite adds up to 1 with Mg, e.g. Ankerite_Fe0.2 is $CaFe_{0.2}Mg_{0.8}(CO_3)_2$.For siderite, which has an end member composition of $FeCO_3$, but significant amounts of Mg can substitute for Fe, no asymmetry was observed, which suggests only one siderite phase per sample. Green: clay-rich interval (Figure 4).

	WED 3.1	WED 3.2	WED 3.3 + 3.3.1	WED 3.4.1	WED 3.5.2	WED 3.6.1	WED 3.6.5	B1.1	B1.3	B1.10	B1.13
Quartz	67.90	35.45	68.66	67.13	54.65	44.42	60.81	59.83	54.73	65.29	67.88
Dolomite	**0.39**	**0**	**0**	**0**	**0**	**2.26**	**0.41**	**0.29**	**0**	**0**	**0**
Ankerite_Fe0.2	**2.55**	**0.28**	**1.10**	**1.17**	**2.54**	**8.62**	**3.10**	**7.43**	**0**	**2.18**	**0.15**
Ankerite_Fe0.54	**0.56**	**0.13**	**0.38**	**0.37**	**1.22**	**1.89**	**0.88**	**0.41**	**0**	**0.23**	**0.16**
Ankerite_Fe0.68	**0**	**0.18**	**0**	**0**	**0**	**0.71**	**0**	**0.00**	**0**	**0**	**0**
Siderite	**0.51**	**8.20**	**1.16**	**0.94**	**2.68**	**3.90**	**4.96**	**0.38**	**1.26**	**1.45**	**1.17**
Barite	1.77	0	0.52	0.79	0	0.71	0	0	0	0	0
Gypsum	0	0	0	0	1.99	1.22	0	0	1.13	0.56	0.74
Anatase	0	0	0.29	0.34	0.70	0	0	0	0	0	0
Plagioclase	5.01	7.61	7.05	7.04	7.11	4.80	7.08	2.20	1.71	1.41	1.66
K-feldspar	8.31	8.39	11.72	13.24	11.59	7.03	8.57	12.56	12.25	14.09	15.96
Pyrite	0	0.14	0	0	0.19	0	0.13	0.06	0	0.04	0
Marcasite	0	0	0	0	0	0	0	0	0	0	0
Sylvite	0	0.12	0	0	0	0	0	0	0	0	0
Halite	0.33	1.70	0.38	0.40	0.34	0.47	0.40	0.09	0	0.15	0.14
Anhydrite	0	0	0	0	8.73	7.28	0.92	5.96	22.42	3.99	3.48
Kaolinite	0	0	0	0	0	0	0	3.38	3.53	4.01	3.96
2:1 clay minerals	12.66	37.79	8.73	8.57	8.25	16.69	12.73	7.41	2.97	6.59	4.71
Average Fe-content Siderite	0.64	0.68	0.65	0.66	0.63	0.64	0.64	0.62	0.59	0.59	0.58

Table 12. Comparison of sample analysis by Qmineral with SGS Horizon and Panterra. The results from Qmineral are rewritten into the format for SGS Horizon: Dolomite includes the three ankerite variants and 2:1 clay minerals are assumed to be illite (Table 11). Note: Analysis by SGS results in higher amounts of quartz and lower amounts of the remaining minerals than Qmineral. Results from Panterra and Qmineral are similar, except for illite and occasionally siderite which are higher in the results from Qmineral. B1.10 and B1.11 give varying results, probably due to heterogeneity in the samples. Green: sheetflood lithofacies.

	Quartz	Plagioclase	K-feldspar	Total feldspar	Illite	Kaolinite	Dolomite	Siderite	Anhydrite	Halite
WED 3.1 – SGS	87.81	2.50	0.02	2.52	1.73	0	7.94	0	0	0
WED 3.1 - Qmin	67.90	5.01	8.31	13.32	12.66	0	3.50	0.51	0	0.33
WED 3.2 – SGS	57.21	8.98	3.69	12.68	27.02	0	0	3.09	0	0
WED 3.2 - Qmin	35.45	7.61	8.39	16.00	37.79	0	0.59	8.20	0	1.70
WED 3.3 – SGS	85.62	7.71	4.27	11.98	1.58	0	0.01	0.80	0	0.02
WED 3.3.1 – Panterra	80	2.00	10	12.00	3.00	0	4.00	1.00	0	-
WED 3.3 + 3.3.1 - Qmin	68.66	7.05	11.72	18.77	8.73	0	1.48	1.16	0	0.38
WED 3.4.1 – Panterra	80	2.00	13.00	15.00	3.00	0	1.00	1.00	0	-
WED 3.4.1 – Qmin	67.13	7.04	13.24	20.28	8.57	0	1.54	0.94	0	0.40
WED 3.5.2 – Panterra	74.00	2.00	9.00	11.00	5.00	0	7.00	1.00	2.00	-
WED 3.5.2 – Qmin	54.65	7.11	11.59	18.70	8.25	0	3.76	2.68	8.73	0.34
B1.1 – Panterra	66.00	1.00	14.00	15.00	3.00	5.00	10	0	1.00	-
B1.1 - Qmin	59.83	2.20	12.56	14.76	7.41	3.38	8.14	0.38	5.96	0.09
B1.3 – Panterra	56.00	1.00	10	11.00	1.00	4.00	0	0	28.00	-
B1.3 - Qmin	54.73	1.71	12.25	13.96	2.97	3.53	0	1.26	22.42	0
B1.10 – Panterra	60	1.00	12.00	13.00	1.00	4.00	2.00	tr	20	-
B1.10 - Qmin	65.29	1.41	14.09	15.50	6.59	4.01	2.41	1.45	3.99	0.15
B1.11 – Panterra	53.00	1.00	5.00	6.00	30	6.00	4.00	1.00	tr	-
B1.11 - Qmin	30.79	0.86	11.45	12.30	44.05	3.77	5.87	2.30	0	0.91
B1.13 – Panterra	74.00	tr	16.00	16.00	2.00	5.00	tr	tr	3.00	-
B1.13 - Qmin	67.88	1.66	15.96	17.62	4.71	3.96	0.31	1.17	3.48	0.14

*Table 13. Comparison of XRD by SGS and Panterra (upper) and QEMSCAN (lower) analyses for BRTZ. * XRD by Panterra. The illite content measured by QEMSCAN includes muscovite and illitised kaolinite, (Fe-)illite and (Fe-)illite/smectite. Note: QEMSCAN results in lower quartz and dolomite and in general higher feldspar (for Panterra analysis only plagioclase), illite and siderite (only for SGS analysis) content. Green: sheetflood lithofacies.*

	Quartz	Plagioclase	K-feldspar	Total feldspar	Illite	Kaolinite	Dolomite	Siderite	Anhydrite	Apatite	Halite
WED 3.1	87.81	2.50	0.02	2.52	1.73	0	7.94	0	0	0	0
	75.50	5.08	7.00	12.07	6.56	0.11	3.61	1.29	0	0.02	0.01
WED 3.2	57.21	8.98	3.69	12.68	27.02	0	0	3.09	0	0	0
	47.53	6.70	6.42	13.12	26.50	0.16	0.24	8.48	0	0.05	0
WED 3.3	85.62	7.71	4.27	11.98	1.58	0	0.01	0.80	0	0	0.02
	66.45	8.40	12.09	20.49	10.41	0.10	0.45	1.48	0.01	0.02	0.01
WED 3.3.1*	80	2.00	10	12.00	3.00	0	4.00	1.00	0	-	-
	70.51	5.72	8.40	14.13	5.59	0.04	1.60	0.88	0.03	-	5.82
WED 3.3.2*	83.00	2.00	7.00	9.00	4.00	0	4.00	tr	0	-	-
	62.88	7.66	14.04	21.69	8.72	0.07	3.05	0.72	0.02	-	2.11
WED 3.4	86.12	8.80	3.84	12.64	1.18	0	0.04	0	0	0	0.02
	69.15	6.39	11.58	17.97	6.95	0.08	1.11	2.84	0.01	0.02	0.02
WED 3.4.1*	80	2.00	13.00	15.00	3.00	0	1.00	1.00	0	-	-
	60.19	6.07	11.83	17.90	10.20	0.04	0.52	0.59	0.04	-	9.17
WED 3.4.2*	80	2.00	11.00	13.00	4.00	0	3.00	tr	0	-	-
	65.19	8.31	11.19	19.50	10.20	0.09	1.70	0.95	0.03	-	1.31
WED 3.5	81.43	6.50	1.63	8.12	0.61	0	1.00	0.70	**8.13**	0	0.01
	58.36	6.07	10.41	16.48	3.59	0.13	0.60	4.03	**15.94**	0.03	0
WED 3.5.2*	74.00	2.00	9.00	11.00	5.00	0	7.00	1.00	**2.00**	-	-
	56.60	7.29	10.58	17.87	9.77	0.14	5.27	4.25	**3.68**	-	0.90

*Table 14. Comparison of XRD by Panterra (upper) and QEMSCAN (lower) analyses for BRTZ. * only measured by XRD. The illite content measured by QEMSCAN includes muscovite and illitised kaolinite, (Fe-)illite and (Fe-)illite/smectite. Note: QEMSCAN and XRD by Panterra give very similar results except for illite and kaolinite which are respectively lower and higher in XRD.*

	Quartz	Plagioclase	K-feldspar	Total feldspar	Illite	Kaolinite	Dolomite	Siderite	Anhydrite	Halite
B1.1	66.00	1.00	14.00	15.00	3.00	5.00	10	0	1.00	-
	60.77	2.67	13.09	15.76	10.20	1.68	9.28	0.11	0.49	0.42
B1.3	56.00	1.00	10	11.00	1.00	4.00	0	0	28.00	-
	54.07	1.64	12.48	14.12	4.66	1.51	0.01	0.90	23.48	0.15
B1.4	69.00	tr	9.00	9.00	1.00	2.00	**17.00**	0	2.00	-
	54.47	1.02	14.29	15.31	5.23	0.98	**17.12**	0.15	3.93	1.89
B1.5	76.00	1.00	11.00	12.00	2.00	6.00	1.00	1.00	2.00	-
	62.87	1.92	16.47	18.39	8.08	2.03	1.38	1.37	4.84	0.03
B1.6	74.00	1.00	12.00	13.00	4.00	7.00	1.00	1.00	0	-
	59.95	1.90	16.16	18.06	12.46	1.92	0.33	3.48	0.13	1.40
B1.9*	68.00	tr	9.00	9.00	10	9.00	4.00	0	0	-
B1.10	60	1.00	12.00	13.00	1.00	4.00	2.00	tr	20	-
	54.94	1.29	12.39	13.68	5.02	1.55	7.66	1.31	13.78	0.84
B1.13	74.00	tr	16.00	16.00	2.00	5.00	tr	tr	3.00	-
	68.03	1.56	16.61	18.16	6.51	2.19	0.05	1.41	1.04	1.80

Table 15. Comparison of XRD by SGS (upper) and QEMSCAN (lower) analyses for WED2. The illite content measured by QEMSCAN includes muscovite and illitised kaolinite, (Fe-)illite and (Fe-)illite/smectite. Note: for the feldspars the quantification is similar for XRD and QEMSCAN. Quartz is much higher in XRD, illite, siderite and anhydrite in QEMSCAN.

	Quartz	Plagioclase	K-feldspar	Total feldspar	Illite	Kaolinite	Dolomite	Siderite	Anhydrite	Halite
WED 2.1	82.16	9.72	0	9.72	8.13	0	0	0	0	0
	65.67	9.09	0.23	9.32	20.35	0.17	0.61	2.80	0.19	0.01
WED 2.2	92.54	0	0	0	1.61	0.03	4.09	0	1.70	0.02
	71.18	0.05	0.18	0.23	14.09	0.28	9.74	0.10	3.72	0.11
WED 2.3	76.98	0	0	0	0.01	0	21.70	0	1.30	0.01
	66.10	0.06	0.17	0.23	10.37	0.23	18.59	0.22	3.59	0.06
WED 2.4	92.66	5.92	0	5.92	1.15	0	0	0	0.01	0.06
	78.35	6.44	0.14	6.57	12.41	0.11	0.07	1.06	0.27	0.02
WED 2.5	88.26	4.00	0	4.00	7.72	0.01	0	0	0	0.01
	64.20	4.59	0.37	4.96	28.53	0.89	0	0.07	0.11	0

*Table 16. XRD and QEMSCAN results from shale intervals within the sandstone reservoirs. * Detfurth Member. # B1.2 and B1.12 are mixed for an experimental study, see D12 from WP3.3 (Koenen et al., 2014).*

Sample	Analysis	Depth (m AH)	Quartz	Plagioclase	K-feldspar	Illite	Kaolinite	Dolomite	Siderite	Anhydrite	Apatite	Hematite	Muscovite	Biotite/chlorite
WED 3.6	XRD SGS	2838.3	48.09	7.78	2.99	38.44	0	0	2.69	0	0	0	-	-
	QEMSCAN		48.56	4.80	3.87	24.87	0.14	0.29	3.69	0	0.09	-	8.15	3.99
WED 3.8*	XRD SGS	2968.1	38.56	0	0	50.18	0	9.26	0	0	0	1.99	-	-
	QEMSCAN		55.55	0.12	1.83	31.12	0.07	6.61	0.21	0	0.04	-	3.31	0.86
WED 2.6	XRD SGS	2992.0	48.53	4.99	0	36.50	0	7.39	0	0	0.30	2.30	-	-
	QEMSCAN		47.18	3.49	0.63	27.16	0.28	6.06	1.11	0	0.16	-	10.08	2.87
B 1.11	XRD Panterra	2690.2	53.00	1.00	5.00	30	6.00	4.00	1.00	0	-	-	-	-
B 1.12	XRD Panterra	2690.5	53.00	1.00	5.00	29.00	6.00	5.00	1.00	0	-	-	-	-
B1.2 + B1.12#	XRD Qmineral	2678.8 / 2690.5	43.70	1.70	8.80	34.00	4.10	1.60	3.80	0	-	-	-	-

Table 17. XRD clay fraction analysis performed for an experimental study, see D12 from WP3.3 (Koenen et al., 2014). # B1.2 and B1.12 are mixed for this study.

	B1.10	B1.2 + B1.12#
Illiet	36	54
Illiet/Smectiet	25	37
'mixed layers' (83/17)*		
Kaoliniet	40	9

Appendix D

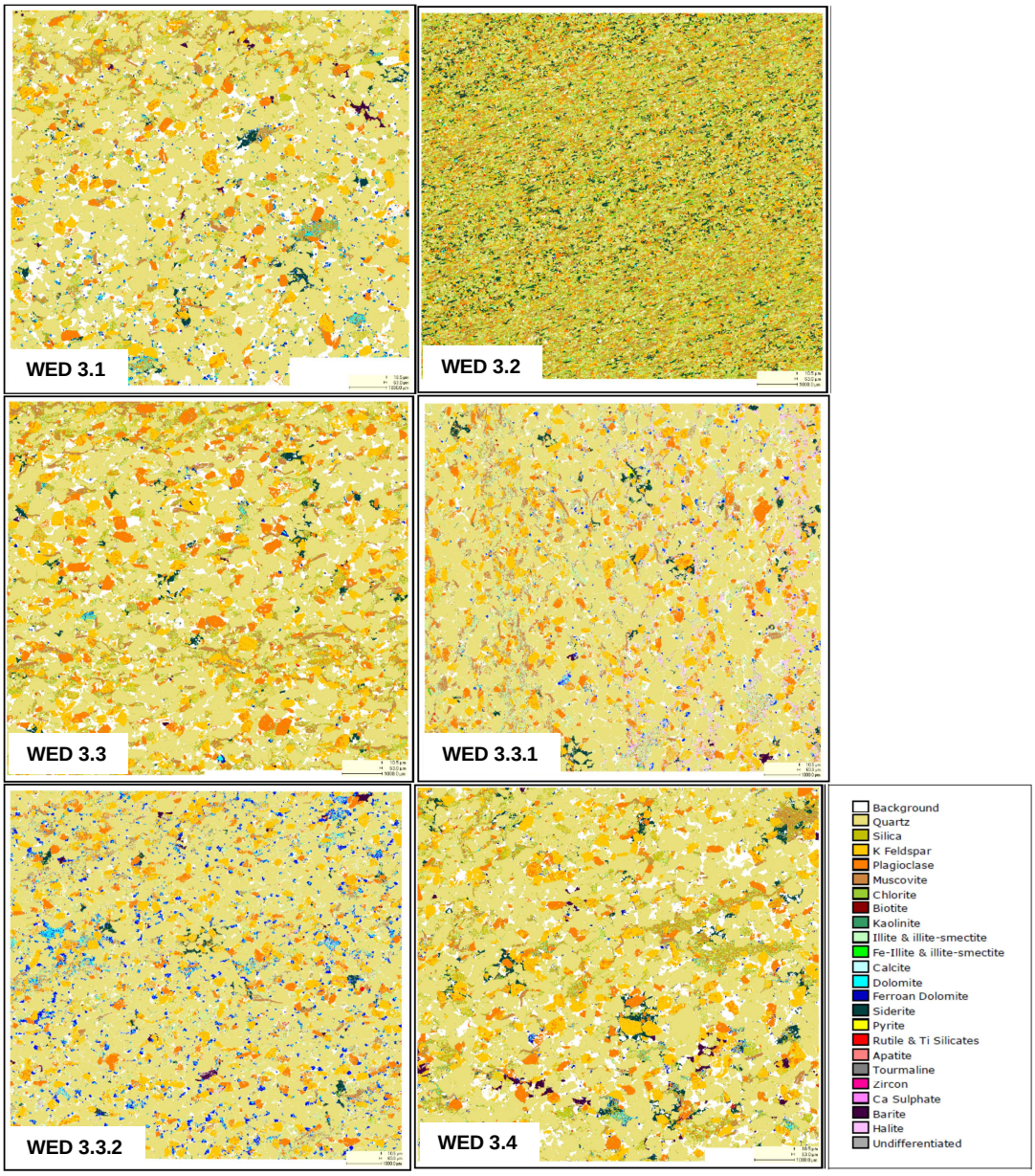

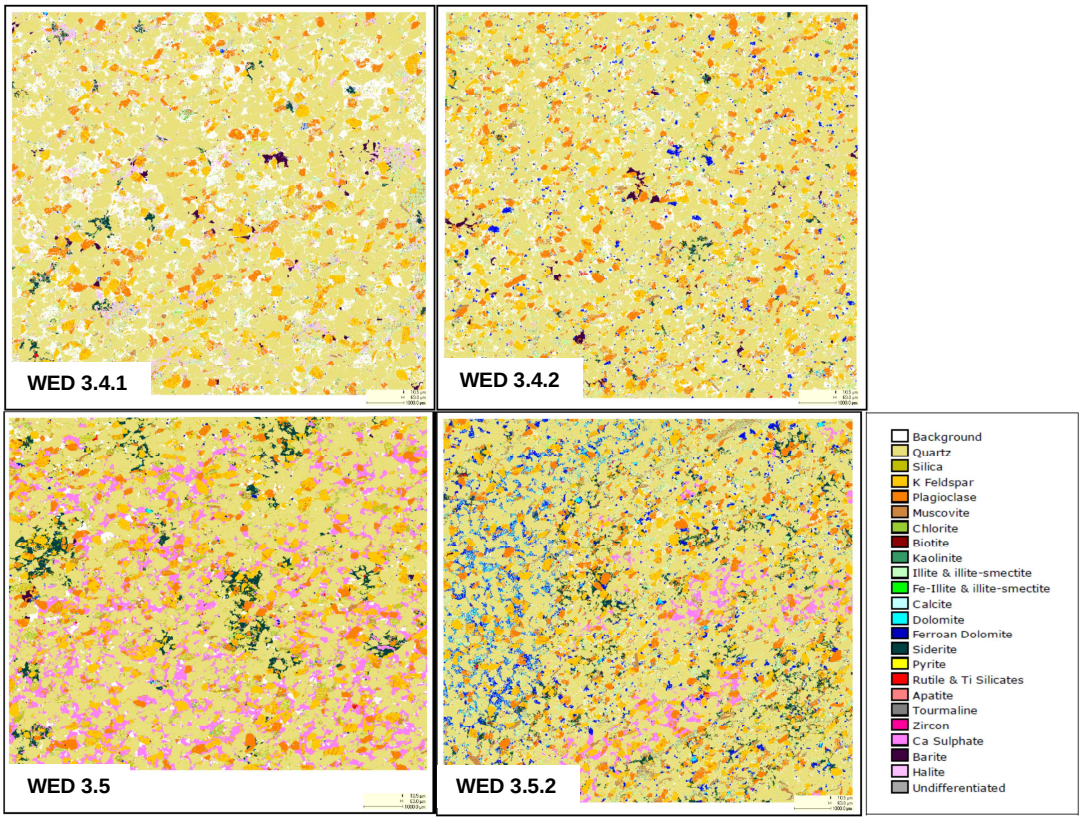

Figure 38. QEMSCAN images of WED3 samples.

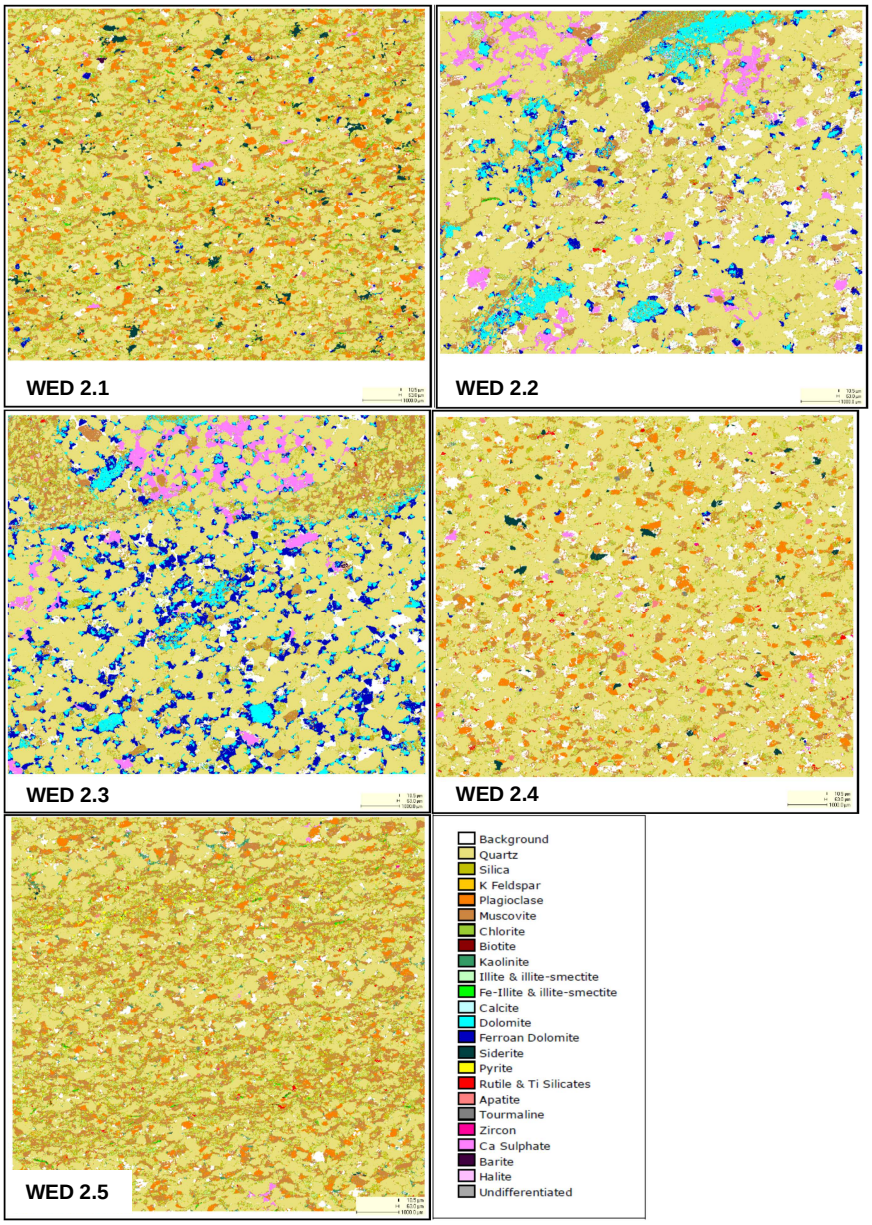

Figure 39. QEMSCAN images of WED2 samples.

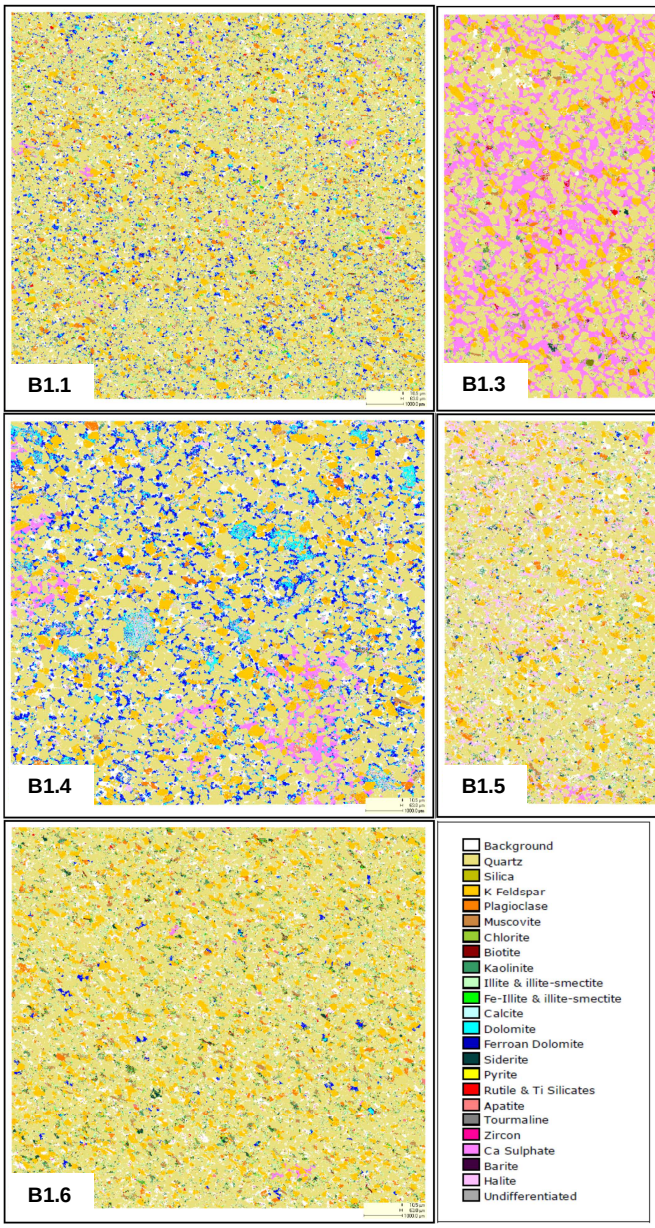

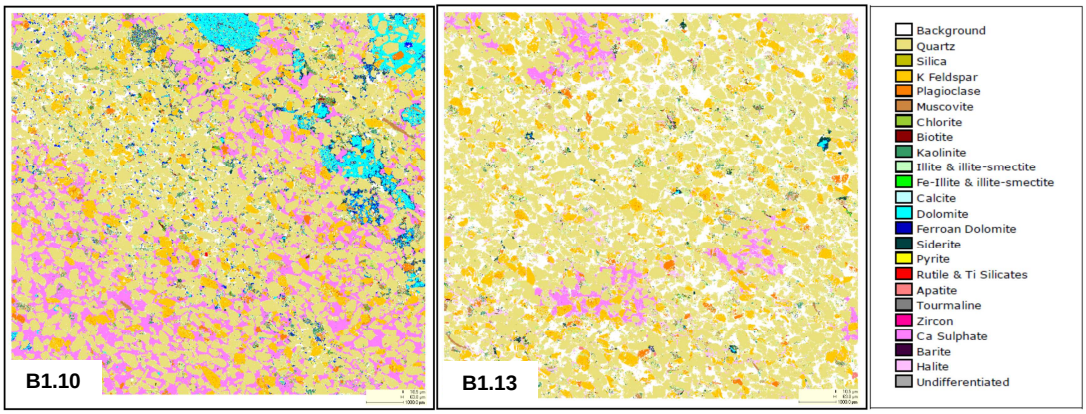

Figure 40. QEMSCAN images of BRTZ samples.

Appendix E

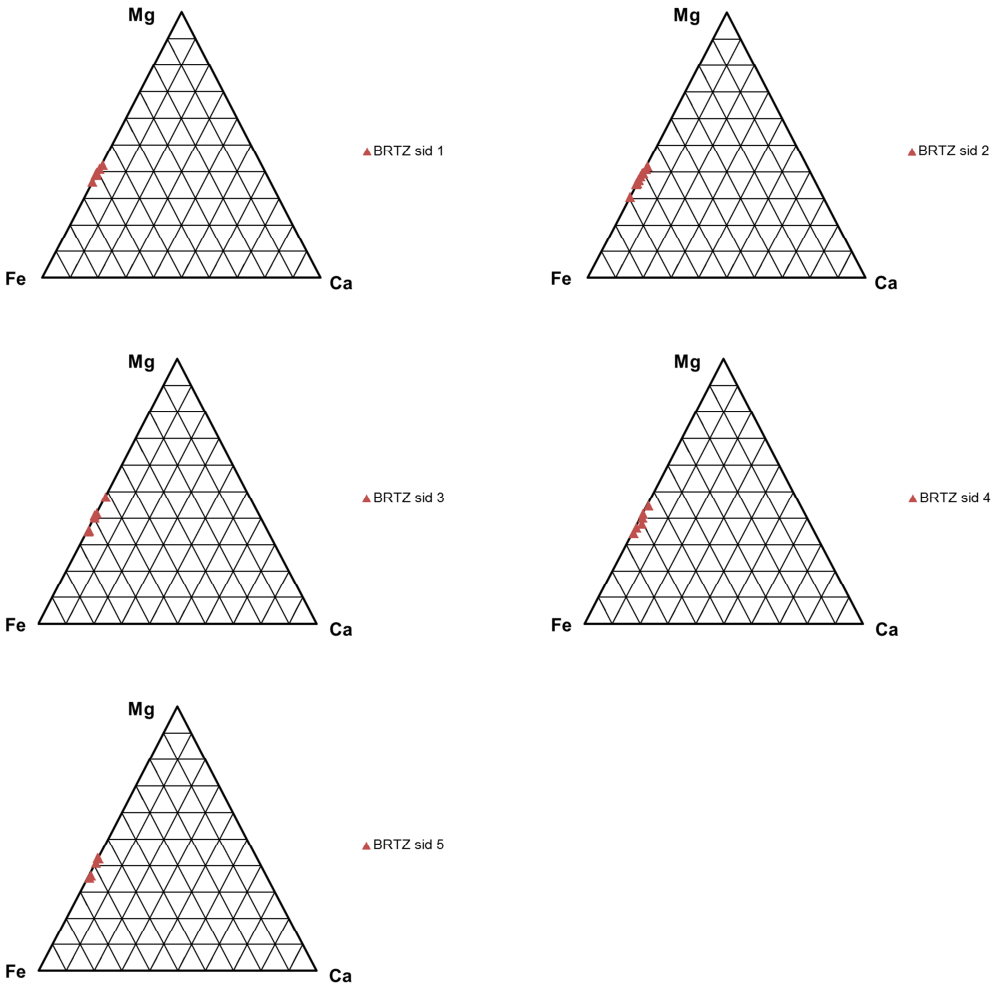

Figure 41. Ternary plots for the 5 types of siderite recognized in the BRTZ samples, based on EDX measurements.